



# Inclusive charm and bottom quark pair production cross sections at hadron colliders at next-to-next-to-leading-order accuracy

David d'Enterria <sup>1,\*</sup> Felix Hekhorn <sup>2,3,†</sup> Ilkka Helenius <sup>2,3,‡</sup>  
Văn Dũng Lê <sup>3,§</sup> and Hannu Paukkunen <sup>2,3,¶</sup>

<sup>1</sup>*CERN, EP Department, CH-1211 Geneva, Switzerland*

<sup>2</sup>*University of Jyväskylä, Department of Physics, P.O. Box 35, FI-40014 University of Jyväskylä, Finland*

<sup>3</sup>*Helsinki Institute of Physics, P.O. Box 64, FI-00014 University of Helsinki, Finland*

The inclusive cross sections for charm ( $c\bar{c}$ ) and bottom ( $b\bar{b}$ ) quark-antiquark pair production in proton-proton, proton-antiproton, and proton-nucleus collisions are studied over a wide range of center-of-mass energies,  $\sqrt{s} \approx 10 \text{ GeV} - 400 \text{ TeV}$ . All existing data over  $\sqrt{s} \approx 10 \text{ GeV} - 14 \text{ TeV}$  are collected and compared to calculations at next-to-next-to-leading-order (NNLO) accuracy using the new fixed-order MaunaKea open-source code for varying sets of parton distribution functions (PDFs). Relative to next-to-leading-order (NLO) predictions, the NNLO cross sections are enhanced by up to a factor of two, with the associated theoretical scale uncertainties reduced by the same amount, leading to agreement with experimental data over the full range of collision energies. The NNLO results are also compared with NLO predictions obtained within the SACOT- $m_T$  general-mass variable-flavour-number scheme. Despite still sizable theoretical and experimental uncertainties,  $c\bar{c}$  cross section at multi-TeV energies can provide extra constraints on the gluon density at very small- $x$  in global PDF analyses. In the bottom sector, more precise cross section measurements at low energies,  $\sqrt{s} \approx 10 - 100 \text{ GeV}$ , can help constraint the bottom-quark pole mass.

## CONTENTS

I. Introduction	2
II. Experimental data	3
A. Heavy-quark fragmentation fractions	3
B. Measurements of $c\bar{c}$ cross sections	7
C. Measurements of $b\bar{b}$ cross sections	9
III. Theoretical predictions	11
A. FFN scheme: NNLO calculations	11
Missing higher-order uncertainties	12
Breakdown of partonic channels	13
Heavy-quark mass dependence and uncertainties	14
PDF dependence and uncertainties	15
QCD coupling uncertainties	18
B. VFN scheme: NLO calculations	19
C. Corrections for p-p-equivalent cross sections	20
IV. Data versus pQCD	21
A. $c\bar{c}$ cross sections	22
B. $b\bar{b}$ cross sections	26
V. Summary	26
A. NNLO charm p-p cross section tables	30
B. NNLO bottom p-p cross section tables	36
References	40

\* david.d'enterria@cern.ch

† felix.a.hekhorn@jyu.fi

‡ ilkka.m.helenius@jyu.fi

§ dunglvht@gmail.com

¶ hannu.paukkunen@jyu.fi

## I. INTRODUCTION

Substantial theoretical progress has been achieved over the past decade in the computation of higher-order corrections for hard-scattering cross sections in hadronic collisions within perturbative quantum chromodynamics (pQCD), in parallel with the steadily improved experimental precision achieved in proton-proton (p-p) measurements at the CERN Large Hadron Collider (LHC). Advances in analytical techniques, numerical methods, and automation have enabled increasingly precise predictions for a wide range of observables [1]. At present, state-of-the-art fixed-order calculations for the cross sections of hard processes in p-p collisions are available at next-to-next-to-leading-order (NNLO) accuracy in the expansion of the strong coupling constant,  $\alpha_s$ , often supplemented by resummation of logarithmically enhanced contributions up to next-to-next-to-leading-log (NNLL) accuracy [2, 3], with an increasing number of processes being computed at next-to-NNLO ( $N^3$ LO) [2–4].

Among the pQCD processes in hadronic collisions, the production of heavy quarks –top, bottom, and charm quarks– predominantly proceeds through gluon-gluon fusion processes,  $gg \rightarrow Q\bar{Q}$  (with heavy  $Q = c, b, t$  quarks), and thereby constitute a particularly sensitive probe of the gluon density in the hadrons. The production of pairs of top ( $t\bar{t}$ ), bottom ( $b\bar{b}$ ), and charm ( $c\bar{c}$ ) quarks is characterized by intrinsically hard scales, corresponding to at least twice their (pole) quark masses,  $m_Q \approx 172.5, 4.8, 1.67$  GeV [5] respectively, which are much larger than the nonperturbative QCD scale  $\Lambda_{\text{QCD}} \approx 0.2$  GeV, thereby enabling the use of the pQCD framework to compute their cross sections. Within the factorization theorem framework [6], these cross sections are obtained from convolutions of partonic subprocess cross sections (“matrix elements”), computed perturbatively as expansions in powers of  $\alpha_s$ , with parton distribution functions (PDFs), evolving according to the DGLAP equations [7–9], that encode the longitudinal momentum fraction ( $x$ ) and virtuality ( $Q^2$ ) carried by the constituent partons of the colliding hadrons. Given the phenomenological significance of the top quark at the LHC, NNLO calculations were first performed for  $t\bar{t}$  production with the `HATHOR` [10] and `TOP++` [11–14] codes, achieving very good agreement with experimental data [15, 16]. The high precision of both  $t\bar{t}$  data and theory has enabled not only to constrain the high- $x$  region of the gluon PDF [17–20], but also accurately measure  $m_{\text{top}}$  [15, 21], as well as precisely extract  $\alpha_s$  [22–24].

For the production of the lighter charm and bottom quarks, the theoretical state-of-the-art has been for many years the next-to-leading order (NLO) accuracy for their differential cross sections (calculated e.g. with the `MNR` code [25]), complemented with next-to-leading-log (NLL) transverse momentum resummation often obtained in a general-mass variable-flavour-number scheme (GM-VFNS) [26–33] (such as in the `FONLL` code [34, 35]). Matching fixed-order calculations, e.g. from `POWHEG` [36, 37] or `MC@NLO` [36], with a parton-shower (PS) algorithm from general-purpose event generators such as `PYTHIA` [38, 39], provides an NLO-accurate description of the complete collision event that can be used to compare with experimental measurements applying arbitrary kinematical cuts. More recent developments include differential NNLO predictions [40–43] for  $b\bar{b}$  production (such as in the `MATRIX` framework [44]), or transverse-momentum-dependent approaches [45]. Whereas inclusive charm-anticharm and bottom-antibottom production cross sections can in principle be computed at NNLO accuracy using the same computational frameworks employed for  $t\bar{t}$  production, as done in [46–48], no systematic study has to date compared the full set of available inclusive  $c\bar{c}$  and  $b\bar{b}$  measurements with NNLO predictions including a comprehensive assessment of the associated theoretical uncertainties. Several factors explain this situation. First, the relatively low energy scales involved in inclusive charm production lead to sizable theoretical uncertainties –particularly from missing higher-order pQCD corrections, PDFs, and charm quark mass– thereby reducing the predictive power of the calculations. Second, LHC measurements have indicated [49–52] that charmed hadrons are produced at the LHC in different mutual proportions than observed at  $e^+e^-$  collisions or in deep-inelastic scattering (DIS) at HERA. The observed relative reduction (increase) of charmed meson (baryon) yields in p-p compared with  $e^+e^-$  collisions has complicated the proper extraction of inclusive charm production cross sections from the experimentally measured hadronic final states. Similar observations have been made also in the case of bottom quarks [53], though the available data are currently more limited.

The enhanced heavy-quark baryon-to-meson production ratio observed in p-p collisions at the LHC has been interpreted as evidence for environment-dependent heavy-quark hadronization, driven by the high density of colour charges produced at TeV energies, in a situation conceptually similar to that first proposed to account for analogous effects originally seen at heavy-ion colliders [54–57]. In p-p events at the LHC, the presence of large number of semihard multiparton interactions leads to heavy quarks hadronizing within a dense system of surrounding partons and beam remnants, where effects such as colour reconnection [58], coalescence (recombination) with nearby light quarks [59–61], and large diquark formation may enhance the probability to form baryons at the expense of mesons compared with the “vacuum” fragmentation measured in  $e^+e^-$  collisions. Interestingly, the observed baryon-to-meson enhancement has been found to be nearly equal in p-p and p-Pb collisions at the LHC [53, 62], whereas the surrounding hadronic activity is twice larger in the latter than in the former system [63], indicating that the system-size dependence of the baryon-enhancement appears to be relatively weak. The LHC data indicate that the enhanced baryon-to-meson pro-

duction fractions appear at low transverse momentum  $p_T$ , whereas for increasing  $p_T$  values the production fractions become roughly consistent with those from  $e^+e^-$  collisions and DIS. From the point of view of collinear factorization, this suggests the presence of significant higher-twist (HT) contributions not describable with universal parton-to-hadron fragmentation functions (FFs) and/or PDFs without some extra modeling. Evidence for the presence of such effects in p-p collisions at the LHC has been also suggested even in high- $p_T$  light-hadron production [64]. Whether the enhanced baryon-to-meson production ratio can be uniquely classified as a final-state effect, and/or as some other HT dynamics, remains an open question under study.

The main goal of this work is to confront fixed-order NNLO predictions for inclusive charm- and bottom-quark production cross sections, including a systematic assessment of all sources of theoretical uncertainties, with the available experimental data from hadronic collisions over a broad range of center-of-mass (c.m.) energies, spanning  $\sqrt{s} \approx 10$  GeV–13 TeV, and extending up to the  $\sqrt{s} \approx 100$  TeV regime foreseen at the CERN Future Circular Collider (FCC) [65, 66], and even  $\sqrt{s} \approx 400$  TeV reached in ultrahigh-energy collisions of cosmic protons with the upper atmosphere [67]. To this end, we first discuss the measurements of the charm- and bottom-quark fragmentation fractions used to derive the  $\sigma(Q\bar{Q})$  cross sections from hadronic final states, and compile all existing measurements of inclusive  $c\bar{c}$  and  $b\bar{b}$  production cross sections in p-p, proton-antiproton (p- $\bar{p}$ ), and proton-nucleus (p-A) collisions (Section II). We then introduce a new numerical NNLO implementation code, called MaunaKea [68], based on the `TOP++` matrix elements interfaced with the `PineAPPL` fast interpolation grids [69, 70] (Section III A). All sources of theoretical uncertainties, including missing higher-order corrections, PDFs, heavy-quark masses, and  $\alpha_s$  are examined. The MaunaKea predictions are subsequently compared with those obtained from resummed NLO calculations using the SACOT- $m_T$  GM-VFNS framework (Section III B). A detailed assessment of the level of theory and data agreement is presented in Section IV. Finally, the main results are summarized in Section V. The appendices A and B provide the charm and bottom NNLO cross sections computed in this work in a tabulated form.

## II. EXPERIMENTAL DATA

The production yields of charm and bottom quarks in hadronic collisions increase significantly with c.m. energy. At the top LHC energies, they represent about 20% (charm) and 1% (bottom) of the total inelastic p-p cross section of  $\sigma(p\text{-}p \rightarrow X) \approx 75$  mb [46]. Virtually all heavy quarks are produced in pairs via QCD processes because single heavy-quark production is possible only through quark-flavour-violating weak interactions that are relatively suppressed by many orders-of-magnitude. Experimentally, one measures the fragmentation products of c- and b-quarks in the form of D, B mesons (including their excited  $D^*, B^*$  states),  $\Lambda_{c,b}$ ,  $\Sigma_{c,b}$ ,  $\Omega_{c,b}$  baryons, plus quarkonia bound states [71–73] of the charmonium ( $J/\psi$ ) and bottomonium ( $\Upsilon$ ) families. Both charm and bottom hadrons decay via the weak interaction and therefore have relatively long lifetimes, leading to typical average decay lengths of  $c\tau \approx 150 \mu\text{m}$  for charm and  $c\tau \approx 470 \mu\text{m}$  for bottom hadrons [5]. Since bottom hadrons also decay into charm hadrons, their successive decay chain results in final states with significantly displaced vertices. Collider experiments heavily exploit this property to measure heavy-quark production by identifying the displaced secondary and tertiary vertices of their fragmentation hadron decays with high-resolution silicon vertex detectors. We discuss first the experimental charm- and bottom-quark fragmentation fractions, and then provide a systematic compilation of all charm-anticharm and bottom-antibottom measurements performed to date at hadronic colliders.

### A. Heavy-quark fragmentation fractions

Most of the inclusive  $c\bar{c}$  and  $b\bar{b}$  cross sections experimentally determined so far are based on measurements of a fraction of the decay channels into heavy-quark hadrons plus, where needed, model-dependent extrapolations from the visible transverse-momentum and rapidity ( $p_T, y$ ) range to the full phase space. The final extraction of the inclusive  $\sigma(c\bar{c})$  and  $\sigma(b\bar{b})$  cross sections is performed by dividing the measured inclusive heavy-quark hadron cross section,  $\sigma(h_Q)$ , by the corresponding total charm or bottom decay fragmentation fractions<sup>1</sup>,  $f(Q \rightarrow h_Q)$ :

$$\sigma(Q\bar{Q}) = \sigma(\sum h_Q) = \frac{\sigma(h_Q)}{f(Q \rightarrow h_Q)}, \text{ for } Q = c, b. \quad (1)$$

---

<sup>1</sup> Hereafter, expressions such as  $f(Q \rightarrow h_Q)$  refer to heavy-quark or antiquark hadron production that, by charge conjugation, satisfy  $f(Q \rightarrow h_Q) \equiv f(\bar{Q} \rightarrow \bar{h}_Q)$ .

Whenever different heavy-quark hadron species  $h_Q$  are measured simultaneously in the same colliding system, their cross sections and fragmentation fractions are conveniently added up or combined (e.g. in the case of measurements of ground and excited hadronic states, where the latter feed the yields of the former) to obtain the corresponding  $\sigma(Q\bar{Q})$  value. In addition, several  $\sigma(c\bar{c})$  extractions exist also based on measurements of high- $p_T$  displaced single leptons ( $\ell^\pm = e^\pm, \mu^\pm$ ) produced in the charmed hadron decays, which use instead the inclusive fragmentation fraction  $f(c \rightarrow \ell^+) = (9.71 \pm 0.32)\%$  [74] to extrapolate to a total heavy-Q cross section.

The heavy-quark fragmentation fraction into a specific hadron  $f(Q \rightarrow h_Q)$  is a soft nonperturbative process, which cannot be calculated with pQCD techniques, and instead one uses experimental data for their determination. The charm-quark fragmentation fractions are shown in Fig. 1 as measured in  $e^+e^-$  collisions at LEP [75] (upper left), derived from a combination of selected  $e^+e^-$ , DIS, and p-p collisions [76] (upper right), and determined by ALICE in p-p collisions at 5 TeV [51] (lower left) and 13 TeV [77] (lower right).

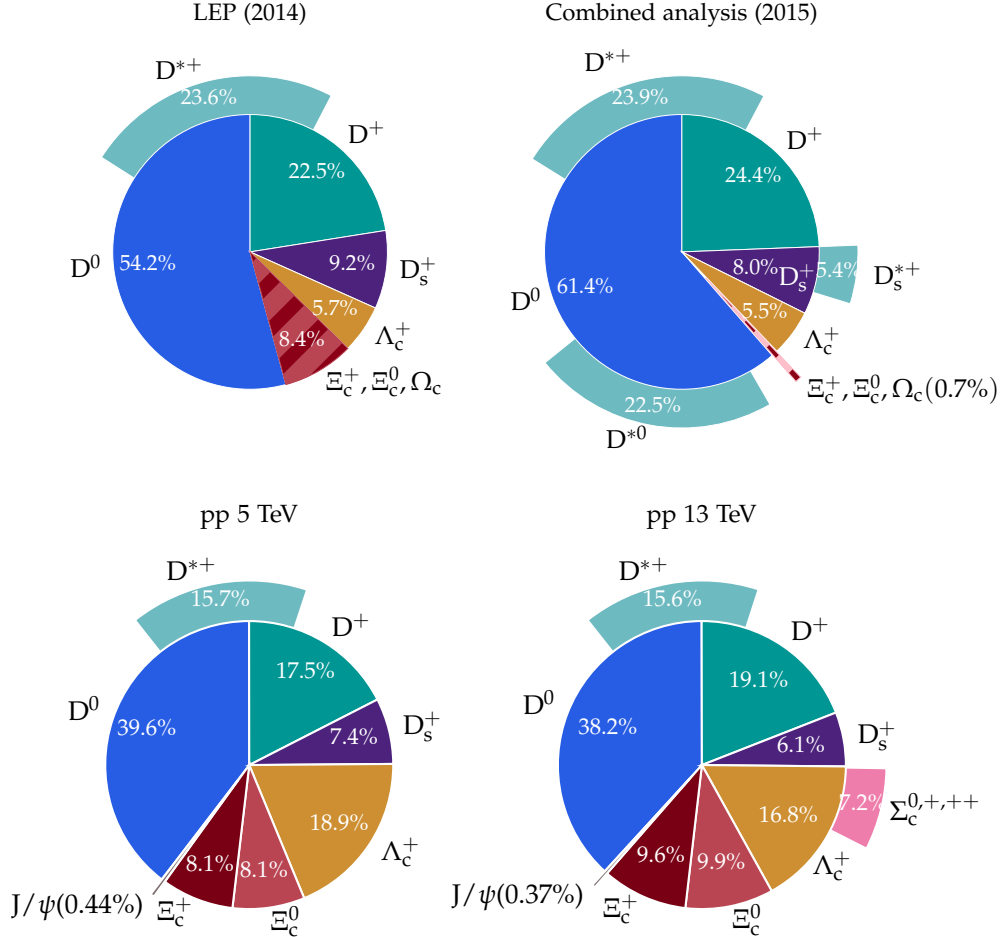


FIG. 1. Charm-quark fragmentation fractions  $f(c \rightarrow h_c)$  into specific charmed hadrons as obtained from different analyses using data from  $e^+e^-$  at LEP (upper left) [75], a combination of  $e^+e^-$ , DIS and p-p collisions (upper right) [76], and ALICE in p-p at 5 TeV (lower left) [51] and 13 TeV (lower right) [77].

Up until about 2015, the data indicated that charm meson and baryon production represented about 85–90% and 15–10%, respectively, of the total charm-quark fragmentation products. However, recent p-p measurements at the LHC [49–52, 62, 77] show an increased proportion of baryons at the expense of mesons, with the mesons (baryons) contributing about 65% (35%) of the total charm production yields. This enhanced charm baryon over meson production observed at the LHC, compared with that measured in  $e^+e^-$  collisions, is indicative of a violation of charm-quark fragmentation universality. Whether this is due to final-state hadronization effects, as aforementioned, or indicative

of other HT phenomena (e.g. enhanced heavy-quark production among the beam remnants outside of the experiment acceptances, or other possibilities) remains an open question. In any case, extrapolations from charm meson to total  $c\bar{c}$  cross sections using Eq. (1) at the LHC have to take into account such a non-universality or, otherwise, by using the “vacuum”  $e^+e^-$  fragmentation fractions, one would extract lower  $\sigma(c\bar{c})$  values. The evolution over time of the values of the charm hadron-to-quark fragmentation fractions measured across various collision systems is shown in Fig. 2. This compilation plot helps clarify some of the differences in charm cross section values inferred from measurements of specific charmed hadrons at different periods, as discussed below.

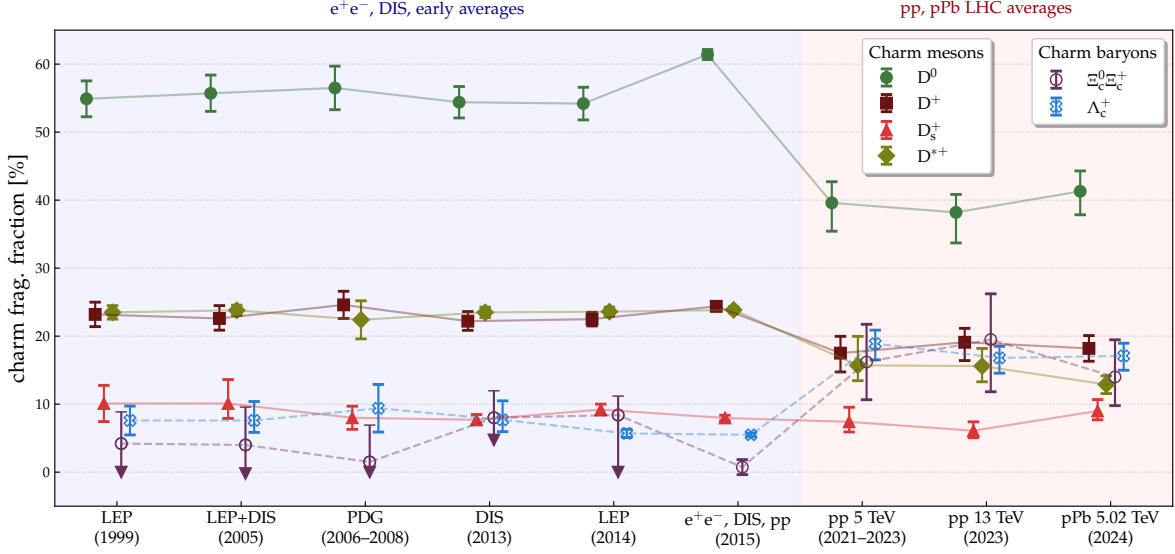


FIG. 2. Time evolution of charm-quark fragmentation fractions into charm mesons and baryons for different colliding systems as determined from LEP data (1999) [78], combined LEP and DIS analysis (2005) [79], reported in the PDG over 2006–2008 [80], DIS data update (2013) [81], LEP data update (2014) [75], combined  $e^+e^-$ , DIS, and p-p analysis (2015) [76], ALICE p-p 5 TeV (2021–23) [51, 77], ALICE p-p 13 TeV (2023) [77], and ALICE p-Pb 5.02 TeV (2024) [62]. These different fragmentation fractions have been used throughout different time periods to extract  $\sigma(c\bar{c})$  in hadronic collisions via Eq. (1) as discussed in the text.

The measurement of  $b\bar{b}$  cross sections relies on the direct reconstruction of B mesons or on the measurement of “nonprompt” (n.p.) charmed hadrons or leptons, which themselves originate from the weak decays of bottom-quark hadrons through the decay chain  $b \rightarrow h_b \rightarrow h_c (\rightarrow \ell^+)$ . Such n.p. particles are reconstructed farther away from the interaction point, in tertiary charm-hadron decay vertices (where the primary and secondary vertices correspond to the p-p collision point, and the B-hadron decay point, respectively). The fragmentation fractions of bottom quarks into different bottom hadrons are shown in Fig. 3 as extracted from  $e^+e^-$  collisions at LEP [74] (upper left) and from p- $\bar{p}$  collisions at Tevatron (upper right). The lower histogram shows the b-quark fragmentation fractions into c-hadrons and displaced electrons measured at LEP [75]. Some evidence of increased bottom baryon-to-meson ratios in hadron-hadron compared with  $e^+e^-$  collisions has been observed at Tevatron [82] (Fig. 3, upper right chart) and at the LHC at forward rapidities [53].

About a half of the experimental  $\sigma(b\bar{b})$  cross sections are derived based on the measurement of very displaced n.p.  $J/\psi$  mesons and/or charged leptons  $\ell^\pm$  from intermediate charmed-hadron decays. The general method to obtain the total bottom cross sections from such n.p. decay products is through the expression,

$$\sigma(b\bar{b}) = \frac{\sigma(\text{n.p. } J/\psi \text{ or } \ell^\pm)}{2 \mathcal{B}(b \rightarrow J/\psi \text{ or } \ell^+)}, \quad (2)$$

which relies on the well-measured inclusive decay branching fractions  $\mathcal{B}(b \rightarrow J/\psi X) = (1.16 \pm 0.10)\%$  and  $\mathcal{B}(b \rightarrow e^\pm X) = (20.5 \pm 0.7)\%$  [5], and the factor of two in the denominator accounts for the contributions from both b and  $\bar{b}$  hadron decays. The  $\mathcal{B}(b \rightarrow J/\psi X)$  value is an average from LEP measurements around the Z peak [83–85]. These experiments first measure the inclusive branching fraction  $\mathcal{B}(Z \rightarrow J/\psi X) = (0.351 \pm 0.024)\%$ , from which a small fraction of prompt- $J/\psi$  events,  $f_{J/\psi}^{\text{prompt}} \approx 2\text{--}8\%$  is subtracted, to isolate the inclusive  $\mathcal{B}(Z \rightarrow b \rightarrow J/\psi X)$  component. Finally, this value is divided by  $\mathcal{B}(Z \rightarrow b\bar{b}) = 15.12\%$  to obtain the branching fraction:  $\mathcal{B}(h_b \rightarrow J/\psi X) =$

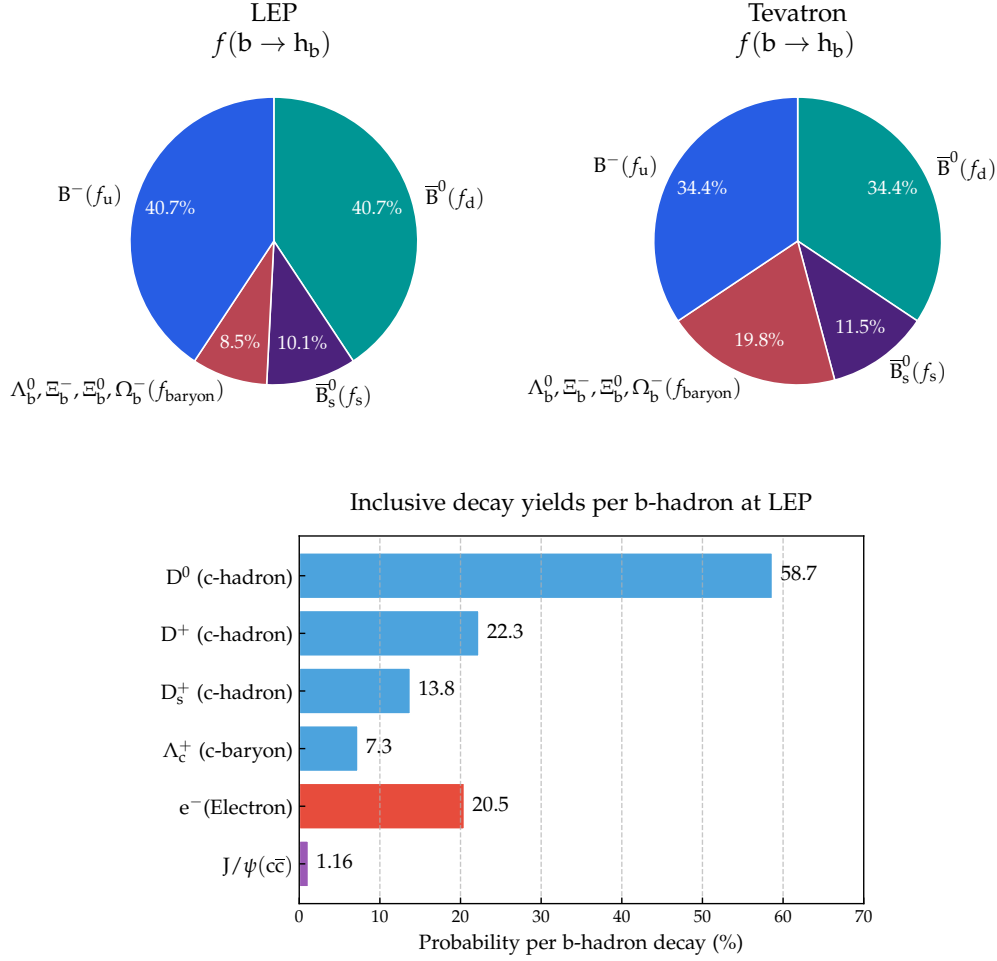


FIG. 3. Bottom-quark fragmentation fractions into different b-hadrons measured at LEP [74] (upper left) and Tevatron [82] (upper right), and inclusive yields to c-hadrons and electrons measured at LEP [75] (lower panel). The symbols  $f_u$ ,  $f_d$ ,  $f_s$ , and  $f_{\text{baryon}}$  are typically used to indicate, respectively, the fractions of  $B^+$ ,  $B^0$ ,  $B_s^0$ , and weakly-decaying bottom baryons in b-quark fragmentation.

$\mathcal{B}(Z \rightarrow b \rightarrow J/\psi X)/(2 \mathcal{B}(Z \rightarrow b\bar{b}))$ . The factor of two in the denominator accounts for the fact that each  $Z \rightarrow b\bar{b}$  event provides two independent opportunities to produce a  $J/\psi$  meson, one from the  $b$  quark and one from the  $\bar{b}$  antiquark. The total inclusive electron/positron yield from b-hadrons,  $\mathcal{B}(b(\rightarrow \bar{c}) \rightarrow e^\pm X) = (20.5 \pm 0.7)\%$ , is the sum of three distinct decay components [86–89]: the primary semileptonic decay  $\mathcal{B}(b \rightarrow e^\pm \bar{\nu} X) = (10.86 \pm 0.35)\%$ , the dominant cascade decay  $\mathcal{B}(b(\rightarrow e^\pm \bar{\nu}) \rightarrow c \rightarrow e^\pm \nu X) = (8.02 \pm 0.19)\%$ , and the secondary cascade decay  $\mathcal{B}(b \rightarrow \bar{c} \rightarrow e^\pm \bar{\nu} X) = (1.6_{-0.4}^{+0.5})\%$  through the charm quark pair production channel ( $b \rightarrow c\bar{c}$ ). Because other hadronic  $Z$  decays are a copious source of non-bottom leptonic backgrounds, these measurements do not rely on an intermediate inclusive  $Z$  branching fraction. Instead, events containing b-hadrons are selected using lifetime tagging. The analysis then exploits the fact that electrons from primary b-hadron decays ( $b \rightarrow e$ ) exhibit characteristically large momentum and transverse momentum relative to the jet axis. This allows the extraction of  $\mathcal{B}(b \rightarrow e^\pm \bar{\nu} X)$  and the cascade fractions directly by performing multi-parameter fits to various distributions, such as electron momentum, transverse momentum, and dilepton correlations. This fitting procedure statistically separates the primary signal from the cascade decays ( $b \rightarrow c \rightarrow e^\pm$ , and  $b \rightarrow \bar{c} \rightarrow e^\pm$ ), primary charm decays ( $Z \rightarrow c\bar{c} \rightarrow e^\pm X$ ), and non-prompt sources such as photon conversions and misidentified hadrons. Ultimately, these individual experimental measurements were combined by the LEP Electroweak Heavy Flavour Working Group to perform a global fit of multiple electroweak parameters [74, 90].

As a last comment regarding the different heavy-quark fragmentation fractions observed at LEP and the LHC, it is important to keep in mind that the experimental geometric acceptances and kinematic selections for final states

in  $e^+e^-$  and hadron-hadron collisions differ significantly (and, to some extent, also between the Tevatron and the LHC). Whereas LEP experiments detect almost the full phase space for hadron production, this is not true for hadron-collider experiments where a fraction of the particle activity goes undetected below  $p_T$  thresholds and/or beyond the detector rapidity coverage (e.g. along the beam direction). Consequently, simple combinations of the LEP and LHC fragmentation fractions into a global average are unsuitable. In this context, LHC heavy-quark hadron measurements can be more consistently extrapolated by either using the fragmentation fractions measured in situ, or alternatively by employing the LEP fractions as a vacuum fragmentation baseline, but stating clearly the underlying assumptions of either choice.

## B. Measurements of $c\bar{c}$ cross sections

Table I collects more than 50 measurements of charm cross sections in hadronic collisions from  $\sqrt{s_{NN}} \approx 11$  GeV (fixed target) up to 13 TeV (LHC). For each result, the first three columns list, respectively, the experiment and colliding system<sup>2</sup>, the detected charm-hadron species (or their decay particles), and their fiducial kinematic range. The latter include the  $p_T$  and  $y$  (or pseudorapidity  $\eta$ ), and/or invariant mass ( $m_{ee}$ ), and/or longitudinal momentum fraction ( $x_F$ ) selection criteria applied by each experimental analysis. The three next columns list, respectively, the fragmentation fraction  $f(c \rightarrow h_c)$  used to extrapolate the hadron cross section  $\sigma(h_Q)$  to a  $\sigma(c\bar{c})$  value via Eq. (1), the measured fiducial cross section, and the typical extrapolation factor used to convert the fiducial into a total cross section, usually obtained with MC simulations via

$$\sigma_{\text{tot}}(\sum h_Q) = \left( \frac{\sigma_{\text{tot}}^{\text{MC}}(\sum h_Q)}{\sigma_{\text{fid}}^{\text{MC}}(\sum h_Q)} \right) \cdot \sigma_{\text{fid}}(\sum h_Q) \quad \text{with MC} = \text{FONLL, POWHEG, PYTHIA 6, PYTHIA 8, \dots} \quad (3)$$

Typical fiducial extrapolation factors amount to 5–10, with relatively large uncertainties due to the lack of experimental data in the detector “blind spots”, at low  $p_T$  and/or at very forward-backward rapidities, which limit the validation of MC model predictions. The last column lists the final derived charm-anticharm production cross section. Whenever two (three) uncertainties are quoted, the first one corresponds to the statistical uncertainty, and the second to the combined systematic and extrapolation uncertainty (or the third to the extrapolation uncertainty alone). In case a given publication gives several  $c\bar{c}$  cross sections obtained from different MC generator extrapolations via Eq. (3), we quote their average and add in quadrature the standard deviation of the different MC central values as an additional uncertainty. All p-A (and the few d-A) cross sections are quoted normalized per nucleon-nucleon collision, i.e. divided by nuclear mass number  $A$  (or by  $2A$  for the deuteron-nucleus collisions).

Most listed values in Table I are taken directly from the bibliographical references indicated in the first column, unless marked as ‘(t.w.)’ (standing for ‘this work’) in which case they have been obtained from our studies here by adding up the measured hadronic fiducial cross sections, applying the quoted fragmentation fractions to obtain fiducial charm-level cross section, and extrapolating them to the full phase space with the listed factors to obtain the final  $\sigma(c\bar{c})$  values. All results estimated here this way have a single uncertainty obtained by adding all sources in quadrature and rounding it up conservatively. In the before-last column, the phase-space extrapolation factors are either taken directly from the original papers, or estimated here from FONLL predictions for each colliding system, using the central CTEQ6.6 PDFs [137] (except for 8.16 TeV where we used NNPDF30\_nlo\_as\_0118 [138]) and conservatively assigning +50% and –10% uncertainties based on the maximum envelope of differences found between our estimate and other factors used in the literature.

Most final cross sections obtained in this way, for a given colliding system and c.m. energy, are mutually consistent within their (often large) uncertainties. A few exceptions to this rule are results obtained from measurements of rare hadronic final states (e.g.  $\Lambda_c$  mesons) and/or within a reduced fiducial phase space, which have very large extrapolation (fragmentation and phase space) factors, and feature significant lower cross section values. One motivation to provide such a long list of (even superseded) measurements is to observe the impact of several ingredients used in the cross sections derivation. One immediate observation of comparing the  $c\bar{c}$  cross sections for the same colliding system and c.m. energy is that the choice of “vacuum” (“medium”) charm-quark fragmentation fractions can reduce (enhance) the final quoted values by up to 30%. The rows highlighted in gray in Table I denote those that we consider to be the most accurate and/or precise  $\sigma(c\bar{c})$  determinations, which are then compared with the theoretical NNLO predictions in Fig. 11 later in this work. This selection is based on several criteria. First, in general we exclude the oldest

<sup>2</sup> For entries with multiple citations, the first one typically provides the numerical values listed, while the subsequent references describe similar previous (often superseded) measurements performed by the same experiment for the same colliding system and final states.

TABLE I. Experimental cross sections for charm-quark pair production in p-p, p- $\bar{p}$ , and p-A collisions from  $\sqrt{s} \approx 11$  GeV to 13 TeV. For each colliding system, we list the measured charmed hadrons (or their decay products), the fiducial ( $p_T, y, \eta, x_F, m_{\ell\ell}$ ) range, the hadron-to-charm-quark fragmentation fraction, the measured fiducial  $\sigma(c\bar{c})$  value, the extrapolation factor to the total phase space, and the final inclusive  $\sigma(c\bar{c})$  cross section. Whenever two (three) uncertainties are given, the first refers to statistical, the second to systematics plus extrapolation (the third to extrapolation alone) sources. Results indicated as ‘(t.w.)’ are obtained as described in the text, with only one total uncertainty quoted (quadratic sum of all uncertainties). Rows in gray indicate cross section values compared with theoretical ones in Fig. 11.

experiment ( $\sqrt{s}$ )	detected particles	fiducial kinematic phase space	$f(c \rightarrow h_c)$ fragmentation fraction	fiducial cross section ( $\mu\text{b}$ ) $\sigma \pm \Delta\sigma_{\text{stat}} \pm \Delta\sigma_{\text{sys}} \pm \Delta\sigma_{\text{ext}}$	full phase space extrapolation factor	total cross section (pp equiv.) ( $\mu\text{b}$ ) $\sigma \pm \Delta\sigma_{\text{stat}} \pm \Delta\sigma_{\text{sys}} \pm \Delta\sigma_{\text{ext}}$
ALICE (13 TeV pp) [77]	$D^0, D^+, D_s^+, D^{*+}, \Lambda_c^+, \Xi_c^+$	all $p_T,  y  < 0.5$	none ( $\sum h_c$ )	$2031 \pm 61^{+135+230}_{-141-140}$	$10^{+50\%}_{-10\%}$ (t.w.)	$20000^{+1000}_{-3000}$ (t.w.)
ALICE (13 TeV pp) [91]	$e^\pm$	all $p_T,  y  < 0.5$	PDG (2016)	$1200 \pm 400$ (t.w.)	$10^{+50\%}_{-10\%}$ (t.w.)	$12000^{+7000}_{-4000}$ (t.w.)
LHCb (13 TeV pp) [92]	$D^0, D^+, D_s^+, D^{*+}$	$p_T=0-8$ GeV, $2 < y < 4.5$	PDG (2008)	$2369 \pm 3 \pm 192$	$5^{+50\%}_{-30\%}$ (t.w.)	$12000 \pm 6000$ (t.w.)
CMS (13 TeV pp) [93]	$D^0, D^+, D^{*+}$	$p_T=4-100$ GeV, $ \eta  < 2.1$	13 TeV pp	$1200 \pm 200$ (t.w.)	$9.9^{+50\%}_{-10\%}$ (t.w.)	$12000^{+2000}_{-3000}$ (t.w.)
ALICE+LHCb comb. (13 TeV pp) [? ]	$D^0$	(combined)	13 TeV pp	(combined)	–	$17430^{+2700}_{-1960}$
LHCb (8.16 TeV pPb) [94]	$D^+, D_s^+$	$p_T=1-13$ GeV, $1.5 < y < 4, -5 < y < -2.5$	5.02 TeV pp	$5100 \pm 500$ (t.w.)	$3^{+50\%}_{-10\%}$ (t.w.)	$15000^{+8000}_{-2000}$ (t.w.)
ALICE (7 TeV pp) [51]	$D^0, D^+, D_s^+, \Lambda_c^+, \Xi_c^+$	all $p_T,  y  < 0.5$	5.02 TeV pp	$1347 \pm 97 \pm 104^{+163}_{-131}$	$8.6^{+50\%}_{-10\%}$ (t.w.)	$12000^{+6000}_{-2000}$ (t.w.)
ALICE (7 TeV pp) [95]	$e^\pm$	all $p_T,  y  < 0.5$	LEP+DIS (2005)	$1100 \pm 200^{+600+200}_{-700-100}$	$8.8^{+35\%}_{-10\%}$	$9700 \pm 1700^{+5200+3400}_{-5600-500}$
ALICE (7 TeV pp) [96]	$e^\pm$	$p_T > 0.4$ GeV, $ y  < 0.8$ , $m_{ee}=1.1-2.7$ GeV	PDG (2008)	–	–	$9700 \pm 3000$
ALICE (7 TeV pp) [97],[98]	$D^0, D^+, D^{*+}$	all $p_T,  y  < 0.5$	LEP+DIS (2005)	$1000^{+300}_{-400}$ (t.w.)	$8.5^{+60\%}_{-5\%}$	$8500 \pm 500^{+1100+5000}_{-3000-400}$
ALICE (7 TeV pp) [99]	$\Lambda_c^+$	$p_T=1-8$ GeV, $ y  < 0.5$	5.02 TeV pp	$1200^{+400}_{-300}$ (t.w.)	$10^{+50\%}_{-10\%}$ (t.w.)	$12000^{+7000}_{-4000}$ (t.w.)
ALICE (7 TeV pp) [100]	$D^0, D^+, D_s^+, D^{*+}$	all $p_T,  y  < 0.5$	LEP (2014)	$988 \pm 81^{+126}_{-206}$	$(8.57^{+2.52}_{-0.33})/1.034$	$8180 \pm 670^{+1010+2400}_{-1680-360}$
ALICE (7 TeV pp) [101]	$D^0, D^+, D_s^+, D^{*+}$	all $p_T,  y  < 0.5$	LEP (2014)	$954 \pm 69 \pm 97$	$(8.56^{+2.51}_{-0.42})/1.034$	$7890 \pm 570 \pm 760^{+2320}_{-450}$
LHCb (7 TeV pp) [49]	$D^0, D^+, D_s^+, D^{*+}, \Lambda_c^+$	$p_T < 8$ GeV, $2 < y < 4.5$	PDG (2008)	$1419 \pm 12 \pm 133$	–	–
ALICE+LHCb (7 TeV pp) [49, 101]	$D^0, D^+, D_s^+, D^{*+}, \Lambda_c^+$	(combined)	LEP (2014), PDG (2008)	(combined)	–	$7440 \pm 140 \pm 570^{+130}_{-70}$
ATLAS (7 TeV pp) [102]	$D^+, D_s^+, D^{*+}$	$p_T=3.5-100$ GeV, $ \eta  < 2.1$	LEP (2014)	$720 \pm 70$ (t.w.)	$(12-14)^{+44\%}_{-40\%}$	$8600 \pm 300 \pm 800^{+3800}_{-3400}$
CMS (7 TeV pp) [103]	$D^{*+}$	$p_T > \text{GeV}$ 1 GeV, $ \eta  < 2.5$	5.02 TeV pp	–	–	$9390^{+1350}_{-1490}$
CMS (7 TeV pp) [104]	$J/\psi, \psi(2S)$	$p_T^{J/\psi}=8-30$ GeV, $ y  < 2.4$	5.02 TeV pp	$85 \pm 15$ (t.w.)	–	–
CMS (7 TeV pp) [105]	$J/\psi$	$p_T^{J/\psi}=6.5-30$ GeV, $ y  < 2.4$	5.02 TeV pp	$140 \pm 30$ (t.w.)	–	–
ALICE (5.02 TeV pPb) [62]	$D^0, D^+, D_s^+, D^{*+}, \Lambda_c^+, \Xi_c^0$	all $p_T, -0.96 < y < 0.04$	5.02 TeV pPb	$1060 \pm 30^{+50}_{-60} \pm 150$	$16^{+50\%}_{-10\%}$	$8700^{+4600}_{-1600}$ (t.w.)
ALICE (5.02 TeV pp) [77] [106][107][108][51]	$D^0, D^+, D_s^+, D^{*+}, \Lambda_c^+, \Xi_c^+$	all $p_T,  y  < 0.5$	none ( $\sum h_c$ )	$1148 \pm 43^{+62+124}_{-65-84}$	$8.1^{+50\%}_{-10\%}$ (t.w.)	$9300^{+4800}_{-1300}$ (t.w.)
LHCb (5.02 TeV pp) [109]	$D^0, D^+, D_s^+, D^{*+}$	$p_T < 8$ GeV, $2 < y < 4.5$	PDG (2008)	$1193 \pm 3 \pm 89$	$4.8^{+50\%}_{-10\%}$ (t.w.)	$5700^{+2900}_{-700}$ (t.w.)
LHCb (5.02 TeV pPb) [110]	$D^0$	$p_T < 10$ GeV, $1.5 < y < 4, -5 < y < -2.5$	5.02 TeV pPb	$2800 \pm 200$ (t.w.)	$2.4^{+50\%}_{-10\%}$	$6800^{+3400}_{-800}$ (t.w.)
CMS (5.02 TeV pp) [111]	$J/\psi, \psi(2S)$	$p_T^{J/\psi}=6.5-50$ GeV, $ y  < 2.4$	5.02 TeV pp	$43^{+6}_{-6}$ (t.w.)	–	–
CMS (5.02 TeV pp) [112]	$D^0$	$p_T=2-100$ GeV, $ y  < 1$	5.02 TeV pp	$880 \pm 170$ (t.w.)	$7^{+50\%}_{-10\%}$ (t.w.)	$6100^{+3300}_{-1300}$ (t.w.)
CMS (5.02 TeV pp) [50]	$\Lambda_c^+$	$p_T=5-20$ GeV, $ y  < 1$	5.02 TeV pp	$60 \pm 20$ (t.w.)	$40^{+50\%}_{-10\%}$ (t.w.)	$2300^{+1500}_{-900}$ (t.w.)
ALICE+LHCb+CMS (5.02 TeV pp) [113]	$D^0, D^{*+}, D^+, D_s^+, \Lambda_c^+, \Xi_c^+$	(combined)	dynamical hadronisation	(combined)	–	$8340^{+220+370+769}_{-220-370-460}$
ALICE (2.76 TeV pp) [98]	$D^0, D^+, D^{*+}$	all $p_T,  y  < 0.5$	LEP+DIS (2005)	$660^{+280}_{-240}$ (t.w.)	$7.3^{+60\%}_{-10\%}$	$4800 \pm 800^{+1000+2600}_{-300-400}$
ALICE (2.76 TeV pp) [51]	$D^0, D^+, D_s^+, \Lambda_c^+, \Xi_c^+$	all $p_T,  y  < 0.5$	5.02 TeV pp	$1126 \pm 303^{+258+420}_{-429-140}$	$7.3^{+50\%}_{-10\%}$ (t.w.)	$8200^{+5900}_{-4100}$ (t.w.)
CDF (1.96 TeV $p\bar{p}$ ) [114]	$D^+$	$p_T = 1.5-14.5$ GeV, $ y  < 1$	LEP (2014)	$320 \pm 50$ (t.w.)	$5.2^{+50\%}_{-10\%}$ (t.w.)	$1700^{+900}_{-300}$ (t.w.)
PHENIX (0.2 TeV pp) [115]	$e^+, \mu^+$	–	PDG (2006)	–	–	$538 \pm 46 \pm 197 \pm 174$
PHENIX (0.2 TeV pp) [116]	$e^\pm$	all $p_T,  y  < 0.5$	PDG (2006)	$118 \pm 8 \pm 50$	4.6	$544 \pm 39 \pm 142 \pm 200$
PHENIX (0.2 TeV pp) [117]	$e^\pm$	all $p_T,  y  < 0.5$	PDG (2006)	$130 \pm 70$ (t.w.)	3.4 $\pm$ 0.2	$440 \pm 230$
PHENIX (0.2 TeV dAu) [117]	$e^\pm$	–	PDG (2006)	–	–	$490 \pm 280$
PHENIX (0.2 TeV pp) [118]	$e^\pm$	all $p_T,  y  < 0.5$	PDG (2006)	$200 \pm 30 \pm 110$	4.6	$920 \pm 150 \pm 540$
PHENIX (0.2 TeV pp) [119]	$e^\pm$	all $p_T,  y  < 0.5$	PDG (2006)	$123 \pm 12 \pm 37$	4.6	$567 \pm 57 \pm 193$
PHENIX (0.2 TeV pp) [120]	$e^\pm$	all $p_T,  y  < 0.5$	PDG (2006)	$119 \pm 12 \pm 38$	4.6	$551 \pm 57 \pm 195$
STAR (0.2 TeV pp) [121]	$D^0, D^+$	all $p_T,  y  < 0.5$	PDG (2008)	$170 \pm 45^{+38}_{-39}$	4.7 $\pm$ 0.7	$797 \pm 210^{+171}_{-270} \pm 119$
LHCb (86.6 GeV pHe) [122]	$J/\psi, D^0$	all $p_T, 2 < y < 4.6$	LEP (2014)	$75 \pm 10$ (t.w.)	1.93	$144 \pm 12 \pm 4$
LHCb (68.5 GeV pNe) [123]	$D^0$	all $p_T, -2.29 < y < 0$	LEP (2014)	$45 \pm 5$ (t.w.)	2.02	$90 \pm 10$ (t.w.)
HERA-B (41.6 GeV pA, A=C,Ti,W) [124]	$D^0, D^+, D_s^+, D^{*+}$	all $p_T, x_F \in [-0.15, 0.05]$	PDG (2006)	$27 \pm 5$ (t.w.)	1.82 $\pm$ 0.17	$49 \pm 5 \pm 7$
E653 (38.9 GeV pA, A=plastic) [125]	$\mu^+$	–	LEP (1999)	–	–	$48 \pm 6 \pm 11$
E789 (38.8 GeV pAu) [126][127]	$D^0, \bar{D}^0$	–	LEP (2014)	–	–	$14 \pm 5$ (t.w.)
E743 (38.2 GeV pp) [126][128]	$D^0, D^+$	–	LEP (1999)	–	–	$29^{+6}_{-5} \pm 5$
NA50 (28.9 GeV pA) [126][129]	$J/\psi$	–	LEP (1999)	–	–	$36 \pm 9$
NA27 (27.4 GeV pp) [126][130]	$D^0, D^+, D^+$	–	LEP (1999)	–	–	$18 \pm 2$
NA16 (26.0 GeV pp) [126][131]	$D^0, D^+$	–	LEP (1999)	–	–	$19^{+10}_{-6}$
E769 (21.7 GeV pA, A=mixed) [126][132]	$D^0, D^+, D_s^+, D^+, \Lambda_c^+$	–	LEP (1999)	–	–	$11 \pm 2 \pm 0.8$
NA32 (19.5 GeV pA) [126][133, 134]	$D^0, D^+, D_s^+$	–	LEP (1999)	–	–	$3 \pm 1$
SVD-1 (11.6 GeV pp) [135]	$D^0, D^+$	–	LEP (1999)	–	–	$2^{+1}_{-0.7} \pm 0.3$
SVD-2 (11.6 GeV pA, A=C,Si,Pb) [136]	$D^0, \bar{D}^0, D^+, \Lambda_c^+$	–	none ( $\sum h_c$ )	–	–	$7 \pm 2 \pm 1$

results that have been superseded by, or combined into, a more recent measurement by the same collaboration(s). The selected results typically cover similar kinematics as the older extractions, but feature smaller uncertainties and/or more detected particles. Second, in general LHC cross sections derived from the sum of “all” charmed hadrons (indicated as ‘ $\sum h_c$ ’ in the table), are preferred over those obtained from fragmentation fractions,  $f(c \rightarrow h_c)$ . Third, p-p collisions are prioritized over proton-nucleus collisions to minimize uncertainties due to nuclear PDFs, unless no p-p data are available at a given  $\sqrt{s}$  value. We note that a few of the values in Table I that combine measurements from independent LHC collaborations, such as [113, 139], have not been officially obtained by the quoted LHC collaborations themselves.

### C. Measurements of $b\bar{b}$ cross sections

Table II collects about 50 measurements of bottom cross sections in hadronic collisions from  $\sqrt{s} \approx 40$  GeV (fixed target) to 13 TeV (LHC). The descriptions of the columns of Table II follow those for the corresponding charm-quark Table I, except that now the bottom fragmentation fraction is not listed as the analyses use different ( $b \rightarrow h_b$ ), ( $b \rightarrow h_b \rightarrow h_c$ ), or ( $b \rightarrow h_b \rightarrow h_c \rightarrow \ell^\pm$ ) decay chains, as discussed previously, and in general the bottom-quark fragmentation fractions implemented in the MC generators employed to correct the experimental measurements follow closely the LEP percentages shown in Fig. 3.

About half of the values of the table, marked as ‘(this work)’, have been obtained here as done for the charm-quark case, by adding up the b-hadrons fiducial cross sections, and then converting those to quark-level cross section via LEP bottom fragmentation fractions (Fig. 3). As done for the similar  $\sigma(c\bar{c})$  cross sections derived in the previous section, the fiducial phase-space extrapolation factors are either taken directly from the original papers, or estimated here from FONLL predictions for each colliding system, using the central CTEQ6.6 PDFs (except for 8.16 TeV where we used NNPDF30\_nlo\_as\_0118) and conservatively assigning uncertainties of  $\pm 20\%$  (for the b-hadrons) or  $\pm 50\%$  (for the displaced leptons) based on the maximum envelope of differences found between our estimates and other factors used in the literature. All our derived ‘(t.w.)’ results are consistent within uncertainties with the extractions obtained directly by the experimental collaborations. For p-p collisions at  $\sqrt{s} = 7$  TeV, we have extrapolated six fiducial cross-section measurements from CMS, corresponding to various different b-quark final states, which all yield mutually consistent  $\sigma(b\bar{b})$  cross section values. We thus provide their combination, obtained as a standard average of the individual measurements. The resulting  $\sigma(b\bar{b}) = 300 \pm 100 \mu\text{b}$  value, with a conservative uncertainty assigned, has been also added to the table. The experimental results listed in gray are considered the most accurate and/or precise determinations (often based on the most recent measurements, and following similar criteria as discussed previously for the charm cross sections), and are selected for comparison with theoretical NNLO predictions in Fig. 14 later on. We note that the entry of Ref. [140], which combines ALICE and LHCb data, does not correspond to an official combination of measurements by these LHC collaborations.

TABLE II. Experimental cross sections for bottom-quark pair production in p-p, p- $\bar{p}$ , and p-A collisions over  $\sqrt{s} \approx 40$  GeV–13 TeV. For each colliding system, we list the measured bottom hadrons or their nonprompt (‘n.p.’) decay products, the fiducial ( $p_T$ ,  $y$ ,  $\eta$ ,  $x_F$ ,  $m_{\ell\ell}$ ) range, the measured fiducial  $\sigma(\text{b}\bar{\text{b}})$  value, and the final inclusive  $\sigma(\text{b}\bar{\text{b}})$  cross section derived. Whenever two (three) uncertainties are given, the first refers to statistical, the second to systematics plus extrapolation (and the third to extrapolation) sources. Results indicated as ‘(t.w.)’ (‘this work’) are obtained as described in the text, with only one total uncertainty quoted (quadratic sum of all uncertainties). Rows in gray indicate cross section values compared with theoretical ones in Fig. 14.

experiment ( $\sqrt{s}$ )	detected particles	fiducial kinematic phase space	fiducial cross section (nb) $\sigma \pm \Delta\sigma_{\text{stat}} \pm \Delta\sigma_{\text{sys}} \pm \Delta\sigma_{\text{extr}}$	full phase space extrapolation factor	total cross section (pp equiv.) (nb) $\sigma \pm \Delta\sigma_{\text{stat}} \pm \Delta\sigma_{\text{sys}} \pm \Delta\sigma_{\text{extr}}$
ALICE (13.6 TeV pp) [141]	$B^0$	all $p_T$ , $ y  < 0.5$	$(59^{+35}_{-35}) \times 10^3$	7.6 $\pm$ 20% (t.w.)	$(450 \pm 280) \times 10^3$ (t.w.)
ALICE (13 TeV pp) [142]	$D^0, D^+, \Lambda_b^+, \Lambda_c^+$ (n.p.)	all $p_T$ , $ y  < 0.5$	$(75.2 \pm 3.2 \pm 5.2^{+12.3}_{-3.2}) \times 10^3$	7.3 $\pm$ 20% (t.w.)	$(550^{+150}_{-120}) \times 10^3$ (t.w.)
ALICE (13 TeV pp) [91]	$e^+$ (from b)	all $p_T$ , $ y  < 0.5$	$(63.5^{+14}_{-14} \pm 9^{+15.5}_{-15.5}) \times 10^3$	7.3 $\pm$ 20% (t.w.)	$(460 \pm 190) \times 10^3$ (t.w.)
LHCb (13 TeV pp) [143]	all $h_b$	all $p_T$ , $2 < \eta < 5$	$(144 \pm 1 \pm 21) \times 10^3$	3.9	$(560 \pm 4 \pm 82) \times 10^3$
LHCb (13 TeV pp) [144]	$B^{\pm}$	$p_T=0-40$ GeV, $2 < y < 4.5$	$(110 \pm 10) \times 10^3$ (t.w.)	4.9 $\pm$ 20%	$(520 \pm 110) \times 10^3$ (t.w.)
LHCb (13 TeV pp) [145]	$J/\psi$ (n.p.)	$p_T=0-14$ GeV, $2 < y < 4.5$	$(970 \pm 5 \pm 60) \times 10^3$	–	$(495 \pm 2 \pm 52) \times 10^3$
ALICE+LHCb comb. (13 TeV pp) [140]	$D^0, J/\psi$ (n.p.)	–	–	–	$(500 \pm 40) \times 10^3$
CMS (13 TeV pp) [146]	$B^+$	$p_T=10-100$ GeV, $ y  < 1.45$	$(71 \pm 5) \times 10^3$ (t.w.)	9.7 $\pm$ 20% (t.w.)	$(680 \pm 150) \times 10^3$ (t.w.)
LHCb (8.16 TeV pPb) [147]	$B^+, B^0, \Lambda_b$	$p_T=2-20$ GeV, $1.5 < y < 3.5, -4.5 < y < 2.5$	$(96 \pm 12) \times 10^3$ (t.w.)	3.5 $\pm$ 20% (t.w.)	$(340 \pm 80) \times 10^3$ (t.w.)
ALICE (7 TeV pp) [148]	$J/\psi$ (n.p.)	all $p_T$ , $ y  < 0.5$	$(43^{+11}_{-11} \pm 9^{+0.6}_{-1.5}) \times 10^3$	4.49 $^{+0.12}_{-0.10}$	$(282 \pm 74^{+59}_{-68}) \times 10^3$
ALICE (7 TeV pp) [95]	$e^+$ (from b)	all $p_T$ , $ y  < 0.5$	$(57.7 \pm 3.2 \pm 17.6) \times 10^3$	–	$(383 \pm 21 \pm 118) \times 10^3$
ALICE (7 TeV pp) [95]+[148]	$e^+, J/\psi$ (n.p.)	–	–	–	$(322 \pm 45^{+39}_{-63}) \times 10^3$
ALICE (7 TeV pp) [96]	$e^+$ (from b)	$p_T^{\text{cc}} < 8$ GeV, $m_{\text{cc}} < 3.3$ GeV, $ y  < 0.8$	–	–	$(170 \pm 100) \times 10^3$
LHCb (7 TeV pp) [143]	all $h_b$	all $p_T$ , $2 < \eta < 5$	$(72 \pm 0.3 \pm 6.8) \times 10^3$	4.1	$(295 \pm 1 \pm 28) \times 10^3$
LHCb (7 TeV pp) [149]	$B^0, B^+, B_s$	$p_T < 40$ GeV, $2 < y < 4.5$	$(48 \pm 6) \times 10^3$ (t.w.)	5.1 $\pm$ 20% (t.w.)	$(240 \pm 60) \times 10^3$ (t.w.)
LHCb (7 TeV pp) [150]	$B^+$	$p_T < 40$ GeV, $2 < y < 4.5$	$(51 \pm 5) \times 10^3$ (t.w.)	5.1 $\pm$ 20% (t.w.)	$(260 \pm 60) \times 10^3$ (t.w.)
LHCb (7 TeV pp) [151]	$D^0$ (n.p.)	all $p_T$ , $2 < \eta < 6$	$(75.3 \pm 5.4 \pm 13) \times 10^3$	3.77 (3.61)	$(284 \pm 20 \pm 49) \times 10^3$
LHCb (7 TeV pp) [152]	$J/\psi$ (n.p.)	$p_T < 14$ GeV, $2 < y < 5$	$(49 \pm 7) \times 10^3$ (t.w.)	5.88 (5.21)	$(288 \pm 4 \pm 48) \times 10^3$
CMS (7 TeV pp) [153]	$B^+$	$p_T > 5$ GeV, $ y  < 2.4$	$(69 \pm 11) \times 10^3$ (t.w.)	3.45 $\pm$ 20% (t.w.)	$(240 \pm 60) \times 10^3$ (t.w.)
CMS (7 TeV pp) [154]	$B^0$	$p_T > 5$ GeV, $ y  < 2.2$	$(82 \pm 11) \times 10^3$ (t.w.)	3.7 $\pm$ 20% (t.w.)	$(300 \pm 70) \times 10^3$ (t.w.)
CMS (7 TeV pp) [155]	$B_s$	$p_T=8-50$ GeV, $ y  < 2.4$	$(66 \pm 8) \times 10^3$ (t.w.)	7.6 $\pm$ 20% (t.w.)	$(500 \pm 120) \times 10^3$ (t.w.)
CMS (7 TeV pp) [156]	$\Lambda_b$ (n.p.)	$p_T > 10$ GeV, $ y  < 2.0$	$(25 \pm 13) \times 10^3$ (t.w.)	14.2 $\pm$ 20% (t.w.)	$(350 \pm 200) \times 10^3$ (t.w.)
CMS (7 TeV pp) [105]	$J/\psi$ (n.p.)	$p_T^{J/\psi} = 6.5-30$ GeV, $ y  < 2.4$	$(19 \pm 3) \times 10^3$ (t.w.)	15 $\pm$ 20% (t.w.)	$(280 \pm 70) \times 10^3$ (t.w.)
CMS (7 TeV pp) [104]	$J/\psi$ (n.p.)	$p_T^{J/\psi} = 8-30$ GeV, $ y  < 2.4$	$(10^{+1}_{-1}) \times 10^3$	26 $\pm$ 20% (t.w.)	$(260 \pm 60) \times 10^3$ (t.w.)
	$\psi(2S)$ (n.p.)	$p_T^{\psi(2S)} = 6.5-30$ GeV, $ y  < 2.4$	$(20^{+2}_{-2}) \times 10^3$	11.5 $\pm$ 20% (t.w.)	$(230 \pm 60) \times 10^3$ (t.w.)
CMS average (7 TeV pp) (t.w.)	(combined)	(combined)	(combined)	–	$(300 \pm 100) \times 10^3$ (t.w.)
CMS (7 TeV pp) [157]	$\mu^+\mu^+$ (from b)	$p_T^{\mu^+\mu^+} > 4$ GeV, $ \eta_{\mu}  < 2.1$	$2200 \pm 300$ (t.w.)	–	–
CMS (7 TeV pp) [158]	$\mu^{\pm}$ (from b)	$p_T^{\mu^{\pm}} > 6$ GeV, $ \eta_{\mu}  < 2.1$	$3200 \pm 800$ (t.w.)	60 $\pm$ 50% (t.w.)	$(190 \pm 110) \times 10^3$ (t.w.)
ATLAS (7 TeV pp) [159]	$B^+$	$p_T=9-120$ GeV, $ y  < 2.25$	$(26 \pm 3) \times 10^3$ (t.w.)	10 $\pm$ 20% (t.w.)	$(260 \pm 60) \times 10^3$ (t.w.)
ALICE (5.02 TeV pp) [106]	$D^0, D^+, D^{*+}$ (n.p.)	all $p_T$ , $ y  < 0.5$	$(34.5 \pm 2.4 \pm 2.5^{+3.9}_{-1.4}) \times 10^3$	6.2 $\pm$ 20% (t.w.)	$(210^{+60}_{-50}) \times 10^3$ (t.w.)
LHCb (5.02 TeV pp) [160]	$J/\psi$ (n.p.)	$p_T^{J/\psi} < 20$ GeV, $2 < y < 4.5$	$(35 \pm 2) \times 10^3$ (t.w.)	5.4 $\pm$ 20% (t.w.)	$(190 \pm 40) \times 10^3$ (t.w.)
ALICE+LHCb comb. (5.02 TeV pp) [140]	$D^0, J/\psi$ (n.p.)	all $p_T$ , $ y  < 0.5$	$(29.6 \pm 2.4) \times 10^3$	–	$(191 \pm 16) \times 10^3$
CMS (5.02 TeV pp) [161]	$D^0$ (n.p.)	$p_T=2-100$ GeV, $ y  < 1.0$	$(31 \pm 5) \times 10^3$ (t.w.)	5.7 $\pm$ 20% (t.w.)	$(180^{+50}_{-50}) \times 10^3$ (t.w.)
CMS (5.02 TeV pp) [162]	$B^{\pm}$	$p_T=7-50$ GeV, $ y  < 2.4$	$(16 \pm 2) \times 10^3$ (t.w.)	7 $\pm$ 20% (t.w.)	$(220 \pm 50) \times 10^3$ (t.w.)
ALICE (2.76 TeV pp) [163]	$e^+$ (from b)	all $p_T$ , $ y  < 0.5$	$(29.1 \pm 2.6^{+0.8}_{-11.7}) \times 10^3$	5.57	$(162 \pm 14^{+56}_{-65}) \times 10^3$
CDF (1.96 TeV pp) [164]	$J/\psi$ (n.p.)	all $p_T$ , $ y  < 0.6$	$(17.6 \pm 0.4 \pm 2.5^{+2.5}_{-2.3}) \times 10^3$	4.3 $\pm$ 20% (t.w.)	$(76^{+19}_{-18}) \times 10^3$ (t.w.)
UA1 (0.63 TeV p $\bar{p}$ ) [165]	$J/\psi, \mu^{\pm}$ (from b)	all $p_T$ , $ \eta  < 1.5$	$(12.8 \pm 4.7 \pm 6) \times 10^3$	–	$(19.3 \pm 7 \pm 9) \times 10^3$
UA1 (0.63 TeV p $\bar{p}$ ) [166]	$\mu^{\pm}$ (from b)	all $p_T$ , $ \eta  < 1.5$	$(13 \pm 2.8 \pm 6.9^{+6.9}_{-4.3}) \times 10^3$	–	$(19.7 \pm 4^{+10.4}_{-6.5}) \times 10^3$
PHENIX (0.51 TeV pp) [167]+[168]	$J/\psi$ (n.p.)	all $p_T$ , $1.2 <  y  < 2.2$	$3630^{+1920}_{-1700}$	3.3 $\pm$ 20% (t.w.)	$(12^{+7}_{-6}) \times 10^3$ (t.w.)
PHENIX (0.51 TeV pp) [169]	$\mu^{\pm}\mu^{\pm}$ (from b)	$p_T^{\mu^{\pm}} > 1$ GeV, $1.2 <  y  < 2.2$ , $m_{\mu\mu} = 5-10$ GeV	$26 \pm 5$ (t.w.)	500	$(13.1 \pm 0.6 \pm 1.5 \pm 2.7) \times 10^3$
PHENIX (0.2 TeV pp) [170]	$e^+$ (from b)	all $p_T$ , $ y  < 0.5$	$920^{+340}_{-310} \pm 390^{+360}_{-360}$	3.5 $\pm$ 8%	$3200^{+1200}_{-1100} \pm 1400^{+3000}_{-2000}$
PHENIX (0.2 TeV pp) [116]	$e^+$ (from b)	$p_T^e > 0.2$ GeV, $ y  < 0.35$	–	–	$3900 \pm 2500^{+3000}_{-2000}$
PHENIX (0.2 TeV pp) [117]	$e^+$ (from b)	$p_T^e > 0.2$ GeV, $ y  < 0.35$	–	–	$3900 \pm 1300$
PHENIX (0.2 TeV dAu) [171]	$e^+$ (from b)	all $p_T$ , $ y  < 0.5$	$1370 \pm 280 \pm 460$	2.5	$3400 \pm 800 \pm 1100$
PHENIX (0.2 TeV dAu) [117]	$e^+$ (from b)	$p_T > 0.2$ GeV, $ y  < 0.35$	–	–	$2800 \pm 1300$
PHENIX (0.2 TeV pp) [172] [173]	$J/\psi$ (n.p.)	all $p_T$ , $1.2 <  y  < 2.2$	$510 \pm 130 \pm 200$	–	$3800 \pm 900 \pm 1600$
PHENIX (0.2 TeV pp) [173]	$\mu^{\pm}\mu^{\pm}$ (from b)	all $p_T$ , $1.2 <  y  < 2.2$	$460 \pm 90$ (t.w.)	–	$3750 \pm 240^{+350}_{-500} \pm 450$
STAR (0.2 TeV pp) [174]	$e^+$ (from b)	$p_T^e = 3-10$ GeV, $ \eta  < 0.5$	$9.8 \pm 2.8$ (t.w.)	–	$4000 \pm 500 \pm 100$
HERA-B (41.6 GeV pA, A=C,Ti) [175]	$J/\psi$ (n.p.)	$x_F \in [-0.25, 0.15]$	–	–	$32^{+14}_{-12} \pm 6$
HERA-B (41.6 GeV pA, A=C,Ti) [126, 176]	$J/\psi$ (n.p.)	$x_F \in [-0.35, 0.15]$	–	–	$14.9 \pm 2.2 \pm 2.3$
HERA-B (41.6 GeV pA, A=C,Ti,W) [177]+[176]	$\mu^{\pm}$ (from b)	$x_F \in [-0.3, 0.15]$	–	–	$15.8 \pm 1.7 \pm 2.3$
E771 (38.7 GeV pSi) [126, 178]	$\mu^{\pm}$ (from b)	$p_T^{\mu^{\pm}} > 6$ GeV, $x_F^{\mu^{\pm}} \in [-0.25, 0.5]$	–	–	$43^{+27}_{-7} \pm 7$
E789 (38.7 GeV pAu) [126, 179]	$J/\psi$ (n.p.)	$p_T^{J/\psi} < 2$ GeV, $x_F^{J/\psi} \in [0, 0.1]$	–	–	$5.7 \pm 1.5 \pm 1.2$

### III. THEORETICAL PREDICTIONS

The scattering process of interest in this work is the inclusive production of a heavy-quark pair ( $Q\bar{Q}$ ) in p-p collisions,  $p(k_1) + p(k_2) \rightarrow Q\bar{Q} + X$ , where  $k_i$  are the incoming momenta of the protons, leading to a collision with squared c.m. energy  $s = (k_1 + k_2)^2$ . The final state is required to have a massive on-shell quark-antiquark pair, implicitly assuming an integration over their momenta. We compare two different theoretical frameworks, based on the fixed flavour number (FFN) scheme and the general-mass variable flavour number scheme (GM-VFNS). In the FFN scheme, the number of active light-parton flavours is fixed ( $N_f = 3, 4$  for charm and bottom, respectively), and heavy quarks such as charm and bottom are not included as proton partons, but are produced explicitly in the hard scattering with their full mass dependence retained. At NLO and beyond, the expressions for the total cross section involve logarithmic terms proportional to  $\log(s/m_Q^2)$  which can potentially become large as the c.m. energy grows. In the GM-VFNS schemes, these logarithmic terms are summed up through the DGLAP renormalization group equations by introducing scale-dependent heavy-quark PDFs and FFs.

#### A. FFN scheme: NNLO calculations

First, we focus on fixed-order predictions within the FFN scheme with  $N_f$  light (massless) quarks  $q$  and a single heavy (massive) quark  $Q$ . The hadronic cross section  $\sigma^{p-p \rightarrow Q\bar{Q}+X}$  can be schematically expressed as a convolution of the PDFs  $f(x, \mu_F^2)$  of the colliding hadrons, and the perturbative computable partonic cross section  $\hat{\sigma}^{ij \rightarrow Q\bar{Q}+X}$ , as

$$\sigma^{p-p \rightarrow Q\bar{Q}+X}(s, m_Q^2, \mu_F^2, \mu_R^2) = \sum_{i,j} \int_{x_{\min}}^1 dx_1 dx_2 f_i(x_1, \mu_F^2) f_j(x_2, \mu_F^2) \hat{\sigma}^{ij \rightarrow Q\bar{Q}+X}(\hat{s} = x_1 x_2 s, m_Q^2, \mu_F^2, \mu_R^2), \quad (4)$$

where the dependence on the factorization scale  $\mu_F$ , introduced by the collinear factorization, and the renormalization scale  $\mu_R$ , introduced by the  $\alpha_s$  running, are explicitly indicated. Unless otherwise specified, we adopt  $\mu_F = \mu_R = 2m_Q$  as the default scale choice, corresponding to the rest mass of the heavy-quark pair system. The sum of initial-state partons  $i, j$  includes light quarks ( $q, \bar{q}$ ) and gluons ( $g$ ), but not heavy quarks  $Q$ , with the full mass dependence  $m_Q$  retained in the matrix elements, i.e. we only consider the perturbative generation of heavy quarks, e.g.  $gg \rightarrow Q\bar{Q}$  and  $q\bar{q} \rightarrow Q\bar{Q}$ , and neglect any contributions from intrinsic heavy-quark PDFs [180]. The cross section integration ranges in  $x_{1,2}$  of Eq. (4) extend up to the kinematic upper limit of unity, while the lower limit is given by

$$x_{\min} = \frac{4m_Q^2}{s}, \quad (5)$$

which reflects the minimum partonic energy ( $\hat{s} = 4m_Q^2$ ) required to produce a heavy-quark pair at rest.

The details of the NNLO PDFs employed in this work, NNPDF4.0 [17], CT18 [19], and MSHT20 [18], are listed in Table III. For each PDF set, the following information is provided: number of effective quark flavours ( $N_f = 3, 4$ , relevant for  $c\bar{c}$  and  $b\bar{b}$  production, respectively), minimum parton momentum fraction ( $x_{\text{gridmin}}$ ) and virtuality ( $Q_{\min}$ ), charm and bottom masses ( $m_c, m_b$ ), and type of error and number of replicas or eigenvectors used for the PDF uncertainty estimate. All PDFs adopt a reference value  $\alpha_s(m_Z) = 0.118$ , defined as the value obtained by evolving  $\alpha_s(Q_{\min})$  to the scale  $m_Z$  within the VFNS scheme (up to  $N_f = 5$ ). For consistency with the FFN scheme, all PDF sets used do not contain any intrinsic charm in the initial proton densities, i.e. the charm distribution  $f_c(x, Q^2)$  is exactly zero at the initial scale and arises solely from pQCD evolution, e.g. through  $g \rightarrow c\bar{c}$  splitting. For the NNPDF4.0 densities, this latter condition is achieved using the perturbative-charm ('pch') set, as the default set uses intrinsic charm [180]. The NNPDF40\_nnlo\_pch\_as\_01180\_nf\_3 and NNPDF40\_nnlo\_as\_01180\_nf\_4 parton densities are used as our default PDF choices for  $c\bar{c}$  and  $b\bar{b}$  production, respectively.

The currently highest available fixed-order perturbative accuracy for heavy-quark production is NNLO, with the corresponding coefficient functions computed in Refs. [10–14, 181]. Hence, we further decompose the partonic cross section as

$$\hat{\sigma}^{ij \rightarrow Q\bar{Q}+X}(\hat{s}, m_Q^2, \mu_F^2, \mu_R^2) = \sum_{k=0}^2 \left( \frac{\alpha_s(\mu_R^2)}{4\pi} \right)^{2+k} \hat{\sigma}_k^{ij \rightarrow Q\bar{Q}+X}(\hat{s}, m_Q^2, \mu_F^2, \mu_R^2), \quad (6)$$

with these coefficient functions implemented into the new MaunaKea code. In practice, we have taken them from TOP++ [11], and MaunaKea differs from the latter in three relevant aspects: (i) the number of light flavours ( $N_f$ )

TABLE III. List of the NNLO PDFs used in the calculations, with their characteristics: number of effective quark flavours ( $N_f = 3, 4$ ), minimum parton momentum fraction ( $x_{\text{gridmin}}$ ) and virtuality ( $Q_{\text{min}}$ ), charm and bottom masses ( $m_c, m_b$ ), and type of error and number of replicas or eigenvectors used.

PDF set family	LHAPDF set name	$N_f$	$x_{\text{gridmin}}$	$Q_{\text{min}}$ [GeV]	$m_c$ [GeV]	$m_b$ [GeV]	# replicas/eigenvectors
NNPDF4.0	NNPDF40_nnlo_pch_as_01180_nf_3	3	$10^{-9}$	1.0	1.51	–	100 (68% CL)
	NNPDF40_nnlo_as_01180_nf_4	4	$10^{-9}$	1.65	–	4.92	100 (68% CL)
CT18	CT18NNLO_NF3	3	$10^{-9}$	1.295	1.30	–	58 (Hessian 90% CL)
	CT18NNLO_NF4	4	$10^{-9}$	1.295	–	4.75	58 (Hessian 90% CL)
MSHT20	MSHT20nnlo_nf3	3	$10^{-6}$	1.0	1.40	–	64 (Hessian 68% CL)
	MSHT20nnlo_nf4	4	$10^{-6}$	1.0	–	4.75	64 (Hessian 68% CL)

is dynamic and not fixed, so it can be used to predict any heavy-quark (and not just  $t\bar{t}$ ) production, (ii) `MaunaKea` is interfaced to `PineAPPL` to produce fast interpolation grids that are PDF-independent and allow setting arbitrary factorization and renormalization scales (effectively, this turns Eq. (4) into a fast matrix operation), and (iii) `MaunaKea` currently does not support soft gluon resummation, i.e. all predictions are at fixed order. The `MaunaKea` code has been extensively benchmarked against predictions by both `TOP++` [12] and `HATHOR` [10]. The code can be downloaded online [68, 182].

We note that the FFN scheme coefficient functions in Eq. (6) are obtained in the pole-mass (on-shell) renormalization scheme i.e. the mass that appears in the coefficient functions is the same as the one that sets the kinematic boundaries, e.g. in Eq. (5). The perturbative convergence of the FFN scheme cross section calculation is known to be improved when using the  $\overline{\text{MS}}$  running-mass scheme compared with the pole-mass (on-shell) renormalization scheme [183]. Furthermore, the pole-mass definition carries an intrinsic uncertainty of order  $\Lambda_{\text{QCD}}$  due to renormalon contributions [183, 184]. This ambiguity is not included in the uncertainties of the pole-mass values quoted by the PDG [185], which are obtained perturbatively from the best determinations of the running masses. However, in this work we still adopt the pole-mass definition for the charm and bottom quarks, as it is the convention commonly used in PDF fits, and we will nevertheless need to specify the pole masses to set the kinematic boundaries, e.g. in Eq. (5).

#### Missing higher-order uncertainties

We start by estimating the size of the theoretical uncertainties associated with missing higher-order corrections for increasing pQCD accuracies, and examining the perturbative convergence of the heavy-quark cross section calculations. Figure 4 shows the inclusive cross sections for  $c\bar{c}$  (left) and  $b\bar{b}$  (right) production in p-p collisions as a function of  $\sqrt{s}$  predicted at LO, NLO, and NNLO accuracy. All predictions have been calculated by using the same NNLO PDF, i.e. the differences between the different-order calculations are due to the coefficient functions. The use of NNLO PDFs in conjunction with LO or NLO coefficient functions does not formally improve the perturbative accuracy of the calculation but, by keeping the PDFs fixed, it provides insight into how the full NNLO result is built up. The error bands around the central curves indicate the missing higher-order theoretical uncertainty obtained through a 7-point scale variation, whereby the  $\mu_F$  and  $\mu_R$  scales are varied within factors of two (excluding variations in opposite directions) around our default scale choice of  $\mu_F = \mu_R = 2m_Q$ . The middle panels show the cross sections normalized to the NNLO predictions, and the bottom panels the so-called  $K$ -factors, namely, the ratios between cross sections obtained at a higher over the immediately lower pQCD accuracy. Despite the reduction in relative scale uncertainties when going from LO to NNLO, they remain substantial at NNLO, amounting on average to approximately  $-40\%$  and  $+100\%$  for charm and  $\pm 25\%$  for bottom, over the considered  $\sqrt{s}$  range. We also observe that the central NNLO predictions are always outside the LO scale-variation bands and only barely within the NLO bands. In addition, the  $K$ -factors are quite large: for  $c\bar{c}$  production the cross sections augment by up to a factor of three from LO to NLO and still by a factor of two from NLO to NNLO, while for  $b\bar{b}$  production we find slightly smaller ratios, which indicates a better perturbative convergence with increasing heavy-quark mass. All in all, the perturbative corrections are large. This slow perturbative convergence can be linked to the relatively large values of the expansion parameter,  $\alpha_s(\mu_R)$ , at the low scales of relevance for charm and bottom pair production, and possibly also to the size of the logarithmic terms  $\sim \log(s/m_Q^2)$ . The large  $K$ -factors could also be due to other large contributions in the partonic cross sections that would require resummation, including the threshold and/or small- $x$  logarithms. In particular, in the high-energy

(small- $x$ ) regime probed by charm production, resummation of  $\log(x)$ -type terms may be required to achieve more perturbatively stable predictions [186–190]. A consistent resummation framework requires both resummed PDFs and resummed partonic cross sections, which is beyond the scope of this study. Note that the high-energy resummation applicable for  $\hat{s} \rightarrow \infty$  is opposite to the threshold resummation applicable for  $\hat{s} \rightarrow 4m_Q^2$  (which `top++` can perform up to NNLL accuracy, but is not available in `MaunaKea`), and is orthogonal to the resummation of  $\log(s/m_Q^2)$  terms originating from collinear radiation discussed in Section III B. The calculation of beyond-NNLO perturbative corrections is mathematically challenging because of the increasingly large number of real and virtual gluon emission diagrams possible, and the presence of massive final-state particles.

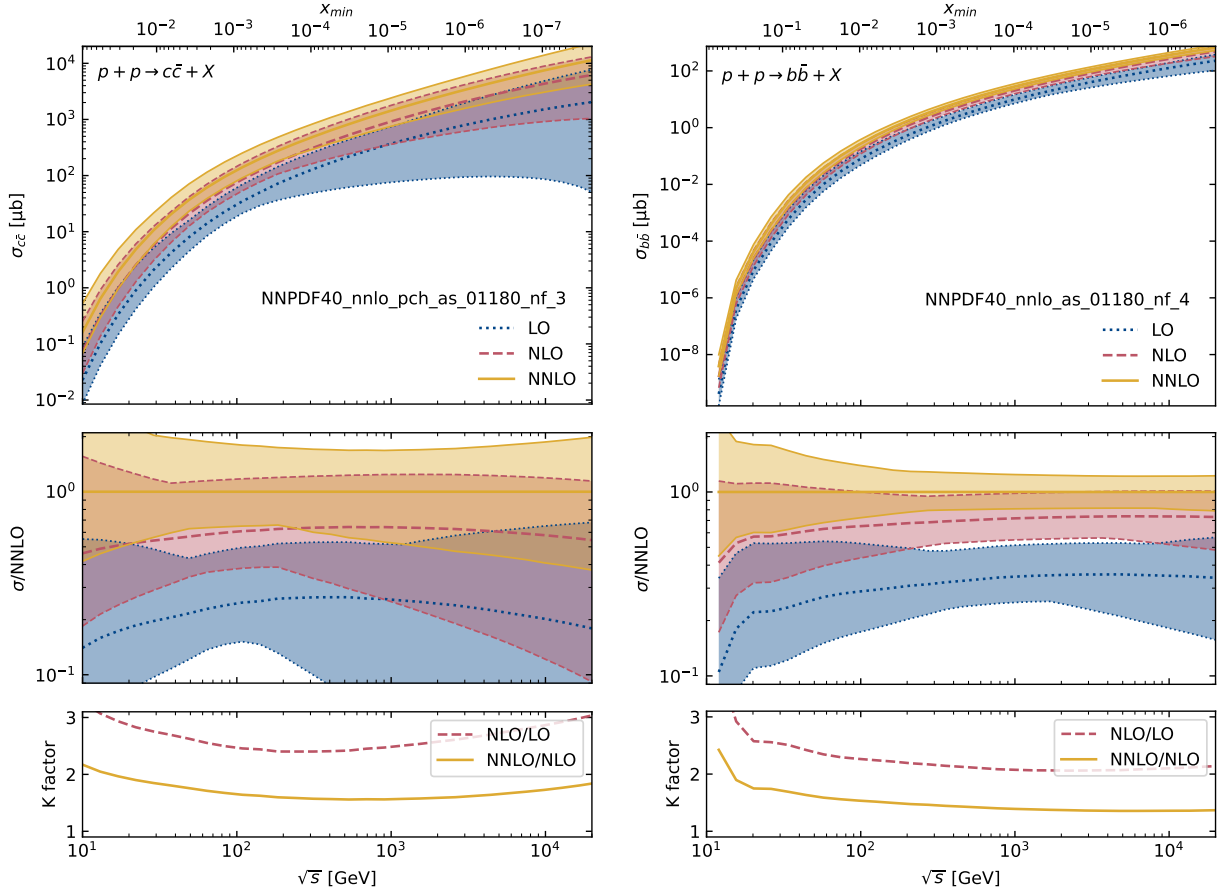


FIG. 4. Inclusive cross sections for charm (left) and bottom (right) production in p-p collisions as a function of the c.m. energy, over  $\sqrt{s} = 10$  GeV–20 TeV, computed at LO (blue), NLO (red), and NNLO (yellow) accuracy. All predictions are calculated with the NNLO PDFs. The upper panels display the absolute cross sections, with bands indicating the scale uncertainties. The middle panels show the relative scale uncertainty with respect to the central predictions, while the lower panels present the  $K$ -factors, i.e. the ratios of the cross sections to those at the preceding perturbative order. The  $x_{\min}$  values indicated in the upper  $x$  axis correspond to Eq. (5).

#### Breakdown of partonic channels

It is instructive to examine the relative contributions of different parton-parton collision combinations, indicated by the  $i, j$  indices in Eq. (4), to the total heavy-quark pair cross section. The relative fractions of  $gg$ ,  $gq$ , and  $q\bar{q}$  processes are plotted as a function of  $\sqrt{s}$  in Fig. 5 for the different perturbative orders. At LO accuracy only the gluon-gluon ( $gg$ ) and the quark-antiquark ( $q\bar{q}$ ) luminosities are possible, while at NLO also the gluon-quark ( $gq$ ) luminosity starts to contribute. The additional quark-quark luminosities ( $qq$ ,  $q\bar{q}'$  and  $q\bar{q}'$ ) that open up at NNLO and contribute to the

small remaining fraction of the total cross section, are not shown in the plot. As the individual partonic channels do not represent physical cross sections, there can be contributions that are negative or bigger than 100%. Figure 5 clearly displays the well-known fact that the heavy-quark cross sections are clearly dominated by the gluon-gluon channel for increasing  $\sqrt{s}$  values. Towards low  $\sqrt{s}$ , however, the  $q\bar{q}$  channel begins to compete and eventually exceeds the size of the gluon-gluon contribution when approaching the threshold production. This can be explained by the increasingly important role of the valence quarks towards low values of  $\sqrt{s}$ , which probe PDFs at higher  $x$  as can be seen from Eq. (5).

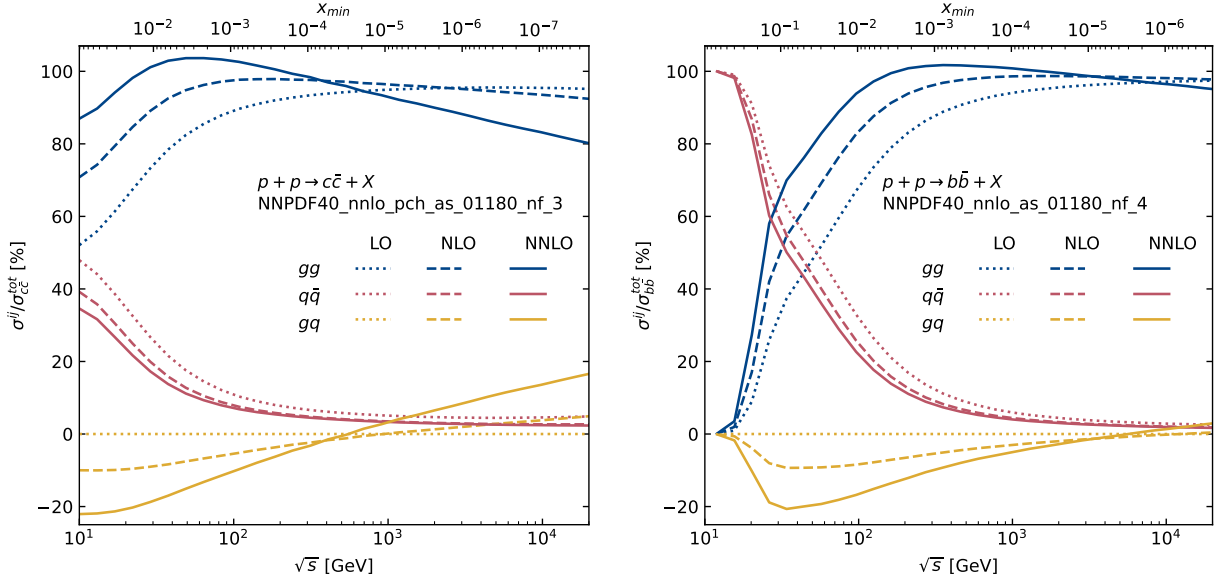


FIG. 5. Breakdown of the relative contribution of different parton-parton luminosities to the total charm (left) and bottom (right) cross section in p-p collisions as a function of c.m. energy, over  $\sqrt{s} = 10$  GeV–20 TeV: gluon-gluon (blue), quark-antiquark (red), and gluon-quark (yellow), at LO (dotted), NLO (dashed), and NNLO (solid) accuracy. The additional quark-quark luminosities that open up at NNLO are not plotted, as they provide only a minor contribution. The  $x_{\min}$  values indicated in the upper  $x$  axis correspond to Eq. (5).

### Heavy-quark mass dependence and uncertainties

In Fig. 6, we investigate the dependence of the inclusive NNLO  $Q\bar{Q}$  cross sections on the value of the heavy-quark mass  $m_Q$ . The charm mass is varied over the range  $m_c = 1.35$ – $1.65$  GeV around the default choice of  $m_c^0 = 1.51$  GeV, and the bottom mass in the range  $m_b = 4.5$ – $5.5$  GeV around the default choice of  $m_b^0 = 4.92$  GeV. Such variations (shown in the figure as error bands around the central curves) represent relative uncertainties of about  $\pm 10\%$  in the charm and bottom masses. The variations are performed in the coefficient functions, but not also in the PDFs because only MSHT20 provides PDF sets for  $N_f = 3, 4$  with  $m_Q$  variants. We fix the factorization scale and the renormalization scale to twice the default mass value  $\mu_F = \mu_R = 2m_Q^0$ , and vary only the value of the heavy quark mass in the hard matrix elements  $\hat{\sigma}$  and the associated phase-space, i.e., effectively, in Eq. (5). The default PDF sets from NNPDF4.0 are used, which do not provide alternative fits for varying  $m_Q$  values, thus neglecting any correlations between quark masses and PDFs [191]. We have checked with the dedicated MSHT20 PDF sets for different  $m_Q$  values, that the impact on the cross section of exactly matching  $m_Q$  in the matrix elements and PDFs is small. The left plot of Fig. 6 indicates that the  $m_c$  choice propagates as a maximum factor of two uncertainty in  $\sigma(c\bar{c})$  at  $\sqrt{s} \approx 10$  GeV, decreasing to a  $\pm(10$ – $20)\%$  uncertainty for  $\sqrt{s} \gtrsim 10$  TeV. Namely, the uncertainty in the  $c\bar{c}$  cross sections associated with the charm quark mass appears subleading with respect to the scale variation uncertainty (Fig. 4, left). On the other hand, for  $b\bar{b}$  production (Fig. 6, right) the bottom-quark mass variations propagate as a relative uncertainty in the cross sections that is somewhat larger than for the  $c\bar{c}$  case, and now dominates over the corresponding theoretical scale uncertainties (Fig. 4 right). This can be seen in particularly near the threshold production region, i.e. for  $\sqrt{s} \rightarrow 2m_b$ , where the

associated restriction on the available phase-space due to modifying the  $m_b$  value has a stronger impact on the pair production cross sections.

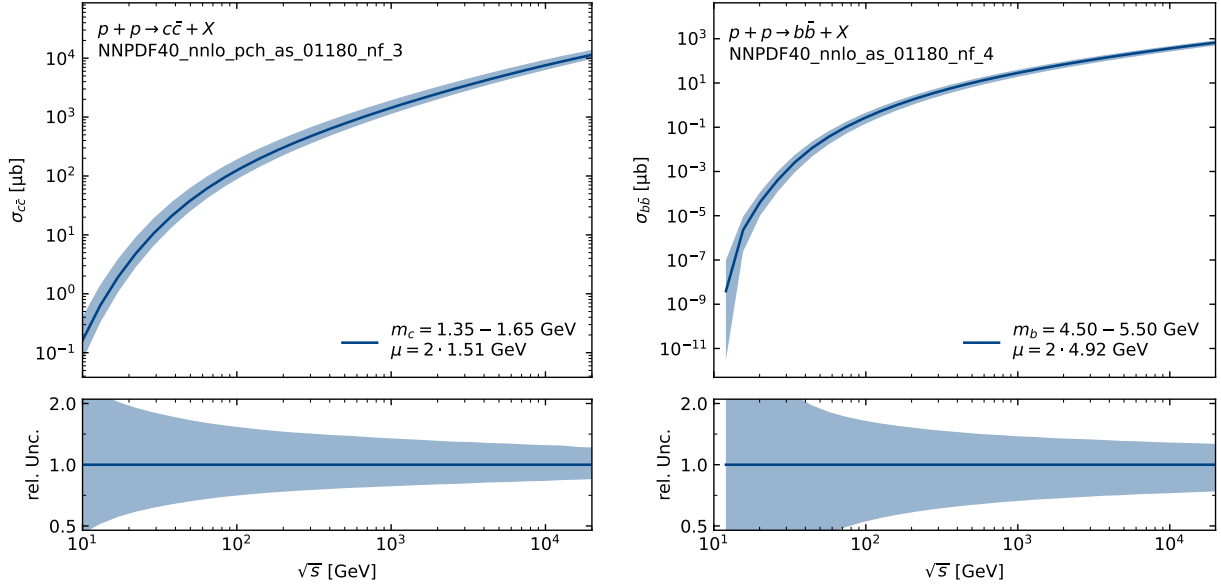


FIG. 6. Inclusive charm (left) and bottom (right) NNLO production cross sections as a function of collision energy, over  $\sqrt{s} = 10$  GeV–20 TeV, with the bands depicting the uncertainty associated with the heavy-quark mass value ( $m_Q$ ) used in the calculations. The charm quark mass is varied over  $m_c = 1.35$ – $1.65$  GeV around the default choice of  $m_c^0 = 1.51$  GeV. The bottom quark mass is varied over  $m_b = 4.5$ – $5.5$  GeV around the default choice of  $m_b^0 = 4.92$  GeV. All scales are fixed to twice the default mass value  $\mu_F = \mu_R = 2m_Q^0$ . The upper panels indicate the total cross section, while the lower panels indicate the relative uncertainty with respect to the default mass value.

### PDF dependence and uncertainties

Figure 7 shows the PDF dependence of the NNLO cross sections for charm (left) and bottom (right) production as a function of  $\sqrt{s}$ , as obtained using three different PDF sets: NNPDF4.0 (orange), MSHT20 (purple), and CT18 (blue), with their associated PDF uncertainty bands. For the predictions based on the CT18 PDFs, we use the central values of the fixed-flavour variant CT18NNLO\_NF3 and CT18NNLO\_NF4 PDFs for charm and bottom, respectively, but the relative PDF error estimates are obtained from the 58 eigenvectors of the default (variable flavour) CT18NNLO set. In general, NNPDF4.0 predicts the lowest cross sections below  $\sqrt{s} \approx 2$  (10) TeV for charm (bottom), whereas CT18 predicts larger values for all collision energies, and MSHT20 falls in between the other two PDFs except above  $\sqrt{s} \approx 2$  (10) TeV where they appear to drop significantly. First of all, and beyond PDF differences discussed in detail below, a first major source of the spread between CT18, NNPDF4.0, and MSHT20 seen in Fig. 7 can be attributed to the values of the heavy-quark masses adopted by each PDF set (Table III), to which the theoretical predictions exhibit strong sensitivity, as illustrated in Fig. 6. The pronounced decline of the MSHT20 PDF predictions at high  $\sqrt{s}$  reflects the limitations associated with the very low momentum fractions probed at LHC energies, which, according to Eq. (5), can reach values below  $x = 10^{-7}$  for either charm or bottom production. The fast decreasing and even negative cross sections for rising  $\sqrt{s}$  values occur simply because the MSHT20 PDF interpolation tables are not provided to as small momentum fractions as needed, and the calculation becomes sensitive to the technical extrapolation approach implemented in the LHAPDF interface [192]. Indeed, the interpolation tables for this PDF are only provided down to  $x_{\text{gridmin}} = 10^{-6}$  (indicated by the leftmost dashed vertical lines in Fig. 7) and since certain error set members exhibit a negative slope in this low- $x$  regime, such a trend is exacerbated by the LHAPDF interface (which extrapolates the latest PDF points with a simple polynomial function) leading to vanishing predictions. As a result, the theoretical  $\sigma(c\bar{c})$  cross sections obtained with MSHT20 have no meaningful physical interpretation above  $\sqrt{s} \approx 3$  TeV, as also reflected by the rapidly increasing uncertainty band, whose magnitude is not physically informative.

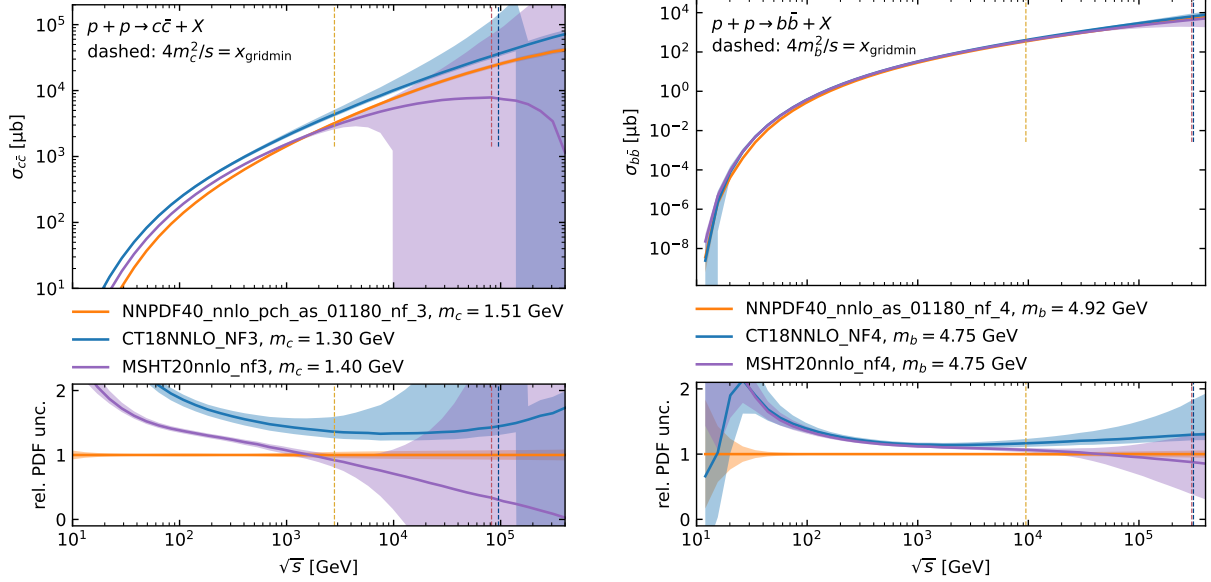


FIG. 7. Total charm (left) and bottom (right) cross section at NNLO accuracy in p-p collisions as a function of c.m. energy, over  $\sqrt{s} = 10$  GeV–400 TeV, predicted with different PDF sets: NNPDF4.0 (orange), MSHT20 (purple), and CT18 (blue), with bands indicating their corresponding PDF uncertainties. The upper panels show the total cross section, while the lower panels indicate their ratio to the NNPDF4.0 prediction. The vertical dashed lines indicate their associated  $x_{\text{gridmin}}$  values of the LHAPDF interpolation grids (Table III).

Compared to MSHT20, the interpolation tables of CT18 and NNPDF extend to smaller values, down to  $x_{\text{gridmin}} = 10^{-9}$  (indicated by the respective dashed vertical lines in Fig. 7). Even so, the NNLO  $\sigma(c\bar{c})$  predictions for those PDF sets become increasingly sensitive to the assumptions made about the behaviour of the parton densities in a region not directly constrained by the data. The datasets used to constrain PDFs in the small- $x$  region in modern global fits typically include DIS and gauge boson production at colliders, but neither provides direct constraints below  $x \approx 10^{-5}$ . Instead, PDF groups often impose a small- $x$  power-law behaviour of the form  $f \propto x^\alpha$ , based on Regge-theory arguments [193, 194], constrained only by the overall momentum sum rule. The question on how to approach this limit and what the exact scaling is, or at which scale it holds, remain open questions [190, 195, 196]. In the case of bottom production, the higher factorization scale mitigates the issue, as the PDF behaviour at small  $x$  is quickly governed by DGLAP evolution effects [197], thereby reducing the dependence on the assumptions imposed on the PDFs at the fitting scale, usually taken near the charm mass threshold.

Whereas for PDFs with a fixed polynomial parametrization, such as CT18 and MSHT20, the extrapolation behavior is exclusively driven by the assumed small- $x$  exponent, the behavior of NNPDF sets is more subtle. This can be seen clearly in the top panel of Fig. 8 where the gluon density of the NNPDF3.1 [198] (green) and NNPDF4.0 (orange) sets are compared, as probed in p-p  $\rightarrow c\bar{c} + X$  production as a function of  $\sqrt{s}$ . Differences are apparent starting at  $\sqrt{s} \approx 1$  TeV, with NNPDF3.1 (NNPDF4.0) rising (decreasing) rapidly with collision energy. Large differences between the two PDFs are not unexpected as both fits use significantly different datasets and, in particular, NNPDF4.0 includes a large amount of new LHC data that constrain better the gluon density. However, these LHC constraints do not extend to the small- $x$  regime where the large differences appear, and the most decisive difference appears to be the employed optimization algorithm: NNPDF3.1 relied on a genetic algorithm, whereas NNPDF4.0 uses a stochastic gradient descent method (see Ref. [17] for a detailed discussion). The former yields largely fluctuating PDFs in the extrapolation region, whilst the latter simply extrapolates the behaviour last seen in the data region as is expected from smooth functions. Neither of these assumptions have a solid first-principles foundation, nor have they been actually validated with experimental data, and thus should be taken with a grain of salt. The fact that the NNPDF4.0 gluon density seems to decrease rapidly with  $\sqrt{s}$  is not problematic per se, as the physical cross section, Eq. (4), involves a double multiplicative convolution. We can disentangle the double integral by defining the usual parton-parton luminosities  $\mathcal{L}_{ij}$  (see also Fig. 5) as the multiplicative convolution over two PDFs, i.e.

$$\mathcal{L}_{ij}(x, \mu_F^2) = x \left( f_i(\mu_F^2) \otimes f_j(\mu_F^2) \right) (x), \quad (7)$$

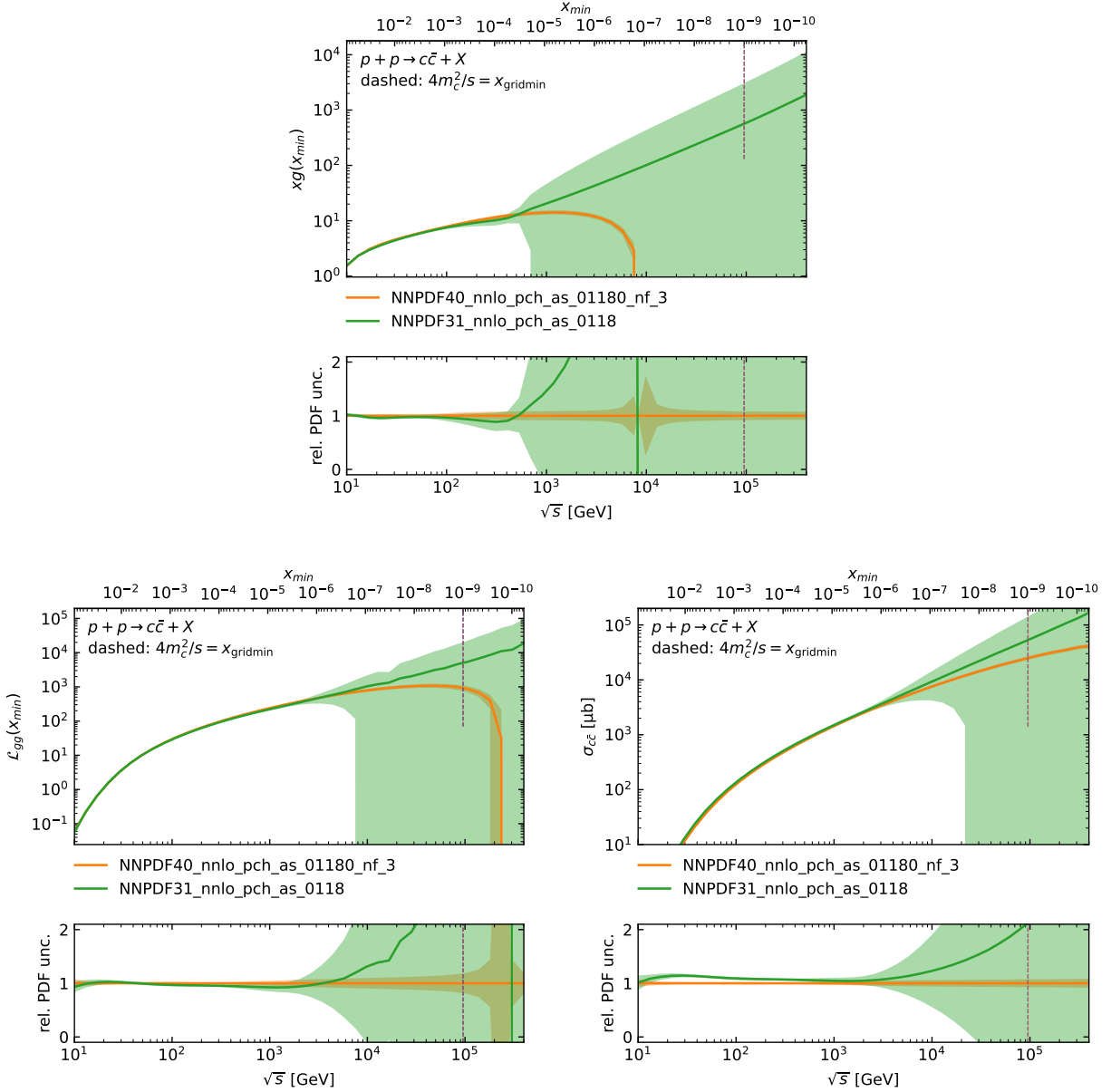


FIG. 8. Comparison of the NNPDF3.1 (green) and NNPDF4.0 (orange) NNLO parton densities in p-p collisions as a function of  $\sqrt{s}$  (lower  $x$  axis) and  $x_{\min}$  (upper  $x$  axis), for the following quantities: Gluon distribution  $xg(x, \mu_0^2)$  (upper), gluon-gluon luminosity  $\mathcal{L}_{gg}(x_{\min}, \mu_0^2)$ , Eq. (7), (lower left), and total charm cross section (lower right). The lower panels show the relative PDF uncertainties with respect to the central NNPDF4.0 results as a function of  $\sqrt{s}$ . The vertical dashed lines indicate the lower  $x_{\text{gridmin}} = 10^{-9}$  values of the LHAPDF interpolation tables.

such that the hadronic cross section is in turn just an ordinary multiplicative convolution of the parton-parton luminosities and the partonic cross sections, i.e.

$$\sigma^{p-p \rightarrow Q\bar{Q}+X}(\rho = 4m_Q^2/s, \mu_F^2, \mu_R^2) = \sum_{i,j} \left( \mathcal{L}_{ij}(\mu_F^2) \otimes \hat{\sigma}^{ij \rightarrow Q\bar{Q}+X}(\mu_F^2, \mu_R^2) \right) (\rho) \quad (8)$$

where the partonic cross sections are now folded over  $\hat{\rho} = 4m_Q^2/\hat{s}$ . As one can see from Fig. 8, a negative gluon distribution (upper panel) does not immediately imply a negative gluon-gluon luminosity (lower left) as those contributions to the integral need first to become dominant (which eventually occurs for  $\sqrt{s} \approx 200$  TeV in the NNPDF4.0 case).

Likewise, a negative gluon-gluon luminosity does not immediately lead to ill-behaved (negative) cross sections (lower right). As the differences between NNPDF3.1 and NNPDF4.0 in Fig. 8 clearly indicate, it should be useful to incorporate the  $\sigma(c\bar{c})$  measurements at the LHC to the global PDF fits, helping to obtain a data-driven constraint on the gluon density at very small momentum fractions  $x \lesssim 10^{-5}$ . While the theoretical uncertainties associated with scale and mass variations are sizable, they can be systematically propagated into the PDF fits by well-established procedures [199]. As a result, though these new constraints would not be very strong, they would nonetheless reduce the sensitivity of the small- $x$  PDFs to assumptions about their functional forms and to the details of the fitting methodology or optimization algorithms.

### *QCD coupling uncertainties*

In Fig. 9 we evaluate the impact of the strong coupling uncertainty,  $\alpha_s(m_Z) = 0.118 \pm 0.001$  [80], in the charm (left) and bottom (right) cross sections. In our calculations, the strong coupling is varied over  $\alpha_s(m_Z) = 0.117$ – $0.119$  in the hard matrix elements as well as, consistently, in the PDFs. For the latter, we use the standard (VFN scheme) NNPDF4.0 sets, which are provided with  $\alpha_s(m_Z)$  variations, to account for the corresponding change in the PDFs [200, 201]. For both  $c\bar{c}$  and  $b\bar{b}$  production the propagated  $\alpha_s$  uncertainty is small, of about 10% at the lowest collision energies, further decreasing with  $\sqrt{s}$  and becoming negligible at the LHC. The larger impact on the cross section with respect to the actual change in its value is due to the running of the strong coupling, which enhances differences at the small renormalization scales used here ( $\mu_R = 2m_Q$ ). We neglect any correlation that might appear by considering simultaneous variations of both the value of  $\alpha_s(m_Z)$  and the heavy quark mass  $m_Q$ , which, in principle, could appear through the gluon distribution. Note that apart from the purposes of this exercise, we always consider the correct FFN-scheme running of the strong coupling for the rest of the results presented in this work. In any case, the uncertainties associated with  $\alpha_s(m_Z)$  variations are clearly negligible compared with all other sources of theoretical uncertainties (scales, PDFs, quark masses) estimated in this work.

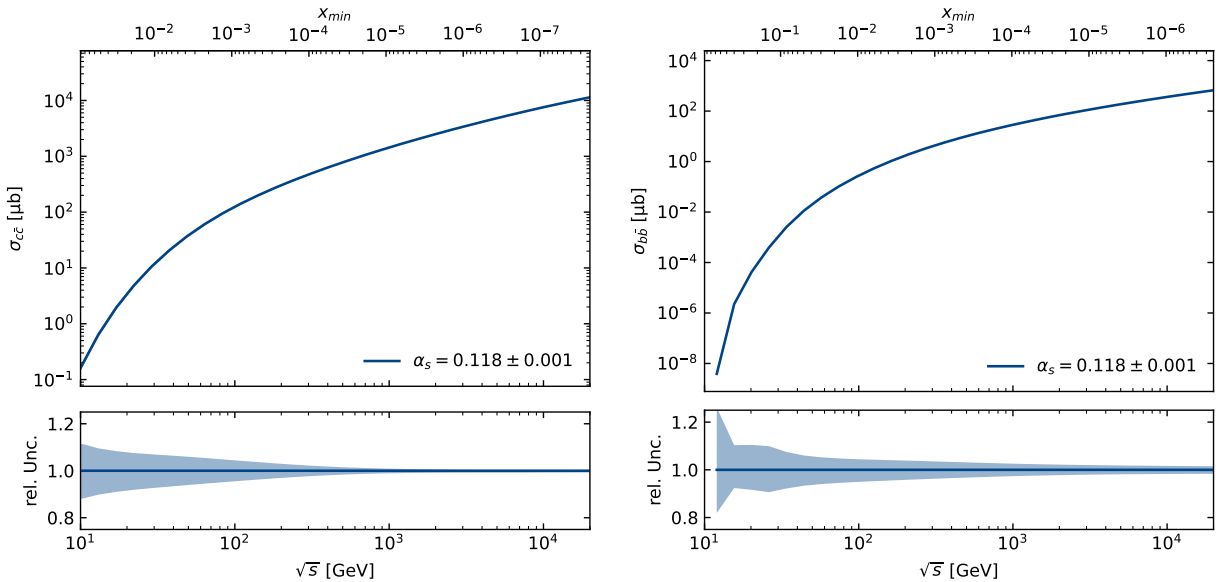


FIG. 9. Inclusive charm (left) and bottom (right) NNLO production cross sections as a function of collision energy, over  $\sqrt{s} = 10$  GeV–20 TeV, with the bands showing the uncertainty associated with variations of the strong coupling constant over  $\alpha_s(m_Z) = 0.117$ – $0.119$ . The lower panels show the relative  $\alpha_s(m_Z)$  uncertainties as a function of  $\sqrt{s}$ .

## B. VFN scheme: NLO calculations

As discussed in the previous section, the perturbative convergence of the FFN-scheme calculations appears rather slow, indicating that higher-order contributions are still presumably significant. A certain class of higher-order contributions can be accounted for in the GM-VFN scheme, which resums contributions that originate from collinear radiation and splitting from the initial- and final-state partons. For example, a collinear splitting of an initial-state gluon into a heavy quark-antiquark pair gives rise to a logarithmic term of the form  $\alpha_s \log(m_Q^2/m_T^2)$ , where  $m_T$  is the transverse mass of the heavy quark. Logarithmic terms of this sort can be resummed in GM-VFNS by introducing a DGLAP-evolving heavy-quark PDF. In the same spirit, a final-state gluon can split into a heavy quark-antiquark pair giving rise to a similar logarithmic term, which in this case can be resummed by introducing a scale-dependent gluon-to-heavy-quark FF. The numerical significance of the resummation, however, is not so easy to assess: it is not only the value of  $\alpha_s \log(m_Q/m_T)$  that matters, but e.g. the resummation always involves convolutions between partonic splitting functions and PDFs/FFs that obscure the simple power counting. In addition, and more importantly, the resummation suffers from scheme dependence, and this dependence is particularly severe at low values of transverse momentum which is precisely where most of the inclusive cross section accumulates. On the one hand, this leads to increased theoretical uncertainties and, in this sense, the FFN-scheme calculations for fully inclusive cross sections are typically considered more reliable. On the other hand, towards higher values of transverse momentum, the resummation becomes eventually necessary as the  $\alpha_s \log(m_Q^2/m_T^2)$  term grows. Whereas at low c.m. energies the transverse-momentum spectra for D- and B-mesons are very narrow, peaked at low  $p_T$ , they become increasingly wider in the range of LHC and FCC collision energies and the average transverse momentum grows larger (Fig. 10). As a result, the importance of the GM-VFNS approach should increase towards large c.m. energies.

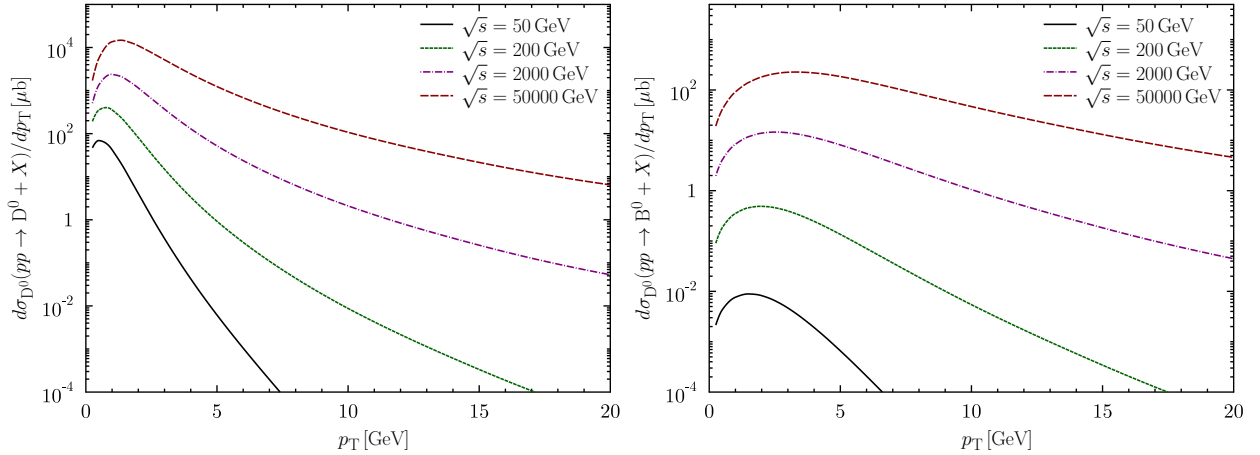


FIG. 10. Inclusive transverse momentum  $p_T$  spectra of  $D^0$  (left) and  $B^0$  (right) mesons produced in p-p collisions at various c.m. energies as computed in the SACOT- $m_T$  framework.

The general structure of a GM-VFNS  $p_T$ -differential cross section for the production of a heavy-flavoured hadron  $h_3$  in a collision between hadrons  $h_1$  and  $h_2$ ,

$$h_1(k_1) + h_2(k_2) \rightarrow h_3(p) + X, \quad (9)$$

is of the form (summed over incoming and outgoing partons  $i, j$ , and  $l$ ),

$$\begin{aligned} \frac{d^3\sigma^{h_1+h_2 \rightarrow h_3+X}}{d^3p/p^0} &= \sum_{i,j,l} \int_{z_{\min}}^1 \frac{dz}{z^2} \int_{x_{\min}}^1 dx_1 \int_{x_{\min}}^1 dx_2 f_i^{h_1}(x_1, \mu_F^2) f_j^{h_2}(x_2, \mu_F^2) D_{l \rightarrow h_3}(z, \mu_{FF}^2) \\ &\times J(\vec{k}, \vec{p}) \times \frac{d^3\hat{\sigma}^{i+j \rightarrow l+X}(x_1, x_2, m_Q, \sqrt{s}, \mu_R^2, \mu_F^2, \mu_{FF}^2)}{d^3k/k^0} - \text{subtraction terms}. \end{aligned} \quad (10)$$

Here  $p$  denotes the four-momentum of the outgoing hadron,  $k$  is the four-momentum of the parton that fragments into  $h_3$ , and  $D_{l \rightarrow h_3}(z, \mu_{FF}^2)$  denotes the corresponding parton-to-hadron fragmentation function at the fragmentation scale

$\mu_{\text{FF}}$ . The hadronic and partonic momenta are related by the fragmentation variable  $z$ , whose definition is not unique. A reasonable choice is

$$z \equiv \frac{p \cdot (k_1 - k_2)}{k \cdot (k_1 - k_2)}, \quad (11)$$

as argued in Ref. [33]. In this case the factor  $J(\vec{k}, \vec{p})$  in Eq. (10) is

$$J(\vec{k}, \vec{p}) = \sqrt{\frac{\vec{p}^2 + m_h^2}{\vec{p}^2} \frac{\vec{k}^2}{\vec{k}^2 + m_Q^2}}, \quad (12)$$

where  $m_h$  is the mass of the heavy-flavoured hadron. The partonic coefficient functions  $d^3\hat{\sigma}^{ij \rightarrow l+X}$  as well as the integration limits  $z^{\text{min}}$  and  $x_i^{\text{min}}$  are scheme-dependent. The GM-VFNS results presented here are obtained in the so-called SACOT- $m_T$  scheme whose underlying idea is to retain the implicit (“kinematic”) mass dependence also, e.g., in those partonic channels that do not explicitly involve a heavy quark [31]. The subtraction terms in Eq. (10) remove the double counting of logarithmic terms that have been resummed into the scale-dependent heavy-quark PDFs and FFs.

The integrated charm production cross section is calculated by evaluating the integrated cross section for  $D^0$  production using the Kneesch–Kniehl–Kramer–Schienbein [202] FFs and the NNPDF40\_nlo\_pch\_as\_01180 proton PDFs, and then dividing the result by the appropriate  $f(c \rightarrow h_c)$  branching fraction. Since the FFs were fitted to  $e^+e^-$  data, we use here  $f(c \rightarrow D^0) = 0.57$  consistently with the LEP data (Fig. 1, upper plots). For the integrated bottom production, we follow the same procedure but this time using the Kniehl–Kramer–Schienbein–Spiesberger FFs [29] for B mesons, the NNPDF40\_nlo\_as\_01180 proton PDFs, and  $f(c \rightarrow B^0) = 0.4$  (Fig. 3, upper left). The renormalization, factorization, and fragmentation scales have been chosen as

$$\mu_i = c_i \sqrt{p_T^2 + m_Q^2} \geq m_Q^2, \quad (13)$$

with the default  $c_i = 1$  value. The sensitivity of our result to missing higher-order corrections is quantified by varying  $c_i$  by a factor of two with the constraints  $1/2 \leq \mu_F/\mu_R \leq 2$ ,  $1/2 \leq \mu_{\text{FF}}/\mu_R \leq 2$ , and  $\mu_i \geq m_Q^2$ . This leads to 17 different combinations of scales, and the corresponding “scale uncertainty” is then defined to be the maximum/minimum envelope found by evaluating the cross sections with these 17 combinations. The scale uncertainty obtained in this way is rather “pessimistic” in a sense that the extreme scale variations are known [31, 33] to clearly over-/under-estimate the LHC measurements at low  $p_T$ . In other GM-VFNS variants, such as FONLL, the scale uncertainties are smaller due to choices made in defining the scheme which forces the low- $p_T$  regime to be more FFN-like.

### C. Corrections for p-p-equivalent cross sections

The MaunaKea and SACOT- $m_T$  cross section calculations are performed using the proton PDFs as expected for p-p collisions, but a fraction of the heavy-quark measurements have been performed in p- $\bar{p}$  (at CERN Sp $\bar{p}$ S and Fermilab Tevatron colliders) and p-A (in fixed target, RHIC, or LHC) collisions. The p-A results collected in our world-data systematics (Tables I and II) are already ‘p-p-equivalent’, namely they are quoted after normalizing the experimental cross section by the corresponding mass number  $A$ . If the actual collision system differs from p-p at a given  $\sqrt{s}$  value, a (small) correction factor needs to be further applied on the total predicted inclusive cross section to account for potential differences between proton and antiproton or nuclear PDFs, of the form

$$R_{p-X}(\sqrt{s}) = \frac{\sigma^{p-X}(\sqrt{s})}{\sigma^{p-p}(\sqrt{s})}, \quad \text{with } X = \bar{p}, A. \quad (14)$$

For the p- $\bar{p}$  case, this correction takes into account the charge conjugation transformation of the PDFs, whereas for p-A collisions we use the corresponding nuclear PDF (nPDF) from the NLO EPPS21 set [203]. The partonic cross-sections remain of course the same, but we restrict them to NLO to match the perturbative accuracy of EPPS21. We find very similar results when using NNLO partonic cross-section since  $R_{p-X}(\sqrt{s})$  is a ratio of cross sections. Moreover, it is worth recalling that the EPPS21 nPDFs are extracted from data by considering ratios of cross sections in the first place, which make them perturbatively more stable. The proton baseline in EPPS21 is CT18ANLO [19], which we thus use to evaluate Eq. (14).

Table IV lists the different correction factors applied to transform the calculated p-p predictions for charm and bottom cross section into the corresponding values for p- $\bar{p}$  or p-A collisions, accounting for the inclusive effect of

the antiproton or nuclear PDFs on the total yields. For each colliding system we list the proton and nuclear PDFs used to derive the value of the correction factor given by Eq. (14). The correction factor for p-Pb collision at the LHC is  $R_{p-X}(\sqrt{s} = 5 \text{ TeV}) = 0.77$  indicating a  $\sim 25\%$  gluon shadowing effect in the lead ion. At p- $\bar{p}$  colliders, the differences between proton and antiproton PDFs are negligible for heavy-quark production because this process is dominated by gluon-gluon (rather than valence quark) scatterings, so the factor is  $R_{p-X}(\sqrt{s}) = 1$  for them. The same is true for proton-light-ion collisions, such as p-He and p-Ne, for which nPDFs effects are expected to be negligible within the current theoretical uncertainties. For fixed-target results, we use the gold nPDF for both p-Au collisions, as well as for the carbon (C), titanium (Ti), and tungsten (W) targets. The correction factors for such collisions are  $R_{p-X}(\sqrt{s} \approx 40 \text{ GeV}) = 1.05$ , indicating a mild  $\sim 5\%$  gluon antishadowing in this kinematic regime. Of course, these correction factors come with their own (few percent) uncertainty, which is nonetheless negligible compared with other sources of theoretical uncertainty (scales, PDFs, and heavy-quark masses).

TABLE IV. Overall correction factors applied to the theoretical inclusive  $\sigma(p-p \rightarrow Q\bar{Q})$  cross sections for charm and bottom, to transform them into the corresponding pp-equivalent  $\sigma(p-\bar{p} \rightarrow Q\bar{Q})$  or  $\sigma(p-A \rightarrow Q\bar{Q})$  values, accounting for antiproton or nuclear PDF effects. For each colliding system we provide the PDFs used to derive the value of the correction factor through Eq. (14).

Measurement	PDFs used	Correction factor $R_{p-X}$
$\sigma(c\bar{c})$ cross sections:		
LHC (5 TeV pPb) [100, 110]	CT18ANLO (p), EPPS21 (Pb)	0.77
CDF (1.96 TeV p $\bar{p}$ ) [114]	CT18ANLO (p, $\bar{p}$ )	1.00
LHCb (86.6 GeV pHe) [122]	CT18ANLO (p, p)	1.00
LHCb (68.5 GeV pNe) [123]	CT18ANLO (p, p)	1.00
HERA-B (41.6 GeV pA, A=C,Ti,W) [124]	CT18ANLO (p), EPPS21 (Au)	1.05
E789 (38.8 GeV pAu) [127]	CT18ANLO (p), EPPS21 (Au)	1.05
$\sigma(b\bar{b})$ cross sections:		
UA1 (630 TeV p $\bar{p}$ ) [166]	CT18ANLO (p, $\bar{p}$ )	1.00
E771 (38.7 GeV pSi) [126, 178]	CT18ANLO (p), EPPS21 (Ca)	0.99
E789 (38.7 GeV pAu) [126, 179]	CT18ANLO (p), EPPS21 (Au)	0.98

#### IV. DATA VERSUS PQCD

We now turn to a comparison between the experimental data, compiled in Section II, and the theoretical predictions, including all sources of uncertainties, discussed in Section III. We remind the reader that the presented predictions here do not take a stand concerning the heavy-quark baryon-versus-meson enhancement observed at the LHC, i.e. they adopt a purely factorized leading-twist picture, while at least a fraction of the experimental data compared with the theory predictions is sensitive to the region where signals of HT effects have been observed.

In this section, we also present theoretical cross-section predictions extending up to the highest-energy hadronic collisions accessible at the FCC ( $\sqrt{s} \approx 100 \text{ TeV}$ ), as well as in cosmic-ray interactions at the GZK cutoff ( $\sqrt{s} \approx 400 \text{ TeV}$ ). Whereas the renormalization and factorization scales are formally unphysical, as their dependence would cancel in an all-orders prediction of the cross section, at fixed perturbative order a residual dependence remains due to the truncation of the perturbative series. For this reason, these scales must be chosen close to the characteristic hard scale of the process in order to avoid large logarithmic corrections and ensure good perturbative convergence. At very high collision energies, progressively smaller values of  $x$  are probed and, in particular for the gluon PDF, the dependence on the factorization scale becomes especially pronounced near  $\mu_F = m_c$ , leading to a substantial amplification of the associated scale uncertainties. To circumvent this issue, we explore an alternative prescription for the default theoretical scales,  $\mu_F$  and  $\mu_R$ , when evaluating the missing higher-order uncertainties of the MaunaKea NNLO predictions. Instead of fixing the default scales to a static value  $\mu_{\text{static}} = 2m_Q$ , corresponding to the production of a  $Q\bar{Q}$  pair at rest, and following the SACOT- $m_T$  results and discussion of Sec. III B, we include in quadrature a

kinematic dependence through the average  $p_T$  of the outgoing quarks as follows,

$$\mu_{\text{dyn.}} = c_i \sqrt{(2m_Q)^2 + \langle p_T \rangle^2} > 2m_Q, \text{ with } c_i = 1 \text{ for the default value and } c_i = \pm(2, 1/2) \text{ for the variations.} \quad (15)$$

At low  $\sqrt{s}$ , one has  $\mu_{\text{static}} \approx \mu_{\text{dyn.}}$ , whereas at high  $\sqrt{s}$  the dynamical scale better captures the increasing effective energy probed by the underlying partonic scatterings, as reflected in the progressively extended high- $p_T$  tail of heavy-quark meson spectra in Fig. 10. We have parametrized the approximately logarithmic dependence of  $\langle p_T \rangle$  on  $\sqrt{s}$ , as predicted from the differential SACOT- $m_T$  calculations, and combined it quadratically with  $(2m_Q)$ , which results in a modest  $\approx(20\text{--}30\%)$  enhancement of the  $\mu_F$  and  $\mu_R$  values at LHC and FCC/GZK-cutoff energies relative to the static scale choice. Using such a dynamic scale mitigates the large growth of the scale uncertainties that arises at very high c.m. energies when using the fixed rest-mass of the heavy-quark pair system as the default theoretical scale. This points once more to the slow convergence of the perturbative expansion, which might be cured by resummation as discussed earlier.

### A. $c\bar{c}$ cross sections

Figure 11 shows the selected set of experimental total charm production cross sections (gray entries in Table I) as a function of  $\sqrt{s}$  compared with the NNLO MaunaKea calculations obtained with the NNPDF4.0, CT18, and MSHT20 proton PDFs. Within the considered sources of theoretical uncertainties (scales, PDFs, and charm quark mass), all three sets of PDFs lead to predictions consistent with the data over the c.m. energies where the probed values of momentum fraction  $x$  remain within the region covered by the LHAPDF grid files (i.e., for the range of  $\sqrt{s}$  to the left of the vertical shaded light-gray areas indicating the extrapolated PDF regions in the plots). At the LHC energies, the data appear to lie in the upper edge of the scale-uncertainty band of the NNPDF4.0 predictions, while being better in line with the CT18 results. The main reason for this difference is the value of the charm-quark mass, which is lower in CT18 than in NNPDF4.0 and leads to higher cross sections across all values of  $\sqrt{s}$ . With the charm mass adopted by the NNPDF4.0 group an optimal agreement with the data would still require an  $N^3\text{LO}$  correction which increases the cross sections by a factor of two or so, i.e. of the same size as the NNLO correction, see Fig. 4. At first sight, the PDF uncertainty of NNPDF4.0 would appear to be too small to bridge the factor of two difference with respect to the data. However, the NNPDF4.0 uncertainty is likely unrealistically small (due to significant parametrization bias), see Fig. 8, as no data in the NNPDF4.0 global fit can directly constrain PDFs at the low values of  $x$  and factorization scales probed by the LHC charm data. The CT18 uncertainty is larger but seems to only allow variations towards higher cross sections. This is due to the CT18 fit constraints, which force the PDFs to remain positive at the parametrization scale  $m_c$ . This is a rather strict requirement because the parametrization scale can, in principle, be chosen entirely freely. In other words, while being more realistic than the NNPDF4.0 one, also the CT18 PDF uncertainty is subject to rather restrictive assumptions at the global fit stage. Regarding the MSHT20 predictions, the LHC kinematic region already lies beyond the validity range of its associated PDF grids (indicated by the vertical gray shaded areas in the plot). From a practical perspective, it would therefore be beneficial to extend the  $x$  grids coverage down to  $\sim 10^{-10}$  in future MSHT releases. Despite this problem, the central MSHT20 predictions are well in line with the measurements for collision energies below the LHC, whereas the central CT18 (NNPDF4.0) curve tends to somewhat overshoot (undershoot) the data. Also here, the hierarchy observed between the NNPDF4.0, CT18, and MSHT20 cross sections follows the different adopted charm-mass values of each PDF set.

Notwithstanding the sizable scale uncertainties in the theoretical calculations, we can conclude that  $\sigma(c\bar{c})$  measurements at the LHC can provide valuable input in future PDF global fits to constrain the gluon density at very small momentum fractions  $x \approx 10^{-6}$ , ensuring that its behaviour is increasingly driven by experimental data rather than by assumptions underlying the small- $x$  extrapolation. Once the theoretical uncertainties are accounted for in the fits, the constraints will not be very strong, but can better “anchor” the low- $x$  gluon density and e.g. exclude the clearly nonphysical cases with negative cross sections visible e.g. for NNPDF3.1 in Fig. 8. Although (well) beyond the range of validity of the current PDF sets, Fig. 11 shows theoretical cross sections up to a few hundred TeV where charm (and bottom) production represents a substantial fraction of the total inelastic cross section. These are of relevance for future-hadron collider (FCC-hh) perspectives [65, 66], and have an impact on muon and neutrino production in cosmic ray physics at ultrahigh energies, approaching the so-called “GZK cutoff” at  $\sqrt{s} \approx 400$  TeV [47, 67]. A reliable understanding of this ultrahigh-energy regime underscores the need for improved control over low- $x$  parton dynamics.

Figure 12 presents the identical data as Fig. 11, but now using the dynamical scale choice, Eq. (15), for the theoretical predictions. We observe a slightly reduced scale sensitivity at high collision energies while the central cross section remains practically the same for all the considered PDF sets. The impact of the dynamical scale choice is larger in

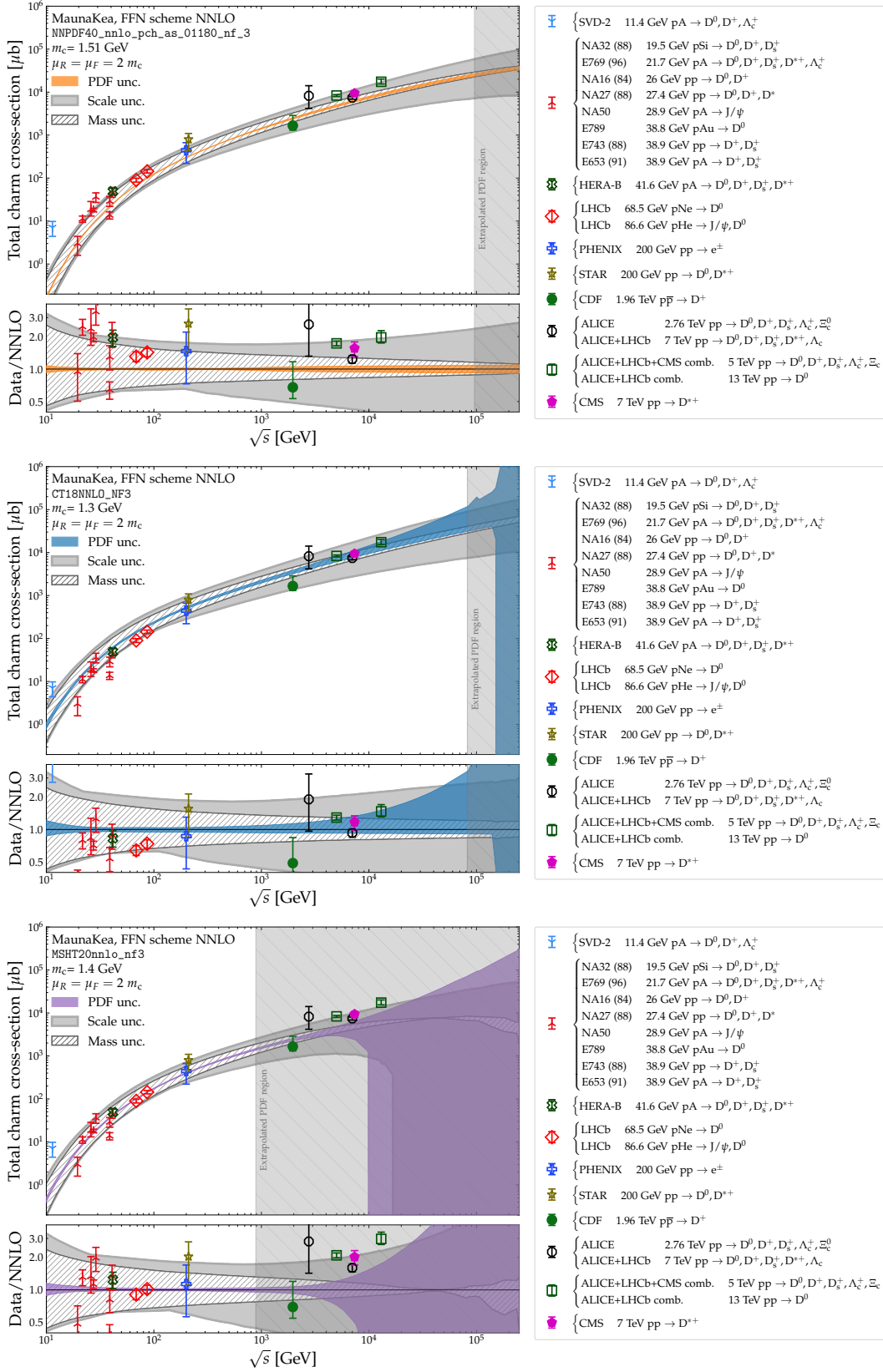


FIG. 11. Charm cross sections in p-p collisions as a function of c.m. energy, over  $\sqrt{s} = 10$  GeV–400 TeV: The experimental data (symbols, selected from Table I) are compared with theoretical MaunaKea NNLO (curves) for the NNPDF4.0 (upper), CT18 (middle), and MSHT20 (lower) PDFs. The PDF uncertainty (in orange, blue, and purple for NNPDF4.0, CT18, and MSHT20, respectively) (see also Fig. 7), the scale variation uncertainties (gray) (Fig. 4), and the charm-quark mass uncertainty (striped white and dark gray) (Fig. 6) are plotted as bands. The vertical shaded light-gray areas indicate the respective LHAPDF extrapolation regions (for which  $x_{\min} \leq x_{\text{gridmin}}$ , see text). The static scale  $\mu_F = \mu_R = 2m_Q$  is used. The lower panels show the data over NNLO ratios.

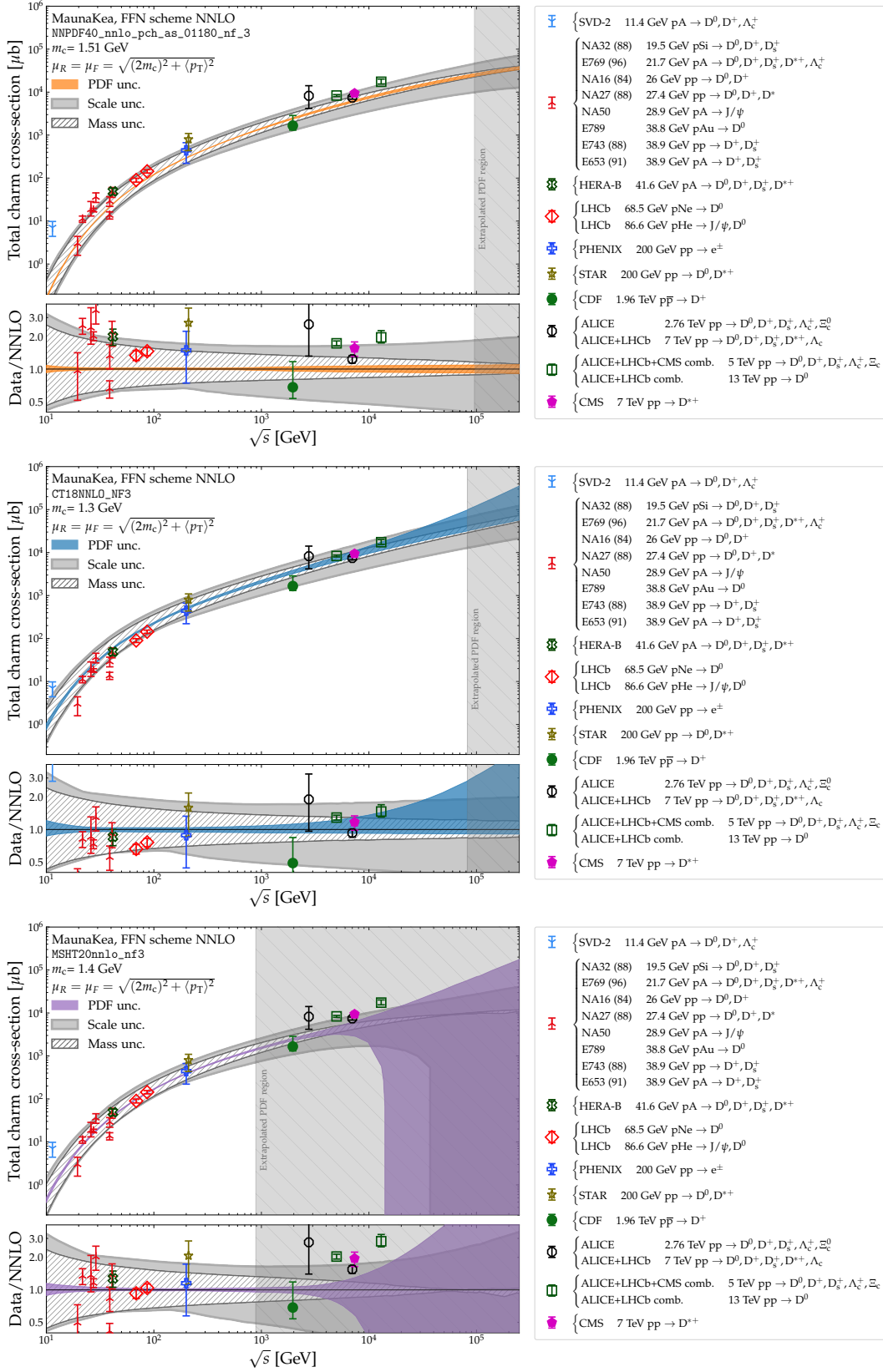


FIG. 12. The same as Fig. 11 but with the dynamic scale  $\mu_F = \mu_R = \mu_{\text{dyn.}}$ , Eq. (15).

the region not covered by the LHAPDF interpolation tables where for negative CT18 cross sections are avoided in the extrapolation region. Similarly for MSHT20, the slightly increased factorization and renormalization scales delay the unphysical extrapolation features which yields better behaved theory predictions. We stress again, that the extrapolation region is strongly driven by the last available points in the LHAPDF interpolation tables and, thus, is unreliable for physical interpretations.

Figure 13 presents a comparison between a somewhat larger selection of experimental charm cross section data than in Fig. 11 and the NLO SACOT- $m_T$  calculations obtained using the NNPDF4.0 PDFs. In addition, the FFNS MaunaKea predictions at NLO and NNLO are included to better judge their differences. Here, we do not target a systematic charting of theoretical uncertainties, but only display the scale uncertainties, which were found to be the dominant ones for the FFNS calculations (Fig. 4). The central SACOT- $m_T$  prediction describes the  $\sqrt{s}$  systematics surprisingly well, being generally a factor of two higher than the corresponding FFNS NNLO calculation with NNPDF4.0. At large  $\sqrt{s}$ , the SACOT- $m_T$  scale uncertainty clearly exceeds the FFNS one at NNLO, although it is actually comparable or even smaller than the FFNS NLO one, i.e. the resummation of mass logarithms appears to have some relevance reducing higher-order uncertainties at very high  $\sqrt{s}$ . At low  $\sqrt{s}$ , the FFNS and SACOT- $m_T$  scale-uncertainty envelopes are comparable. However, we note that in the SACOT- $m_T$  case, scale variations below  $m_c$  are not considered, which partially restricts the size of the downward uncertainty. While the NNLO scale uncertainties appear smaller, potentially suggesting that the FFNS prediction are more reliable than the SACOT- $m_T$  calculation, we remind the reader that the perturbative FFNS series does not exhibit clear signals of convergence and that the scale variations at lower orders do not perfectly capture the size of the higher-order corrections (Fig. 4). The SACOT- $m_T$  scale uncertainties are also expected to be somewhat overestimated, as comparisons with measurements [31] show that extreme scale variations fail to adequately describe the differential LHC D-meson cross section data. At  $\sqrt{s} \approx 100$  TeV, also the SACOT- $m_T$  calculation starts to integrate parton collisions below the NNPDF4.0  $x_{\text{gridmin}}$  value, although the underlying parton distributions are generally effectively probed at larger  $x$  values than in the FFNS calculations [31] and the predictions are, at the end, not as sensitive to the PDF-extrapolation region.

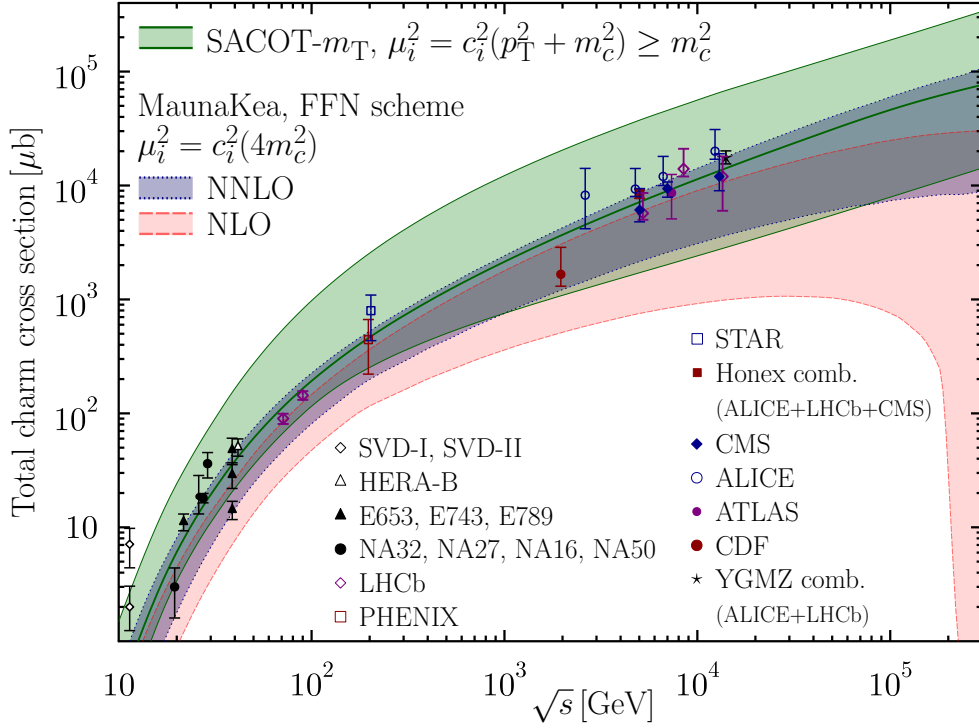


FIG. 13. Compilation of representative experimental total  $c\bar{c}$  cross sections as a function of  $\sqrt{s}$  (Honex and YGMZ indicate the data combinations of Refs. [113, 139], respectively) compared with GM-VFNS calculations within the SACOT- $m_T$  scheme, obtained using the corresponding NNPDF4.0 NLO PDF set. The corresponding MaunaKea NLO- and NNLO-accurate FFNS calculations are shown for comparison. The coloured bands denote the corresponding theoretical scale uncertainties.

## B. $b\bar{b}$ cross sections

Figure 14 displays a selected set of experimental data for total bottom production cross sections (gray entries in Table II) as a function of  $\sqrt{s}$  compared with the NNLO MaunaKea calculations obtained using the NNPDF4.0, CT18, and MSHT20 proton PDFs. First, in general, all the data can be described within the theoretical uncertainties and do not leave room for very large remaining N<sup>3</sup>LO QCD contributions. Compared to the charm case, the bottom-quark masses used in the three sets are relatively similar, and as a result all three PDF sets produce cross section predictions that are significantly more consistent with each other than observed for the former. The NNPDF4.0 set uses the largest  $m_b$  value and, correspondingly, predicts the lowest  $\sigma(b\bar{b})$  cross sections. At low  $\sqrt{s}$ , the NNLO calculations become highly sensitive to the bottom-quark mass because the mass variations modify the available phase space in the large- $x$  region where the PDFs are very steep functions of  $x$ . Unlike in the charm case, the effect of changing the bottom mass cannot be so easily compensated by the scale variations. As a result, improved measurements of bottom cross sections over  $\sqrt{s} \approx 10\text{--}100$  GeV would provide useful constraints on the bottom-quark pole mass. Due to the larger bottom compared to charm quark masses, the probed momentum fractions in the PDFs are clearly larger in  $b\bar{b}$  production, see Eq. (5), and the technical limitations of the LHAPDF grids are not as severe as for the  $\sigma(c\bar{c})$  calculations. Nevertheless, the highest  $\sqrt{s}$  probed at the LHC cannot be fully consistently computed with the MSHT20 grids, since low- $x$  PDF extrapolations become necessary above  $\sqrt{s} \approx 10$  TeV for this PDF set. This observation further motivates an extension of the minimum  $x$  coverage of the MSHT grids in future PDF releases. The impact of choosing the dynamical scale, Eq. (15), is negligible in the case of bottom production due to the larger mass and thus already higher scales. We list the corresponding values in Section B for completeness.

A comparison of experimental  $\sigma(b\bar{b})$  cross section measurements (including a few more data points than in Fig. 14) as a function of  $\sqrt{s}$  with the SACOT- $m_T$  calculations, obtained with the NNPDF4.0 NLO set, is shown in Fig. 15. Within the scale uncertainty bands, the calculation reproduces all data. However, the response of the theoretical cross sections to the scale variations is much larger than in the MaunaKea FFNS calculations, even at NLO. Also here, it is known that the most extreme scale variation used in the SACOT- $m_T$  approach do not provide a good agreement with the differential B-meson data from the LHC, and therefore the scale-uncertainty band is most likely unrealistically wide.

## V. SUMMARY

A comprehensive collection of existing measurements of inclusive charm and bottom cross sections in hadronic collisions over three orders-of-magnitude in collision energy  $\sqrt{s} \approx 10$  GeV–13 TeV has been presented, and compared with calculations at next-to-next-to-leading order (NNLO) accuracy in perturbative QCD as implemented in the new MaunaKea code, within the fixed flavour number (FFN) scheme. In addition, the data and NNLO calculations have been compared with the predictions obtained with the SACOT- $m_T$  general-mass variable-flavour-number scheme (GM-VFNS) at next-to-leading-order (NLO) accuracy. The theoretical MaunaKea cross sections are based on the matrix elements of the TOP++ code, developed for the calculation of top-quark pair cross sections, modified to be applicable for fixed-order calculations of charm- and bottom-quark pair production and interfaced with the PineAPPL fast interpolation grids. Theoretical predictions have been obtained for three different NNLO-accurate global-fit parton distribution functions (PDFs): NNPDF4.0, CT18, and MSHT20. The uncertainties associated with missing higher-order corrections, PDFs, heavy-quark masses, and the strong coupling have been quantified, and detailed data-versus-NNLO comparisons have been presented for each PDF set. In addition, heavy-quark cross sections predictions are provided up to the highest c.m. energies accessible at the CERN Future Circular Collider (FCC) and in ultrahigh-energy cosmic-ray interactions in the upper atmosphere,  $\sqrt{s} \approx 400$  TeV.

On the experimental side, a detailed discussion has been first provided about the determination of total charm and bottom cross sections from measurements of c- and b-hadrons (and/or their decay products), supplemented by extrapolations to heavy-quark-level cross sections based on parton-to-hadron fragmentation fractions. The determination of all relevant heavy-quark fragmentation fractions, and their dependence on the collision system where they have been measured ( $e^+e^-$ , DIS, LHC), have been thoroughly discussed. A collection of approximately 50 measurements for charm hadrons and 50 measurements for bottom hadrons has been compiled, specifying the fiducial phase space and the extrapolation factors used to derive the corresponding experimental  $\sigma(c\bar{c})$  and  $\sigma(b\bar{b})$  cross sections over  $\sqrt{s} \approx 10$  GeV–13 TeV. About 10 (20) of the existing fiducial measurements of charm (bottom) hadrons production cross sections have been converted into inclusive  $\sigma(c\bar{c})$  or  $\sigma(b\bar{b})$  values, enabling an extended comparison of results. The impact of using different parton-to-hadron fragmentation fractions has been considered, in particular in the context of the enhanced heavy-quark baryon-to-meson ratios observed at the LHC.

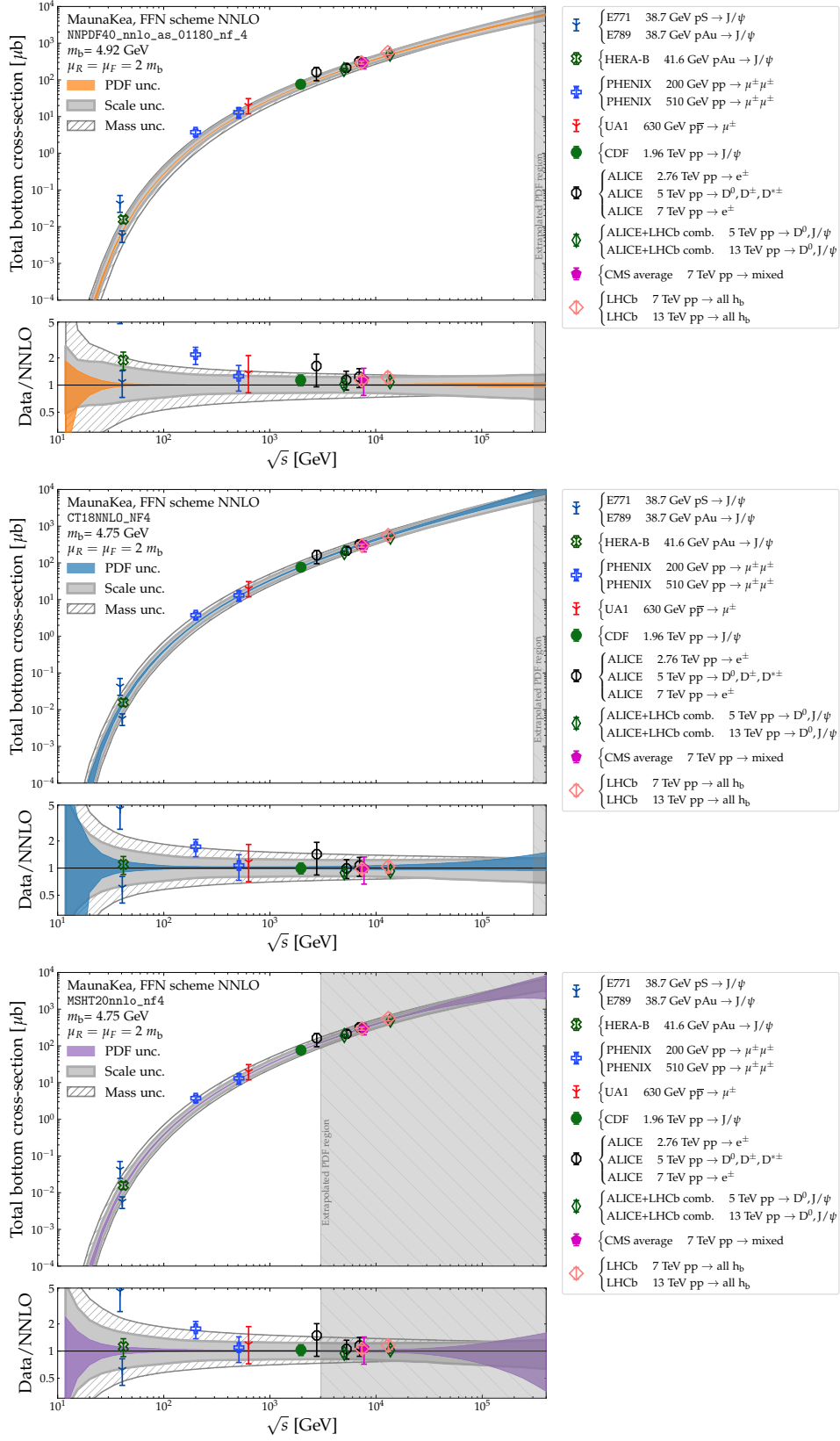


FIG. 14. Bottom cross sections in p-p collisions as a function of c.m. energy, over  $\sqrt{s} = 10$  GeV–400 TeV: The experimental data (symbols, selected from Table II) are compared with theoretical MaunaKea NNLO (curves) for the NNPDF4.0 (upper), CT18 (middle), and MSHT20 (lower) PDFs. The PDF uncertainty (in orange, blue, and purple for NNPDF4.0, CT18, and MSHT20, respectively) (see also Fig. 7), the scale variation uncertainties (gray) (Fig. 4), and the bottom-quark mass uncertainty (striped white and dark gray) (Fig. 6) are plotted as bands. The vertical shaded light-gray areas indicate the respective LHAPDF extrapolation regions (for which  $x_{\min} \leq x_{\text{gridmin}}$ , see text). The static scale  $\mu_F = \mu_R = 2m_Q$  is used. The lower panels show the data over NNLO ratios.

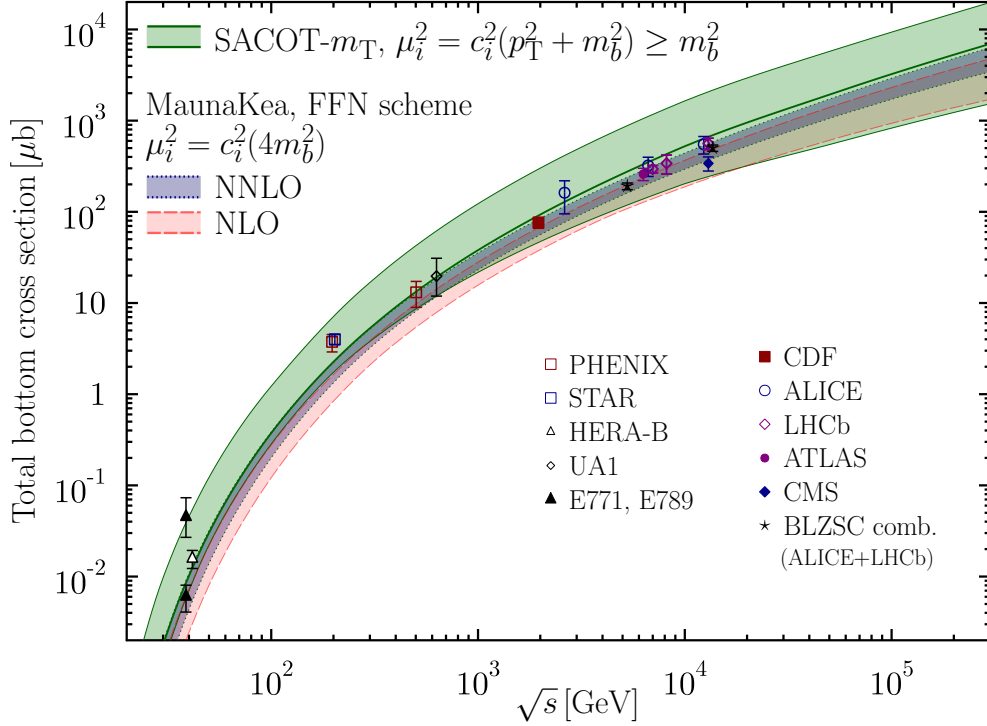


FIG. 15. Compilation of representative experimental total  $b\bar{b}$  cross sections as a function of  $\sqrt{s}$  (the BLZSC  $\sigma(b\bar{b})$  combination corresponds to that reported in Ref. [140]) compared with GM-VFNS calculations within the SACOT- $m_T$  scheme, obtained using the corresponding NNPDF4.0 NLO PDF set. The corresponding MaunaKea NNLO- and NLO-accuracy FFNS calculations are shown for comparison. The coloured bands denote the corresponding theoretical scale uncertainties.

On the theory side, the computed  $K$ -factors, defined as  $K = \sigma(N^{n+1}LO)/\sigma(N^nLO)$  (with  $n = 0, 1$ ) are found to decrease when going from NLO/LO to NNLO/NLO for both charm and bottom cross sections, indicating that the perturbative expansion is converging. However, we also observe that the NNLO cross sections for both heavy quarks are enhanced by up to a factor of two relative to the NLO predictions, i.e. the convergence of the perturbative series is slow. The theoretical uncertainties associated with the missing higher-order corrections have been estimated through scale variations, and found to be generally reduced when the perturbative accuracy of the calculation is increased. They still remain sizable, of the order of  $\pm 60\%$  ( $\pm 20\%$ ) for charm (bottom) production at NNLO, in the most favorable cases. We have also studied the sensitivity of the cross sections to the heavy-quark masses, by varying the values of  $m_c$  and  $m_b$  by  $\pm 10\%$  in the matrix elements from their nominal values defined in the PDF fits. For charm, we observe that  $m_c$  variations lead to cross-section uncertainties of about  $\pm 100\%$  ( $\pm 20\%$ ) at low (LHC) energies. For bottom-quark production,  $m_b$  variations remain the dominant source of uncertainty over the entire collision-energy range, leading to changes in the cross sections of about  $\pm 100\%$  ( $\pm 35\%$ ) at fixed-target (LHC) energies. Uncertainties associated with variations of  $\alpha_s(m_Z)$  within its current experimental precision are found to be subleading throughout the entire energy range, remaining (well) below 10% for both charm and bottom production.

As an alternative to the FFNS calculations, we also considered a specific GM-VFNS approach, SACOT- $m_T$ , which resums terms proportional to  $\log(m_T^2/m_Q^2)$  that are significant in the large- $p_T$  limit. These contributions should become more pronounced at higher collision energies due to increasingly flatter  $p_T$ -spectra, and therefore could potentially improve the convergence of the perturbative expansion. Although the missing higher-order corrections of this approach are still too large to draw a strong conclusion at NLO, evidence for reduced scale uncertainties at  $\sqrt{s} \approx 100$  TeV for charm is visible with respect to the fixed-order MaunaKea NLO result.

Detailed studies of the PDF dependence and propagated uncertainties of the heavy-quark cross sections have been presented. Except at the lowest collision energies in the bottom sector, heavy-quark pair production is dominated by gluon-gluon scattering, so the measured cross sections provide a particularly sensitive probe of the gluon PDF. In

the current global-PDF fits, the gluon density is fairly well constrained down to  $x \approx 10^{-5}$  where HERA data exist, but it is practically unconstrained at smaller parton fractional momenta. This small- $x$  region begins to contribute to heavy-quark cross section around  $\sqrt{s} \approx 1$  TeV in hadronic collisions and, accordingly, PDF uncertainties are found to increase in the multi-TeV regime. Technical issues appear for some of the employed PDFs when evaluated outside their nominal range of applicability in  $x$ . The LHAPDF grids of MSHT20 stop at  $x = 10^{-6}$ , beyond which the densities rely on uncontrolled LHAPDF extrapolations leading to unphysical behaviour of the central PDFs and inflation of their uncertainty bands. The NNPDF4.0 and CT18 PDFs interpolation grids extend down to  $x = 10^{-9}$ , which provides some stability for the obtained cross sections beyond LHC energies, but one should keep in mind that there are no actual data constraints available, and the PDF uncertainties might be restricted due to parametrization biases.

Accounting for all, admittedly sizable, uncertainties, we find good agreement between the NNLO calculations and experimental data over the full range of collision energies explored, though the level of accord depends on the PDF set used. The theory-data agreement is driven mainly by the choice of heavy-quark masses over  $\sqrt{s} \approx 10$  GeV–1 TeV, and by intrinsic low- $x$  PDF differences in the multi-TeV regime. For  $\sqrt{s} > 1$  TeV, the charm cross sections become sensitive to small- $x$  gluon distributions at low factorization scales where experimental constraints are absent, and in some cases depend on (arbitrary) LHAPDF extrapolations. In this context, three practical conclusions emerge. First, the existing  $\sigma(c\bar{c})$  measurements at the LHC can serve as input to future global PDF fits, providing constraints on the gluon density at very small momentum fractions  $x \approx 10^{-6}$ , and reducing reliance on assumptions inherent to small- $x$  extrapolations. Second, extending the  $x$ -grid coverage down to  $10^{-10}$  in future global-PDF releases would be advantageous, in particular in view of predictions for future hadron colliders. Third, in the case of  $b\bar{b}$  production at low  $\sqrt{s}$ , the NNLO calculations become highly sensitive to the bottom-quark mass, because it determines the available phase space, and thus precise measurements of  $\sigma(b\bar{b})$  cross sections above threshold, over  $\sqrt{s} \approx 10$ –100 GeV, would provide useful constraints on the bottom-quark pole mass.

Ultimately, high-precision charm and bottom cross sections will require improved experimental knowledge of heavy-flavour hadron production fractions over the largest possible phase space at the LHC, together with theoretical progress beyond NNLO fixed-order accuracy. Both developments are essential for a full understanding of heavy-quark production at future colliders such as the FCC-hh, as well as at the highest-energy hadronic collisions achieved in cosmic-ray interactions with the upper atmosphere. Further studies are therefore needed, and the present study provides a state-of-the-art baseline for such upcoming investigations.

*Acknowledgments* – Useful discussions with A. Verbytskyi on the experimental heavy-quark fragmentation fractions are acknowledged. A. Geiser’s contribution to collection of past experimental heavy-quark data is acknowledged. F. H., I. H., and H. P. have been supported by the Academy of Finland projects 331545, 358090 and 361179, and were funded as a part of the Center of Excellence in Quark Matter of the Academy of Finland, project 346326.

**Appendix A: NNLO charm p-p cross section tables**

TABLE V. Theoretical NNLO predictions for the inclusive  $c\bar{c}$  cross sections in p-p collisions over  $\sqrt{s} \approx 10$  GeV–400 TeV obtained with MaunaKea using the NNPDF40\_nnlo\_pch\_as\_01180\_nf\_3 PDFs. For each system, we list the central cross section,  $\sigma(c\bar{c})$ , followed by the percent (positive and negative) uncertainties from missing higher-order corrections ( $\Delta_{\text{scale}}^{\pm}$ ), parton densities ( $\Delta_{\text{PDF}}^{\pm}$ ), charm quark mass ( $\Delta_{m_c}^{\pm}$ ), and strong coupling constant ( $\Delta_{\alpha_s}^{\pm}$ ). The dotted line marks the lower  $x$  limit of validity of the PDF set by  $x_{\text{gridmin}}$  (cross sections for c.m. energies above this threshold rely on extrapolations provided by LHAPDF). The static scale  $\mu_F = \mu_R = 2m_Q$  is used as central value.

$\sqrt{s}$ [GeV]	$\sigma(c\bar{c})$ [ $\mu\text{b}$ ]	$\Delta_{\text{scale}}^+$ (%)	$\Delta_{\text{scale}}^-$ (%)	$\Delta_{\text{PDF}}^+$ (%)	$\Delta_{\text{PDF}}^-$ (%)	$\Delta_{m_c}^+$ (%)	$\Delta_{m_c}^-$ (%)	$\Delta_{\alpha_s}^+$ (%)	$\Delta_{\alpha_s}^-$ (%)
11.6	0.36	+200	-55	+5	-5	+135	-50	+10.5	-11
19.5	3.2	+135	-50	+3	-3	+95	-45	+7.5	-9
21.7	4.5	+125	-45	+2	-2	+90	-40	+7.5	-8
26	7.9	+110	-45	+2	-2	+85	-40	+7.5	-7.5
27.4	9.2	+105	-45	+2	-2	+80	-40	+7	-7.5
28.9	10.5	+105	-45	+2	-2	+80	-40	+7	-7.5
38.7	22.0	+95	-40	+2	-2	+70	-35	+6.5	-6.5
38.9	22.5	+95	-40	+2	-2	+70	-35	+6.5	-6.5
41.6	26.0	+95	-40	+2	-1	+70	-35	+6.5	-6.5
68.5	69.0	+85	-35	+2	-2	+60	-30	+5.5	-5.5
86.6	100	+80	-35	+2	-2	+55	-30	+4.5	-5
200	300	+75	-35	+2	-2	+45	-25	+3	-3
1960	2450	+70	-50	+4	-4	+30	-20	+1	-0.5
2760	3170	+75	-55	+5	-5	+30	-20	+0.5	-1
5000	4820	+80	-55	+5	-5	+25	-20	+0	-1
5020	4830	+80	-55	+5	-5	+25	-20	+0	-1
7000	6030	+80	-55	+6	-6	+25	-15	+0	-1
13000	8870	+90	-60	+6	-6	+25	-15	+0	-0.5
13600	9120	+90	-60	+6	-6	+25	-15	+0	-0.5
14000	9280	+90	-60	+6	-6	+25	-15	+0	-0.5
84000	23600	+130	-70	+7	-7	+15	-10	+0	-0
100000	25470	+135	-70	+7	-7	+15	-10	+0	-0
400000	41500	+190	-80	+9	-8	+10	-10	+0	-0

TABLE VI. Same as Table V, but using the  $\mu_F = \mu_R = \mu_{\text{dyn}}$  dynamic scale, Eq. (15), as central value.

$\sqrt{s}$ [GeV]	$\sigma(c\bar{c})$ [ $\mu\text{b}$ ]	$\Delta_{\text{scale}}^+$ (%)	$\Delta_{\text{scale}}^-$ (%)	$\Delta_{\text{PDF}}^+$ (%)	$\Delta_{\text{PDF}}^-$ (%)	$\Delta_{m_c}^+$ (%)	$\Delta_{m_c}^-$ (%)	$\Delta_{\alpha_s}^+$ (%)	$\Delta_{\alpha_s}^-$ (%)
11.6	0.36	+195	-55	+5	-5	+135	-50	+10	-11
19.5	3.1	+135	-50	+3	-3	+95	-45	+8	-8.5
21.7	4.4	+125	-45	+2	-2	+90	-40	+7.5	-8
26	7.7	+110	-45	+2	-2	+85	-40	+7	-7.5
27.4	9.0	+105	-45	+2	-2	+85	-40	+7	-7.5
28.9	10.4	+105	-45	+2	-2	+80	-40	+7	-7.5
38.7	21.6	+95	-40	+2	-2	+70	-35	+6.5	-6.5
38.9	21.8	+95	-40	+2	-2	+70	-35	+6.5	-6.5
41.6	25.4	+95	-40	+2	-2	+70	-35	+6	-6.5
68.5	67.2	+85	-35	+2	-2	+60	-30	+5	-5.5
86.6	98.5	+80	-35	+2	-2	+55	-30	+4.5	-5
200	300	+70	-35	+2	-2	+45	-25	+3	-3
1960	2450	+60	-45	+4	-4	+30	-20	+0.5	-1
2760	3170	+60	-50	+5	-5	+30	-20	+0.5	-1
5000	4820	+65	-50	+5	-5	+30	-20	+0	-1
5020	4830	+65	-50	+5	-5	+30	-20	+0	-1
7000	6020	+65	-50	+6	-6	+25	-20	+0	-1
13000	8870	+65	-55	+6	-6	+25	-15	+0	-0.5
13600	9110	+65	-55	+6	-6	+25	-15	+0	-0.5
14000	9270	+65	-55	+6	-6	+25	-15	+0	-0.5
84000	23580	+80	-60	+7	-7	+15	-10	+0	-1
100000	25500	+85	-60	+7	-7	+15	-10	+0	-1.5
400000	41600	+110	-65	+8	-8	+5	-10	+0.5	-2.5

TABLE VII. Theoretical NNLO predictions for the inclusive  $c\bar{c}$  cross sections in p-p collisions over  $\sqrt{s} \approx 10$  GeV–400 TeV obtained with MaunaKea using the CT18NNLO\_NF3 PDFs. For each system, we list the central cross section,  $\sigma(c\bar{c})$ , followed by the percent (positive and negative) uncertainties from missing higher-order corrections ( $\Delta_{\text{scale}}^{\pm}$ ), parton densities ( $\Delta_{\text{PDF}}^{\pm}$ ), charm quark mass ( $\Delta_{m_c}^{\pm}$ ), and strong coupling constant ( $\Delta_{\alpha_s}^{\pm}$ ). The dotted line marks the lower  $x$  limit of validity of the PDF set by  $x_{\text{gridmin}}$  (cross sections for c.m. energies above this threshold rely on extrapolations provided by LHAPDF). The static scale  $\mu_F = \mu_R = 2m_Q$  is used as central value.

$\sqrt{s}$ [GeV]	$\sigma(c\bar{c})$ [ $\mu\text{b}$ ]	$\Delta_{\text{scale}}^+$ (%)	$\Delta_{\text{scale}}^-$ (%)	$\Delta_{\text{PDF}}^+$ (%)	$\Delta_{\text{PDF}}^-$ (%)	$\Delta_{m_c}^+$ (%)	$\Delta_{m_c}^-$ (%)	$\Delta_{\alpha_s}^+$ (%)	$\Delta_{\alpha_s}^-$ (%)
11.6	1.73	+210	-55	+17	-11	+125	-55	+13.5	-11.5
19.5	10.5	+140	-50	+7	-6	+95	-45	+9.5	-9
21.7	14.1	+125	-45	+6	-5	+90	-45	+9	-8
26	22.5	+120	-45	+5	-5	+85	-45	+8	-7
27.4	25.5	+120	-45	+5	-5	+85	-45	+8	-7
28.9	29.0	+120	-45	+5	-5	+80	-40	+7.5	-7
38.7	53.5	+110	-40	+4	-5	+70	-40	+6	-6
38.9	54.0	+110	-40	+4	-5	+70	-40	+6	-6
41.6	61.5	+110	-40	+4	-5	+70	-40	+5.5	-6
68.5	140	+100	-40	+5	-5	+60	-35	+4.5	-4
86.6	195	+95	-40	+4	-5	+55	-35	+4	-3
200	510	+85	-45	+5	-6	+45	-30	+2	-2.5
1960	3400	+90	-60	+14	-7	+30	-25	+2	-1.5
2760	4330	+95	-60	+17	-7	+30	-20	+2	-1.5
5000	6470	+105	-65	+25	-8	+30	-20	+1.5	-2
5020	6480	+105	-65	+25	-8	+30	-20	+1.5	-2
7000	8030	+110	-65	+30	-8	+30	-20	+2	-1.5
13000	11850	+125	-70	+50	-8	+25	-20	+2	-2
13600	12180	+125	-70	+55	-8	+25	-20	+2	-1.5
14000	12400	+125	-70	+55	-8	+25	-20	+2	-1.5
84000	33780	+165	-80	+255	-9	+20	-15	+1.5	-1.5
100000	36900	+170	-80	+420	-9	+20	-15	+1.5	-1.5
400000	71850	+200	-85	+3835	-100	+20	-15	+1	-1

TABLE VIII. Same as Table VII, but using the  $\mu_F = \mu_R = \mu_{\text{dyn}}$  dynamic scale, Eq. (15), as central value.

$\sqrt{s}$ [GeV]	$\sigma(c\bar{c})$ [ $\mu\text{b}$ ]	$\Delta_{\text{scale}}^+$ (%)	$\Delta_{\text{scale}}^-$ (%)	$\Delta_{\text{PDF}}^+$ (%)	$\Delta_{\text{PDF}}^-$ (%)	$\Delta_{m_c}^+$ (%)	$\Delta_{m_c}^-$ (%)	$\Delta_{\alpha_s}^+$ (%)	$\Delta_{\alpha_s}^-$ (%)
11.6	1.70	+210	-55	+17	-11	+125	-55	+13.5	-11.5
19.5	10.2	+135	-50	+8	-6	+95	-45	+9.5	-8.5
21.7	13.7	+125	-45	+6	-5	+90	-45	+9	-8
26	21.8	+115	-45	+5	-5	+85	-45	+8	-7.5
27.4	24.7	+115	-45	+5	-5	+85	-45	+7.5	-7
28.9	28.0	+115	-45	+5	-5	+80	-40	+7.5	-7
38.7	51.9	+105	-40	+4	-5	+70	-40	+6	-6
38.9	52.4	+105	-40	+4	-5	+70	-40	+6	-6
41.6	59.6	+105	-40	+4	-5	+70	-40	+6	-5.5
68.5	137	+95	-35	+4	-5	+60	-35	+4	-4
86.6	190	+90	-35	+4	-5	+55	-35	+3.5	-3.5
200	500	+80	-40	+4	-6	+45	-30	+2	-2
1960	3400	+70	-55	+12	-7	+35	-25	+1.5	-1.5
2760	4330	+70	-55	+15	-7	+30	-20	+1.5	-1.5
5000	6470	+75	-55	+25	-8	+30	-20	+2	-1.5
5020	6480	+75	-55	+25	-8	+30	-20	+2	-1.5
7000	8030	+75	-55	+30	-8	+30	-20	+2	-2
13000	11880	+80	-60	+45	-8	+25	-20	+2	-1.5
13600	12190	+80	-60	+45	-8	+25	-20	+2	-1.5
14000	12400	+80	-60	+45	-8	+25	-20	+2	-2
84000	34550	+90	-65	+185	-9	+20	-15	+1.5	-1.5
100000	37650	+95	-65	+215	-9	+20	-15	+1.5	-1.5
400000	76650	+100	-65	+705	-10	+20	-15	+1.5	-1.5

TABLE IX. Theoretical NNLO predictions for the inclusive  $c\bar{c}$  cross sections in p-p collisions over  $\sqrt{s} \approx 10 \text{ GeV} - 400 \text{ TeV}$  obtained with MaunaKea using the MSHT20nnlo\_nf3 PDFs. For each system, we list the central cross section,  $\sigma(c\bar{c})$ , followed by the percent (positive and negative) uncertainties from missing higher-order corrections ( $\Delta_{\text{scale}}^{\pm}$ ), parton densities ( $\Delta_{\text{PDF}}^{\pm}$ ), charm quark mass ( $\Delta_{m_c}^{\pm}$ ), and strong coupling constant ( $\Delta_{\alpha_s}^{\pm}$ ). The dotted line marks the lower  $x$  limit of validity of the PDF set by  $x_{\text{gridmin}}$  (cross sections for c.m. energies above this threshold rely on extrapolations provided by LHAPDF). The static scale  $\mu_F = \mu_R = 2m_Q$  is used as central value.

$\sqrt{s}$ [GeV]	$\sigma(c\bar{c})$ [ $\mu\text{b}$ ]	$\Delta_{\text{scale}}^+$ (%)	$\Delta_{\text{scale}}^-$ (%)	$\Delta_{\text{PDF}}^+$ (%)	$\Delta_{\text{PDF}}^-$ (%)	$\Delta_{m_c}^+$ (%)	$\Delta_{m_c}^-$ (%)	$\Delta_{\alpha_s}^+$ (%)	$\Delta_{\alpha_s}^-$ (%)
11.6	0.90	+205	-55	+12	-9	+120	-55	+12	-10.5
19.5	6.20	+135	-50	+8	-4	+90	-45	+8	-8
21.7	8.50	+125	-45	+7	-4	+85	-45	+7.5	-7.5
26	14.0	+110	-45	+6	-4	+80	-40	+7	-6.5
27.4	16.0	+110	-45	+6	-4	+80	-40	+6.5	-6.5
28.9	18.5	+110	-45	+5	-3	+75	-40	+6.5	-6.5
38.7	35.5	+100	-40	+4	-3	+70	-40	+5.5	-5.5
38.9	35.7	+100	-40	+4	-3	+70	-40	+5.5	-5.5
41.6	41.0	+100	-40	+4	-3	+65	-40	+5	-5.5
68.5	99.5	+90	-35	+3	-3	+60	-35	+4	-3.5
86.6	140	+90	-35	+3	-3	+55	-35	+3.5	-3
200	390	+80	-40	+3	-3	+45	-30	+1.5	-2
1960	2390	+80	-65	+7	-8	+25	-20	+1	-1
.....									
2760	2925	+85	-65	+9	-12	+25	-20	+1	-1
5000	3990	+95	-70	+20	-28	+20	-15	+1	-1
5020	3995	+95	-75	+20	-29	+20	-15	+1	-1
7000	4650	+105	-75	+35	-48	+15	-15	+1	-1
13000	5875	+125	-90	+75	-100	+10	-10	+2	-2
13600	5965	+130	-90	+80	-100	+10	-10	+2	-2
14000	6020	+130	-90	+80	-100	+10	-10	+2	-2
84000	7610	+340	-100	+860	-100	+10	-15	+2	-2
100000	7425	+380	-100	+1130	-100	+10	-15	+2	-2
400000	1140	+4900	-100	+49725	-100	+270	-100	+2	-2

TABLE X. Same as Table IX, but using the  $\mu_F = \mu_R = \mu_{\text{dyn}}$  dynamic scale, Eq. (15), as central value.

$\sqrt{s}$ [GeV]	$\sigma(c\bar{c})$ [ $\mu\text{b}$ ]	$\Delta_{\text{scale}}^+$ (%)	$\Delta_{\text{scale}}^-$ (%)	$\Delta_{\text{PDF}}^+$ (%)	$\Delta_{\text{PDF}}^-$ (%)	$\Delta_{m_c}^+$ (%)	$\Delta_{m_c}^-$ (%)	$\Delta_{\alpha_s}^+$ (%)	$\Delta_{\alpha_s}^-$ (%)
11.6	0.88	+200	-55	+12	-9	+120	-55	+11.5	-10.5
19.5	6.05	+135	-50	+8	-4	+90	-45	+8	-8
21.7	8.32	+125	-45	+7	-4	+85	-45	+7.5	-7.5
26	13.7	+110	-45	+6	-4	+80	-40	+7	-6.5
27.4	15.6	+105	-45	+6	-3	+80	-40	+6.5	-6.5
28.9	17.8	+105	-45	+5	-3	+75	-40	+6.5	-6.5
38.7	34.4	+100	-40	+4	-3	+70	-40	+5.5	-5.5
38.9	34.7	+100	-40	+4	-3	+70	-40	+5.5	-5.5
41.6	39.8	+100	-40	+4	-3	+65	-40	+5	-5
68.5	96.9	+90	-35	+3	-3	+60	-35	+4	-3.5
86.6	138	+85	-35	+3	-3	+55	-35	+3	-3
200	385	+75	-40	+2	-3	+45	-30	+2	-2
1960	2420	+65	-55	+6	-8	+25	-20	+0.5	-0.5
2760	2980	+65	-60	+8	-11	+25	-20	+0	0
5000	4095	+70	-65	+18	-24	+20	-15	+0.5	-1
5020	4100	+70	-65	+18	-24	+20	-15	+0.5	-1
7000	4800	+70	-65	+30	-40	+20	-15	+0.5	-2
13000	6175	+80	-75	+60	-91	+15	-15	+1.5	-5.5
13600	6265	+80	-75	+65	-96	+15	-10	+1.5	-6
14000	6325	+80	-75	+65	-99	+15	-10	+2	-6
84000	9830	+150	-100	+495	-100	+0	-5	+7.5	-35
100000	10150	+160	-100	+585	-100	+0	-5	+8	-39
400000	11900	+300	-100	+2295	-100	+10	-15	+125	-92

**Appendix B: NNLO bottom p-p cross section tables**

TABLE XI. Theoretical NNLO predictions for the inclusive  $b\bar{b}$  cross sections in p-p collisions over  $\sqrt{s} \approx 10 \text{ GeV} - 400 \text{ TeV}$  obtained with MaunaKea using the NNPDF40\_nnlo\_as\_01180\_nf\_4 PDFs. For each system, we list the central cross section,  $\sigma(b\bar{b})$ , followed by the percent (positive and negative) uncertainties from missing higher-order corrections ( $\Delta_{\text{scale}}^{\pm}$ ), parton densities ( $\Delta_{\text{PDF}}^{\pm}$ ), bottom quark mass ( $\Delta_{m_b}^{\pm}$ ), and strong coupling constant ( $\Delta_{\alpha_s}^{\pm}$ ). The dotted line marks the lower  $x$  limit of validity of the PDF set by  $x_{\text{gridmin}}$  (cross sections for c.m. energies above this threshold rely on extrapolations provided by LHAPDF). The static scale  $\mu_F = \mu_R = 2m_Q$  is used as central value.

$\sqrt{s}$ [GeV]	$\sigma(b\bar{b})$ [ $\mu\text{b}$ ]	$\Delta_{\text{scale}}^+$ (%)	$\Delta_{\text{scale}}^-$ (%)	$\Delta_{\text{PDF}}^+$ (%)	$\Delta_{\text{PDF}}^-$ (%)	$\Delta_{m_b}^+$ (%)	$\Delta_{m_b}^-$ (%)	$\Delta_{\alpha_s}^+$ (%)	$\Delta_{\alpha_s}^-$ (%)
38.7	0.0056	+60	-35	+5	-5	+105	-60	+7	-7
41.6	0.0083	+60	-35	+4	-4	+100	-60	+5.5	-7.5
200	1.72	+30	-20	+1	-1	+50	-40	+4	-4
510	10.4	+25	-20	+1	-1	+45	-35	+3	-3
630	14.6	+25	-20	+1	-1	+40	-35	+3	-3
1960	67.0	+25	-20	+1	-1	+35	-30	+2.5	-2
2760	99.5	+25	-20	+1	-1	+35	-30	+2	-2
7000	260	+20	-20	+2	-2	+30	-30	+1.5	-2
13000	460	+20	-20	+2	-2	+30	-25	+1.5	-1.5
13600	480	+20	-20	+2	-2	+30	-25	+1.5	-2
14000	490	+20	-20	+2	-2	+30	-25	+1.5	-2
84000	2050	+25	-25	+4	-4	+25	-25	+1.5	-2
100000	2330	+25	-25	+4	-4	+25	-25	+1.5	-1.5
.....									
400000	5950	+30	-30	+6	-5	+20	-20	+1	-1

TABLE XII. Same as Table XI, but using the  $\mu_F = \mu_R = \mu_{\text{dyn}}$  dynamic scale, Eq. (15), as central value.

$\sqrt{s}$ [GeV]	$\sigma(\text{bb})[\mu\text{b}]$	$\Delta_{\text{scale}}^+$ (%)	$\Delta_{\text{scale}}^-$ (%)	$\Delta_{\text{PDF}}^+$ (%)	$\Delta_{\text{PDF}}^-$ (%)	$\Delta_{m_b}^+$ (%)	$\Delta_{m_b}^-$ (%)	$\Delta_{\alpha_s}^+$ (%)	$\Delta_{\alpha_s}^-$ (%)
38.7	0.0056	+60	-35	+5	-5	+105	-60	+6.5	-7
41.6	0.0083	+60	-35	+4	-4	+100	-60	+6	-7
200	1.7	+30	-20	+1	-1	+50	-40	+4	-4
510	10.4	+25	-20	+1	-1	+45	-35	+3	-3.5
630	14.5	+25	-20	+1	-1	+40	-35	+3	-3
1960	66.8	+25	-20	+1	-1	+35	-30	+2	-2
2760	98.9	+20	-20	+1	-1	+35	-30	+2	-2
7000	260	+20	-20	+2	-2	+30	-30	+1.5	-2
13000	460	+20	-20	+2	-2	+30	-25	+1.5	-1.5
13600	480	+20	-20	+2	-2	+30	-25	+1.5	-1.5
14000	490	+20	-20	+2	-2	+30	-25	+1.5	-1.5
84000	2050	+25	-25	+4	-4	+25	-25	+1	-1.5
100000	2340	+25	-25	+4	-4	+25	-25	+1	-1.5
400000	5950	+25	-30	+6	-5	+20	-20	+1	-1.5

TABLE XIII. Theoretical NNLO predictions for the inclusive  $\text{bb}$  cross sections in p-p collisions over  $\sqrt{s} \approx 10 \text{ GeV} - 400 \text{ TeV}$  obtained with MaunaKea using the CT18NNLO\_NF4 PDFs. For each system, we list the central cross section,  $\sigma(\text{bb})$ , followed by the percent (positive and negative) uncertainties from missing higher-order corrections ( $\Delta_{\text{scale}}^\pm$ ), parton densities ( $\Delta_{\text{PDF}}^\pm$ ), bottom quark mass ( $\Delta_{m_b}^\pm$ ), and strong coupling constant ( $\Delta_{\alpha_s}^\pm$ ). The dotted line marks the lower  $x$  limit of validity of the PDF set by  $x_{\text{gridmin}}$  (cross sections for c.m. energies above this threshold rely on extrapolations provided by LHAPDF). The static scale  $\mu_F = \mu_R = 2m_Q$  is used as central value.

$\sqrt{s}$ [GeV]	$\sigma(\text{bb}) [\mu\text{b}]$	$\Delta_{\text{scale}}^+$ (%)	$\Delta_{\text{scale}}^-$ (%)	$\Delta_{\text{PDF}}^+$ (%)	$\Delta_{\text{PDF}}^-$ (%)	$\Delta_{m_b}^+$ (%)	$\Delta_{m_b}^-$ (%)	$\Delta_{\alpha_s}^+$ (%)	$\Delta_{\alpha_s}^-$ (%)
38.7	0.010	+65	-35	+20	-12	+135	-55	+10.5	-9
41.6	0.014	+60	-35	+18	-11	+125	-55	+8.5	-9
200	2.17	+30	-20	+3	-3	+65	-40	+4.5	-3.5
510	12.3	+25	-20	+3	-3	+55	-35	+2.5	-2.5
630	17.0	+25	-20	+3	-3	+50	-30	+2.5	-2.5
1960	76.5	+25	-20	+3	-4	+45	-30	+2	-2
2760	115	+25	-20	+3	-4	+45	-30	+2	-2
7000	300	+25	-20	+5	-5	+40	-25	+2	-2
13000	540	+25	-20	+7	-5	+35	-25	+2	-2
13600	565	+25	-20	+7	-5	+35	-25	+2	-2
14000	580	+25	-20	+7	-5	+35	-25	+2	-2
84000	2550	+25	-25	+18	-6	+30	-20	+2	-2
100000	2910	+25	-25	+20	-6	+30	-20	+2	-2
400000	7760	+30	-30	+50	-7	+30	-20	+2	-2

TABLE XIV. Same as Table XIII, but using the  $\mu_F = \mu_R = \mu_{\text{dyn.}}$  dynamic scale, Eq. (15), as central value.

$\sqrt{s}$ [GeV]	$\sigma(\text{b}\bar{\text{b}})[\mu\text{b}]$	$\Delta_{\text{scale}}^+(\%)$	$\Delta_{\text{scale}}^-(\%)$	$\Delta_{\text{PDF}}^+(\%)$	$\Delta_{\text{PDF}}^-(\%)$	$\Delta_{m_b}^+(\%)$	$\Delta_{m_b}^-(\%)$	$\Delta_{\alpha_s}^+(\%)$	$\Delta_{\alpha_s}^-(\%)$
38.7	0.010	+65	-35	+20	-12	+135	-55	+10	-9
41.6	0.014	+60	-35	+18	-11	+125	-55	+9.5	-8.5
200	2.15	+30	-20	+3	-3	+65	-40	+4	-4
510	12.2	+25	-20	+3	-3	+55	-35	+2.5	-2.5
630	16.9	+25	-20	+3	-3	+50	-30	+2.5	-2.5
1960	76.1	+25	-20	+3	-4	+45	-30	+2	-2
2760	113	+25	-20	+3	-4	+45	-30	+2	-2
7000	300	+25	-20	+5	-5	+40	-25	+2	-2
13000	540	+25	-20	+7	-5	+35	-25	+2	-2
13600	560	+25	-20	+7	-5	+35	-25	+2	-2
14000	575	+25	-20	+7	-5	+35	-25	+2	-2
84000	2540	+25	-25	+18	-6	+30	-20	+2.5	-2.5
100000	2900	+25	-25	+20	-6	+30	-20	+2.5	-2.5
400000	7760	+25	-30	+45	-7	+30	-20	+2.5	-2.5

TABLE XV. Theoretical NNLO predictions for the inclusive  $\text{b}\bar{\text{b}}$  cross sections in p-p collisions over  $\sqrt{s} \approx 10 \text{ GeV} - 400 \text{ TeV}$  obtained with MaunaKea using the MSHT20nnlo.nf4 PDFs. For each system, we list the central cross section,  $\sigma(\text{b}\bar{\text{b}})$ , followed by the percent (positive and negative) uncertainties from missing higher-order corrections ( $\Delta_{\text{scale}}^\pm$ ), parton densities ( $\Delta_{\text{PDF}}^\pm$ ), bottom quark mass ( $\Delta_{m_b}^\pm$ ), and strong coupling constant ( $\Delta_{\alpha_s}^\pm$ ). The dotted line marks the lower  $x$  limit of validity of the PDF set by  $x_{\text{gridmin}}$  (cross sections for c.m. energies above this threshold rely on extrapolations provided by LHAPDF). The static scale  $\mu_F = \mu_R = 2m_Q$  is used as central value.

$\sqrt{s}$ [GeV]	$\sigma(\text{b}\bar{\text{b}}) [\mu\text{b}]$	$\Delta_{\text{scale}}^+(\%)$	$\Delta_{\text{scale}}^-(\%)$	$\Delta_{\text{PDF}}^+(\%)$	$\Delta_{\text{PDF}}^-(\%)$	$\Delta_{m_b}^+(\%)$	$\Delta_{m_b}^-(\%)$	$\Delta_{\alpha_s}^+(\%)$	$\Delta_{\alpha_s}^-(\%)$
38.7	0.0098	+65	-35	+11	-9	+135	-55	+8.5	-7.5
41.6	0.0140	+60	-35	+10	-8	+125	-55	+7	-8
200	2.10	+30	-20	+3	-2	+65	-40	+3.5	-3
510	12.0	+25	-20	+2	-2	+55	-35	+2.5	-2.5
630	16.6	+25	-20	+2	-2	+50	-30	+2	-2.5
1960	74	+25	-20	+2	-2	+45	-30	+2	-1.5
2760	110	+25	-20	+2	-2	+40	-30	+2	-1.5
7000	280	+20	-20	+2	-3	+40	-25	+1.5	-1.5
13000	485	+20	-20	+3	-4	+35	-25	+1.5	-1.5
13600	505	+25	-20	+3	-4	+35	-25	+1.5	-1.5
14000	520	+25	-20	+3	-4	+35	-25	+1.5	-1.5
84000	1975	+25	-30	+18	-25	+30	-20	+0	-1.5
100000	2215	+25	-30	+20	-28	+30	-20	+0	-1
400000	5085	+30	-35	+55	-64	+25	-15	+0	-1

TABLE XVI. Same as Table XV, but using the  $\mu_F = \mu_R = \mu_{\text{dyn}}$  dynamic scale, Eq. (15), as central value.

$\sqrt{s}$ [GeV]	$\sigma(\text{bb})[\mu\text{b}]$	$\Delta_{\text{scale}}^+(\%)$	$\Delta_{\text{scale}}^-(\%)$	$\Delta_{\text{PDF}}^+(\%)$	$\Delta_{\text{PDF}}^-(\%)$	$\Delta_{m_b}^+(\%)$	$\Delta_{m_b}^-(\%)$	$\Delta_{\alpha_s}^+(\%)$	$\Delta_{\alpha_s}^-(\%)$
38.7	0.0097	+65	-35	+11	-9	+135	-55	+8	-7.5
41.6	0.014	+60	-35	+10	-8	+125	-55	+7.5	-7.5
200	2.1	+30	-20	+3	-2	+65	-40	+3.5	-3.5
510	11.9	+25	-20	+2	-2	+55	-35	+2	-2.5
630	16.5	+25	-20	+2	-2	+50	-30	+2	-2.5
1960	73.5	+25	-20	+2	-2	+45	-30	+2	-1.5
2760	108	+25	-20	+2	-2	+40	-30	+2	-1.5
7000	278	+20	-20	+2	-3	+40	-25	+1.5	-2
.....									
13000	485	+20	-20	+3	-4	+35	-25	+1.5	-1.5
13600	505	+20	-20	+3	-4	+35	-25	+1.5	-1.5
14000	515	+20	-20	+3	-4	+35	-25	+1.5	-1.5
84000	1980	+25	-30	+18	-22	+30	-20	+0	-1.5
100000	2220	+25	-30	+20	-26	+30	-20	+0	-1
400000	5100	+30	-35	+55	-52	+25	-20	+0	-2.5

## REFERENCES

- [1] J. Huston, K. Rabbertz, and G. Zanderighi, “Quantum Chromodynamics,” [arXiv:2312.14015 \[hep-ph\]](#).
- [2] J. Andersen *et al.*, “Les Houches 2023: Physics at TeV Colliders: Standard Model Working Group Report,” in *Physics of the TeV Scale and Beyond the Standard Model: Intensifying the Quest for New Physics*. June, 2024. [arXiv:2406.00708 \[hep-ph\]](#).
- [3] A. Huss, J. Huston, S. Jones, M. Pellen, and R. Röntsch, “Les Houches 2023 – Physics at TeV Colliders: Report on the Standard Model Precision Wishlist,” [arXiv:2504.06689 \[hep-ph\]](#).
- [4] F. Caola, W. Chen, C. Duhr, X. Liu, B. Mistlberger, F. Petriello, G. Vita, and S. Weinzierl, “The Path forward to N<sup>3</sup>LO,” in *Snowmass 2021*. 3, 2022. [arXiv:2203.06730 \[hep-ph\]](#).
- [5] **Particle Data Group** Collaboration, S. Navas *et al.*, “Review of particle physics,” *Phys. Rev. D* **110** (2024) 030001.
- [6] J. C. Collins, D. E. Soper, and G. F. Sterman, “Factorization of Hard Processes in QCD,” *Adv. Ser. Direct. High Energy Phys.* **5** (1989) 1–91, [arXiv:hep-ph/0409313](#).
- [7] V. N. Gribov and L. N. Lipatov, “Deep inelastic e p scattering in perturbation theory,” *Sov. J. Nucl. Phys.* **15** (1972) 438–450.
- [8] Y. L. Dokshitzer, “Calculation of the Structure Functions for Deep Inelastic Scattering and e<sup>+</sup>e<sup>-</sup> Annihilation by Perturbation Theory in Quantum Chromodynamics.,” *Sov. Phys. JETP* **46** (1977) 641–653.
- [9] G. Altarelli and G. Parisi, “Asymptotic Freedom in Parton Language,” *Nucl. Phys. B* **126** (1977) 298–318.
- [10] M. Aliev, H. Lacker, U. Langenfeld, S. Moch, P. Uwer, and M. Wiedermann, “HATHOR: HAdronic Top and Heavy quarks crOss section calculator,” *Comput. Phys. Commun.* **182** (2011) 1034–1046, [arXiv:1007.1327 \[hep-ph\]](#).
- [11] M. Czakon and A. Mitov, “Top++: A program for the calculation of the top-pair cross-section at hadron colliders,” *Comput. Phys. Commun.* **185** (2014) 2930, [arXiv:1112.5675 \[hep-ph\]](#).
- [12] M. Czakon, P. Fiedler, and A. Mitov, “Total top-quark pair-production cross section at hadron colliders through  $\mathcal{O}(\alpha_s^4)$ ,” *Phys. Rev. Lett.* **110** (2013) 252004, [arXiv:1303.6254 \[hep-ph\]](#).
- [13] M. Czakon and A. Mitov, “NNLO corrections to top pair production at hadron colliders: the quark-gluon reaction,” *JHEP* **01** (2013) 080, [arXiv:1210.6832 \[hep-ph\]](#).
- [14] P. Bärnreuther, M. Czakon, and A. Mitov, “Percent Level Precision Physics at the Tevatron: First Genuine NNLO QCD Corrections to  $q\bar{q} \rightarrow t\bar{t} + X$ ,” *Phys. Rev. Lett.* **109** (2012) 132001, [arXiv:1204.5201 \[hep-ph\]](#).
- [15] **ATLAS** Collaboration, G. Aad *et al.*, “Climbing to the Top of the ATLAS 13 TeV data,” *Phys. Rept.* **1116** (2025) 127–183, [arXiv:2404.10674 \[hep-ex\]](#).
- [16] **CMS** Collaboration, A. Hayrapetyan *et al.*, “Stairway to discovery: A report on the CMS programme of cross section measurements from millibarns to femtobarns,” *Phys. Rept.* **1115** (2025) 3–115, [arXiv:2405.18661 \[hep-ex\]](#).
- [17] **NNPDF** Collaboration, R. D. Ball *et al.*, “The path to proton structure at 1% accuracy,” *Eur. Phys. J. C* **82** (2022) 428, [arXiv:2109.02653 \[hep-ph\]](#).
- [18] S. Bailey, T. Cridge, L. A. Harland-Lang, A. D. Martin, and R. S. Thorne, “Parton distributions from LHC, HERA, Tevatron and fixed target data: MSHT20 PDFs,” *Eur. Phys. J. C* **81** (2021) 341, [arXiv:2012.04684 \[hep-ph\]](#).
- [19] T.-J. Hou *et al.*, “New CTEQ global analysis of quantum chromodynamics with high-precision data from the LHC,” *Phys. Rev. D* **103** (2021) 014013, [arXiv:1912.10053 \[hep-ph\]](#).
- [20] S. Alekhin, M. V. Garzelli, S. O. Moch, and O. Zenaiev, “NNLO PDFs driven by top-quark data,” *Eur. Phys. J. C* **85** (2025) 162, [arXiv:2407.00545 \[hep-ph\]](#).
- [21] **CMS** Collaboration, A. Hayrapetyan *et al.*, “Review of top quark mass measurements in CMS,” *Phys. Rept.* **1115** (2025) 116–218, [arXiv:2403.01313 \[hep-ex\]](#).
- [22] T. Klijnsma, S. Bethke, G. Dissertori, and G. P. Salam, “Determination of the strong coupling constant  $\alpha_s(m_Z)$  from measurements of the total cross section for top-antitop quark production,” *Eur. Phys. J. C* **77** (2017) 778, [arXiv:1708.07495 \[hep-ph\]](#).
- [23] **CMS** Collaboration, A. M. Sirunyan *et al.*, “Measurement of the  $t\bar{t}$  production cross section, the top quark mass, and the strong coupling constant using dilepton events in pp collisions at  $\sqrt{s} = 13$  TeV,” *Eur. Phys. J. C* **79** (2019) 368, [arXiv:1812.10505 \[hep-ex\]](#).
- [24] D. d’Enterria *et al.*, “The strong coupling constant: state of the art and the decade ahead,” *J. Phys. G* **51** (2024) 090501, [arXiv:2203.08271 \[hep-ph\]](#).
- [25] M. L. Mangano, P. Nason, and G. Ridolfi, “Heavy quark correlations in hadron collisions at next-to-leading order,” *Nucl. Phys. B* **373** (1992) 295–345.
- [26] M. Cacciari, M. Greco, and P. Nason, “The  $p_T$  spectrum in heavy-flavour hadroproduction,” *JHEP* **05** (1998) 007, [arXiv:hep-ph/9803400](#).
- [27] B. A. Kniehl, G. Kramer, I. Schienbein, and H. Spiesberger, “Inclusive  $D^{*\pm}$  production in  $p\bar{p}$  collisions with massive charm quarks,” *Phys. Rev. D* **71** (2005) 014018, [arXiv:hep-ph/0410289](#).
- [28] B. A. Kniehl, G. Kramer, I. Schienbein, and H. Spiesberger, “Collinear subtractions in hadroproduction of heavy quarks,” *Eur. Phys. J. C* **41** (2005) 199–212, [arXiv:hep-ph/0502194](#).
- [29] B. A. Kniehl, G. Kramer, I. Schienbein, and H. Spiesberger, “Finite-mass effects on inclusive  $B$  meson hadroproduction,” *Phys. Rev. D* **77** (2008) 014011, [arXiv:0705.4392 \[hep-ph\]](#).
- [30] B. A. Kniehl, G. Kramer, I. Schienbein, and H. Spiesberger, “Inclusive B-Meson Production at the LHC in the GM-VFN Scheme,” *Phys. Rev. D* **84** (2011) 094026, [arXiv:1109.2472 \[hep-ph\]](#).

- [31] I. Helenius and H. Paukkunen, “Revisiting the D-meson hadroproduction in general-mass variable flavour number scheme,” *JHEP* **05** (2018) 196, [arXiv:1804.03557 \[hep-ph\]](#).
- [32] K. Xie, J. M. Campbell, and P. M. Nadolsky, “A general-mass scheme for prompt charm production at hadron colliders,” *SciPost Phys. Proc.* **8** (2022) 084, [arXiv:2108.03741 \[hep-ph\]](#).
- [33] I. Helenius and H. Paukkunen, “B-meson hadroproduction in the SACOT- $m_T$  scheme,” *JHEP* **07** (2023) 054, [arXiv:2303.17864 \[hep-ph\]](#).
- [34] M. Cacciari, S. Frixione, N. Houdeau, M. L. Mangano, P. Nason, and G. Ridolfi, “Theoretical predictions for charm and bottom production at the LHC,” *JHEP* **10** (2012) 137, [arXiv:1205.6344 \[hep-ph\]](#).
- [35] M. Cacciari, M. L. Mangano, and P. Nason, “Gluon PDF constraints from the ratio of forward heavy-quark production at the LHC at  $\sqrt{s} = 7$  and 13 TeV,” *Eur. Phys. J. C* **75** (2015) 610, [arXiv:1507.06197 \[hep-ph\]](#).
- [36] S. Frixione, P. Nason, and C. Oleari, “Matching NLO QCD computations with Parton Shower simulations: the POWHEG method,” *JHEP* **11** (2007) 070, [arXiv:0709.2092 \[hep-ph\]](#).
- [37] S. Alioli, P. Nason, C. Oleari, and E. Re, “A general framework for implementing NLO calculations in shower Monte Carlo programs: the POWHEG BOX,” *JHEP* **06** (2010) 043, [arXiv:1002.2581 \[hep-ph\]](#).
- [38] T. Sjostrand, S. Mrenna, and P. Z. Skands, “PYTHIA 6.4 Physics and Manual,” *JHEP* **05** (2006) 026, [arXiv:hep-ph/0603175](#).
- [39] C. Bierlich *et al.*, “A comprehensive guide to the physics and usage of PYTHIA 8.3,” *SciPost Phys. Codeb.* **2022** (2022) 8, [arXiv:2203.11601 \[hep-ph\]](#).
- [40] S. Catani, S. Devoto, M. Grazzini, S. Kallweit, and J. Mazzitelli, “Bottom-quark production at hadron colliders: fully differential predictions in NNLO QCD,” *JHEP* **03** (2021) 029, [arXiv:2010.11906 \[hep-ph\]](#).
- [41] M. L. Czakon, T. Generet, A. Mitov, and R. Poncelet, “B-hadron production in NNLO QCD: application to LHC  $t\bar{t}$  events with leptonic decays,” *JHEP* **10** (2021) 216, [arXiv:2102.08267 \[hep-ph\]](#).
- [42] J. Mazzitelli, A. Ratti, M. Wiesemann, and G. Zanderighi, “B-hadron production at the LHC from bottom-quark pair production at NNLO+PS,” *Phys. Lett. B* **843** (2023) 137991, [arXiv:2302.01645 \[hep-ph\]](#).
- [43] M. Czakon, T. Generet, A. Mitov, and R. Poncelet, “Open B-Hadron Production at Hadron Colliders in QCD at Next-to-Next-to-Leading-Order and Next-to-Next-to-Leading-Logarithmic Accuracy,” *Phys. Rev. Lett.* **135** (2025) 161903, [arXiv:2411.09684 \[hep-ph\]](#).
- [44] M. Grazzini, S. Kallweit, and M. Wiesemann, “Fully differential NNLO computations with MATRIX,” *Eur. Phys. J. C* **78** (2018) 537, [arXiv:1711.06631 \[hep-ph\]](#).
- [45] H.-S. Shao and G. Wang, “Analytic NNLO transverse-momentum-dependent soft function for heavy quark pair hadroproduction at threshold,” *JHEP* **10** (2025) 164, [arXiv:2506.23791 \[hep-ph\]](#).
- [46] D. d’Enterria and A. M. Snigirev, “Triple parton scatterings in high-energy proton-proton collisions,” *Phys. Rev. Lett.* **118** (2017) 122001, [arXiv:1612.05582 \[hep-ph\]](#).
- [47] D. d’Enterria and A. M. Snigirev, “Triple-parton scatterings in proton-nucleus collisions at high energies,” *Eur. Phys. J. C* **78** (2018) 359, [arXiv:1612.08112 \[hep-ph\]](#).
- [48] A. Accardi *et al.*, “A Critical Appraisal and Evaluation of Modern PDFs,” *Eur. Phys. J. C* **76** (2016) 471, [arXiv:1603.08906 \[hep-ph\]](#).
- [49] LHCb Collaboration, R. Aaij *et al.*, “Prompt charm production in pp collisions at  $\sqrt{s} = 7$  TeV,” *Nucl. Phys. B* **871** (2013) 1–20, [arXiv:1302.2864 \[hep-ex\]](#).
- [50] CMS Collaboration, A. M. Sirunyan *et al.*, “Production of  $\Lambda_c^+$  baryons in proton-proton and lead-lead collisions at  $\sqrt{s_{NN}} = 5.02$  TeV,” *Phys. Lett. B* **803** (2020) 135328, [arXiv:1906.03322 \[hep-ex\]](#).
- [51] ALICE Collaboration, S. Acharya *et al.*, “Charm-quark fragmentation fractions and production cross section at midrapidity in pp collisions at the LHC,” *Phys. Rev. D* **105** (2022) L011103, [arXiv:2105.06335 \[nucl-ex\]](#).
- [52] CMS Collaboration, A. Tumasyan *et al.*, “Study of charm hadronization with prompt  $\Lambda_c^+$  baryons in proton-proton and lead-lead collisions at  $\sqrt{s_{NN}} = 5.02$  TeV,” *JHEP* **01** (2024) 128, [arXiv:2307.11186 \[nucl-ex\]](#).
- [53] LHCb Collaboration, R. Aaij *et al.*, “Enhanced production of  $\Lambda_b^0$  baryons in high-multiplicity pp collisions at  $\sqrt{s} = 13$  TeV,” *Phys. Rev. Lett.* **132** (2024) 081901, [arXiv:2310.12278 \[hep-ex\]](#).
- [54] P. R. Sorensen and X. Dong, “Suppression of non-photonic electrons from enhancement of charm baryons in heavy ion collisions,” *Phys. Rev. C* **74** (2006) 024902, [arXiv:nucl-th/0512042](#).
- [55] G. Martinez-Garcia, S. Gadrat, and P. Crochet, “Consequences of a  $\Lambda_c/D$  enhancement effect on the non-photonic electron nuclear modification factor in central heavy ion collisions at RHIC energy,” *Phys. Lett. B* **663** (2008) 55–60, [arXiv:0710.2152 \[hep-ph\]](#). [Erratum: *Phys.Lett.B* 666, 533 (2008)].
- [56] Y. Oh, C. M. Ko, S. H. Lee, and S. Yasui, “Heavy baryon/meson ratios in relativistic heavy ion collisions,” *Phys. Rev. C* **79** (2009) 044905, [arXiv:0901.1382 \[nucl-th\]](#).
- [57] A. Andronic *et al.*, “Heavy-flavour and quarkonium production in the LHC era: from proton-proton to heavy-ion collisions,” *Eur. Phys. J. C* **76** (2016) 107, [arXiv:1506.03981 \[nucl-ex\]](#).
- [58] J. Altmann, A. Dubla, V. Greco, A. Rossi, and P. Skands, “Towards the understanding of heavy quarks hadronization: from leptonic to heavy-ion collisions,” *Eur. Phys. J. C* **85** (2025) 16, [arXiv:2405.19137 \[hep-ph\]](#).
- [59] W. M. Alberico, A. Beraudo, A. De Pace, A. Molinari, M. Monteno, M. Nardi, and F. Prino, “Heavy-flavour spectra in high energy nucleus-nucleus collisions,” *Eur. Phys. J. C* **71** (2011) 1666, [arXiv:1101.6008 \[hep-ph\]](#).
- [60] J. Song, H.-h. Li, and F.-l. Shao, “New feature of low  $p_T$  charm quark hadronization in  $pp$  collisions at  $\sqrt{s} = 7$  TeV,” *Eur. Phys. J. C* **78** (2018) 344, [arXiv:1801.09402 \[hep-ph\]](#).

- [61] V. Minissale, S. Plumari, and V. Greco, “Charm hadrons in pp collisions at LHC energy within a coalescence plus fragmentation approach,” *Phys. Lett. B* **821** (2021) 136622, [arXiv:2012.12001 \[hep-ph\]](#).
- [62] ALICE Collaboration, S. Acharya *et al.*, “Charm fragmentation fractions and  $c\bar{c}$  cross section in pPb collisions at  $\sqrt{s_{NN}} = 5.02$  TeV,” *Eur. Phys. J. C* **84** (2024) 1286, [arXiv:2405.14571 \[nucl-ex\]](#).
- [63] ALICE Collaboration, S. Acharya *et al.*, “Pseudorapidity densities of charged particles with transverse momentum thresholds in pp collisions at  $s=5.02$  and 13 TeV,” *Phys. Rev. D* **108** (2023) 072008, [arXiv:2211.15364 \[nucl-ex\]](#).
- [64] D. d’Enterria, K. J. Eskola, I. Helenius, and H. Paukkunen, “Confronting current NLO parton fragmentation functions with inclusive charged-particle spectra at hadron colliders,” *Nucl. Phys. B* **883** (2014) 615–628, [arXiv:1311.1415 \[hep-ph\]](#).
- [65] M. L. Mangano *et al.*, “Physics at a 100 TeV pp Collider: Standard Model Processes,” [arXiv:1607.01831 \[hep-ph\]](#).
- [66] FCC Collaboration, A. Abada *et al.*, “FCC-hh: The Hadron Collider: Future Circular Collider Conceptual Design Report Volume 3,” *Eur. Phys. J. ST* **228** (2019) 755–1107.
- [67] D. d’Enterria, T. Pierog, and G. Sun, “Impact of QCD jets and heavy-quark production in cosmic-ray proton atmospheric showers up to  $10^{20}$  eV,” *Astrophys. J.* **874** (2019) 152, [arXiv:1809.06406 \[astro-ph.HE\]](#).
- [68] F. Hekhorn, “felixhehorn/maunakea: Initial release for zenodo,” Nov., 2024. <https://doi.org/10.5281/zenodo.14185847>.
- [69] S. Carrazza, E. R. Nocera, C. Schwan, and M. Zaro, “PineAPPL: combining EW and QCD corrections for fast evaluation of LHC processes,” *JHEP* **12** (2020) 108, [arXiv:2008.12789 \[hep-ph\]](#).
- [70] C. Schwan, T. R. Rabemananjara, A. Candido, F. Hekhorn, T. Sharma, S. Carrazza, A. Barontini, J. Wissmann, and J. M. Cruz-Martinez, “Nnpdf/pineappl: v1.0.0,” June, 2025. <https://doi.org/10.5281/zenodo.15635174>.
- [71] N. Brambilla *et al.*, “Heavy Quarkonium: Progress, Puzzles, and Opportunities,” *Eur. Phys. J. C* **71** (2011) 1534, [arXiv:1010.5827 \[hep-ph\]](#).
- [72] J.-P. Lansberg, “New Observables in Inclusive Production of Quarkonia,” *Phys. Rept.* **889** (2020) 1–106, [arXiv:1903.09185 \[hep-ph\]](#).
- [73] E. Chapon *et al.*, “Prospects for quarkonium studies at the high-luminosity LHC,” *Prog. Part. Nucl. Phys.* **122** (2022) 103906, [arXiv:2012.14161 \[hep-ph\]](#).
- [74] ALEPH, DELPHI, L3, OPAL, SLD, LEP Electroweak Working Group, SLD Electroweak Group, SLD Heavy Flavour Group Collaboration, S. Schael *et al.*, “Precision electroweak measurements on the Z resonance,” *Phys. Rept.* **427** (2006) 257–454, [arXiv:hep-ex/0509008](#).
- [75] L. Gladilin, “Fragmentation fractions of  $c$  and  $b$  quarks into charmed hadrons at LEP,” *Eur. Phys. J. C* **75** (2015) 19, [arXiv:1404.3888 \[hep-ex\]](#).
- [76] M. Lisovyi, A. Verbytskyi, and O. Zenaiev, “Combined analysis of charm-quark fragmentation-fraction measurements,” *Eur. Phys. J. C* **76** (2016) 397, [arXiv:1509.01061 \[hep-ex\]](#).
- [77] ALICE Collaboration, S. Acharya *et al.*, “Charm production and fragmentation fractions at midrapidity in pp collisions at  $\sqrt{s} = 13$  TeV,” *JHEP* **12** (2023) 086, [arXiv:2308.04877 \[hep-ex\]](#).
- [78] L. Gladilin, “Charm hadron production fractions,” [arXiv:hep-ex/9912064](#).
- [79] ZEUS Collaboration, S. Chekanov *et al.*, “Measurement of charm fragmentation ratios and fractions in photoproduction at HERA,” *Eur. Phys. J. C* **44** (2005) 351–366, [arXiv:hep-ex/0508019](#).
- [80] Particle Data Group Collaboration, C. Amsler *et al.*, “Review of Particle Physics,” *Phys. Lett. B* **667** (2008) 1–1340.
- [81] ZEUS Collaboration, H. Abramowicz *et al.*, “Measurement of charm fragmentation fractions in photoproduction at HERA,” *JHEP* **09** (2013) 058, [arXiv:1306.4862 \[hep-ex\]](#).
- [82] HFLAV Collaboration, Y. S. Amhis *et al.*, “Averages of  $b$ -hadron,  $c$ -hadron, and  $\tau$ -lepton properties as of 2018,” *Eur. Phys. J. C* **81** (2021) 226, [arXiv:1909.12524 \[hep-ex\]](#).
- [83] ALEPH Collaboration, D. Buskulic *et al.*, “Measurements of mean lifetime and branching fractions of  $b$  hadrons decaying to  $J/\psi$ ,” *Phys. Lett. B* **295** (1992) 396–408.
- [84] L3 Collaboration, O. Adriani *et al.*, “ $\chi(c)$  production in hadronic Z decays,” *Phys. Lett. B* **317** (1993) 467–473.
- [85] DELPHI Collaboration, P. Abreu *et al.*, “ $J/\psi$  production in the hadronic decays of the Z,” *Phys. Lett. B* **341** (1994) 109–122.
- [86] DELPHI Collaboration, P. Abreu *et al.*, “A Study of  $B^0 - \bar{B}^0$  mixing using semileptonic decays of  $B$  hadrons produced from  $Z^0$ ,” *Phys. Lett. B* **301** (1993) 145–154.
- [87] L3 Collaboration, M. Acciarri *et al.*, “Measurement of the branching ratios  $b \rightarrow e$  neutrino X,  $\mu$  neutrino X,  $\tau$ -neutrino X and neutrino X,” *Z. Phys. C* **71** (1996) 379–390.
- [88] OPAL Collaboration, G. Abbiendi *et al.*, “Measurements of inclusive semileptonic branching fractions of  $b$  hadrons in Z0 decays,” *Eur. Phys. J. C* **13** (2000) 225–240, [arXiv:hep-ex/9906041](#).
- [89] ALEPH Collaboration, A. Heister *et al.*, “Inclusive semileptonic branching ratios of  $b$  hadrons produced in Z decays,” *Eur. Phys. J. C* **22** (2002) 613–626, [arXiv:hep-ex/0108007](#).
- [90] ALEPH, DELPHI, L3, OPAL Collaboration, “Combining heavy flavor electroweak measurements at LEP,” *Nucl. Instrum. Meth. A* **378** (1996) 101–115.
- [91] ALICE Collaboration, S. Acharya *et al.*, “Dielectron and heavy-quark production in inelastic and high-multiplicity proton–proton collisions at  $\sqrt{s_{NN}} = 13$  TeV,” *Phys. Lett. B* **788** (2019) 505–518, [arXiv:1805.04407 \[hep-ex\]](#).
- [92] LHCB Collaboration, R. Aaij *et al.*, “Measurements of prompt charm production cross-sections in pp collisions at  $\sqrt{s} = 13$  TeV,” *JHEP* **03** (2016) 159, [arXiv:1510.01707 \[hep-ex\]](#). [Erratum: JHEP 09, 013 (2016), Erratum: JHEP 05, 074 (2017)].

- [93] CMS Collaboration, A. Tumasyan *et al.*, “Measurement of prompt open-charm production cross sections in proton-proton collisions at  $\sqrt{s} = 13$  TeV,” *JHEP* **11** (2021) 225, [arXiv:2107.01476 \[hep-ex\]](#).
- [94] LHCb Collaboration, R. Aaij *et al.*, “Observation of strangeness enhancement with charmed mesons in high-multiplicity pPb collisions at  $\sqrt{s_{NN}}=8.16$  TeV,” *Phys. Rev. D* **110** (2024) L031105, [arXiv:2311.08490 \[hep-ex\]](#).
- [95] ALICE Collaboration, B. Abelev *et al.*, “Measurement of electrons from beauty hadron decays in pp collisions at  $\sqrt{s} = 7$  TeV,” *Phys. Lett. B* **721** (2013) 13–23, [arXiv:1208.1902 \[hep-ex\]](#). [Erratum: *Phys.Lett.B* 763, 507–509 (2016)].
- [96] ALICE Collaboration, S. Acharya *et al.*, “Dielectron production in proton-proton collisions at  $\sqrt{s} = 7$  TeV,” *JHEP* **09** (2018) 064, [arXiv:1805.04391 \[hep-ex\]](#).
- [97] ALICE Collaboration, B. Abelev *et al.*, “Measurement of charm production at central rapidity in proton-proton collisions at  $\sqrt{s} = 7$  TeV,” *JHEP* **01** (2012) 128, [arXiv:1111.1553 \[hep-ex\]](#).
- [98] ALICE Collaboration, B. Abelev *et al.*, “Measurement of charm production at central rapidity in proton-proton collisions at  $\sqrt{s} = 2.76$  TeV,” *JHEP* **07** (2012) 191, [arXiv:1205.4007 \[hep-ex\]](#).
- [99] ALICE Collaboration, S. Acharya *et al.*, “ $\Lambda_c^+$  production in pp collisions at  $\sqrt{s} = 7$  TeV and in p-Pb collisions at  $\sqrt{s_{NN}} = 5.02$  TeV,” *JHEP* **04** (2018) 108, [arXiv:1712.09581 \[nucl-ex\]](#).
- [100] ALICE Collaboration, J. Adam *et al.*, “D-meson production in p-Pb collisions at  $\sqrt{s_{NN}} = 5.02$  TeV and in pp collisions at  $\sqrt{s} = 7$  TeV,” *Phys. Rev. C* **94** (2016) 054908, [arXiv:1605.07569 \[nucl-ex\]](#).
- [101] ALICE Collaboration, S. Acharya *et al.*, “Measurement of D-meson production at mid-rapidity in pp collisions at  $\sqrt{s} = 7$  TeV,” *Eur. Phys. J. C* **77** (2017) 550, [arXiv:1702.00766 \[hep-ex\]](#).
- [102] ATLAS Collaboration, G. Aad *et al.*, “Measurement of  $D^{*+}$ ,  $D^+$  and  $D_s^+$  meson production cross sections in pp collisions at  $\sqrt{s} = 7$  TeV with the ATLAS detector,” *Nucl. Phys. B* **907** (2016) 717–763, [arXiv:1512.02913 \[hep-ex\]](#).
- [103] CMS Collaboration, “Measurement of double differential and total charm cross sections at 7 TeV.” CMS-PAS-BPH-22-007, 2024.
- [104] CMS Collaboration, S. Chatrchyan *et al.*, “ $J/\psi$  and  $\psi_{2S}$  production in pp collisions at  $\sqrt{s} = 7$  TeV,” *JHEP* **02** (2012) 011, [arXiv:1111.1557 \[hep-ex\]](#).
- [105] CMS Collaboration, V. Khachatryan *et al.*, “Prompt and Non-Prompt  $J/\psi$  Production in pp Collisions at  $\sqrt{s} = 7$  TeV,” *Eur. Phys. J. C* **71** (2011) 1575, [arXiv:1011.4193 \[hep-ex\]](#).
- [106] ALICE Collaboration, S. Acharya *et al.*, “Measurement of beauty and charm production in pp collisions at  $\sqrt{s} = 5.02$  TeV via non-prompt and prompt D mesons,” *JHEP* **05** (2021) 220, [arXiv:2102.13601 \[nucl-ex\]](#).
- [107] ALICE Collaboration, S. Acharya *et al.*, “Measurement of  $D^0$ ,  $D^+$ ,  $D^{*+}$  and  $D_s^+$  production in pp collisions at  $\sqrt{s} = 5.02$  TeV with ALICE,” *Eur. Phys. J. C* **79** (2019) 388, [arXiv:1901.07979 \[nucl-ex\]](#).
- [108] ALICE Collaboration, S. Acharya *et al.*, “ $\Lambda_c^+$  production in pp and in p-Pb collisions at  $\sqrt{s_{NN}} = 5.02$  TeV,” *Phys. Rev. C* **104** (2021) 054905, [arXiv:2011.06079 \[nucl-ex\]](#).
- [109] LHCb Collaboration, R. Aaij *et al.*, “Measurements of prompt charm production cross-sections in pp collisions at  $\sqrt{s} = 5$  TeV,” *JHEP* **06** (2017) 147, [arXiv:1610.02230 \[hep-ex\]](#).
- [110] LHCb Collaboration, R. Aaij *et al.*, “Study of prompt  $D^0$  meson production in pPb collisions at  $\sqrt{s_{NN}} = 5$  TeV,” *JHEP* **10** (2017) 090, [arXiv:1707.02750 \[hep-ex\]](#).
- [111] CMS Collaboration, A. M. Sirunyan *et al.*, “Measurement of prompt and nonprompt charmonium suppression in PbPb collisions at 5.02 TeV,” *Eur. Phys. J. C* **78** (2018) 509, [arXiv:1712.08959 \[nucl-ex\]](#).
- [112] CMS Collaboration, A. M. Sirunyan *et al.*, “Nuclear modification factor of  $D^0$  mesons in PbPb collisions at  $\sqrt{s_{NN}} = 5.02$  TeV,” *Phys. Lett. B* **782** (2018) 474–496, [arXiv:1708.04962 \[nucl-ex\]](#).
- [113] C. Bierlich, J. Wilkinson, J. Sun, G. Manca, R. Granier de Cassagnac, and J. Otwinowski, “Open charm production cross section from combined LHC experiments in pp collisions at  $\sqrt{s} = 5.02$  TeV,” *Eur. Phys. J. Plus* **139** (2024) 593, [arXiv:2311.11426 \[hep-ph\]](#).
- [114] CDF Collaboration, T. A. Aaltonen *et al.*, “Measurement of the  $D^+$ -meson production cross section at low transverse momentum in p- $\bar{p}$  collisions at  $\sqrt{s} = 1.96$  TeV,” *Phys. Rev. D* **95** (2017) 092006, [arXiv:1610.08989 \[hep-ex\]](#).
- [115] PHENIX Collaboration, A. Adare *et al.*, “Heavy-flavor electron-muon correlations in  $p + p$  and  $d+Au$  collisions at  $\sqrt{s_{NN}} = 200$  GeV,” *Phys. Rev. C* **89** (2014) 034915, [arXiv:1311.1427 \[nucl-ex\]](#).
- [116] PHENIX Collaboration, A. Adare *et al.*, “Dilepton mass spectra in p+p collisions at  $\sqrt{s_{NN}} = 200$ -GeV and the contribution from open charm,” *Phys. Lett. B* **670** (2009) 313–320, [arXiv:0802.0050 \[hep-ex\]](#).
- [117] PHENIX Collaboration, A. Adare *et al.*, “Measurements of  $e^+e^-$  pairs from open heavy flavor in p+p and  $d+A$  collisions at  $\sqrt{s_{NN}} = 200$  GeV,” *Phys. Rev. C* **96** (2017) 024907, [arXiv:1702.01084 \[nucl-ex\]](#).
- [118] PHENIX Collaboration, S. S. Adler *et al.*, “Single electrons from heavy flavor decays in p+p collisions at  $\sqrt{s_{NN}} = 200$  GeV,” *Phys. Rev. Lett.* **96** (2006) 032001, [arXiv:hep-ex/0508034](#).
- [119] PHENIX Collaboration, A. Adare *et al.*, “Measurement of high- $p_T$  single electrons from heavy-flavor decays in  $p + p$  collisions at  $\sqrt{s} = 200$  GeV,” *Phys. Rev. Lett.* **97** (2006) 252002, [arXiv:hep-ex/0609010](#).
- [120] PHENIX Collaboration, A. Adare *et al.*, “Heavy Quark Production in  $p + p$  and Energy Loss and Flow of Heavy Quarks in Au+Au Collisions at  $\sqrt{s_{NN}} = 200$  GeV,” *Phys. Rev. C* **84** (2011) 044905, [arXiv:1005.1627 \[nucl-ex\]](#).
- [121] STAR Collaboration, L. Adamczyk *et al.*, “Measurements of  $D^0$  and  $D^+$  Production in  $p + p$  Collisions at  $\sqrt{s} = 200$  GeV,” *Phys. Rev. D* **86** (2012) 072013, [arXiv:1204.4244 \[nucl-ex\]](#).
- [122] LHCb Collaboration, R. Aaij *et al.*, “First Measurement of Charm Production in its Fixed-Target Configuration at the LHC,” *Phys. Rev. Lett.* **122** (2019) 132002, [arXiv:1810.07907 \[hep-ex\]](#).

- [123] **LHCb** Collaboration, R. Aaij *et al.*, “Open charm production and asymmetry in pNe collisions at  $\sqrt{s_{NN}} = 68.5$  GeV,” *Eur. Phys. J. C* **83** (2023) 541, [arXiv:2211.11633 \[hep-ex\]](#).
- [124] **HERA-B** Collaboration, I. Abt *et al.*, “Measurement of  $D^0$ ,  $D^+$ ,  $D_s^+$  and  $D^{*+}$  Production in Fixed Target 920-GeV Proton-Nucleus Collisions,” *Eur. Phys. J. C* **52** (2007) 531–542, [arXiv:0708.1443 \[hep-ex\]](#).
- [125] **Fermilab E653** Collaboration, K. Kodama *et al.*, “Charm Meson Production in 800-GeV/c Proton - Emulsion Interactions,” *Phys. Lett. B* **263** (1991) 573–578.
- [126] C. Lourenco and H. K. Wohri, “Heavy flavour hadro-production from fixed-target to collider energies,” *Phys. Rept.* **433** (2006) 127–180, [arXiv:hep-ph/0609101](#).
- [127] **E789** Collaboration, M. J. Leitch *et al.*, “Nuclear dependence of neutral D meson production by 800-GeV/c protons,” *Phys. Rev. Lett.* **72** (1994) 2542–2545.
- [128] R. Ammar *et al.*, “D-Meson Production in 800-GeV/c p Pinteractions,” *Phys. Rev. Lett.* **61** (1988) 2185–2188.
- [129] **NA38**, **NA50** Collaboration, M. C. Abreu *et al.*, “Dimuon and charm production in nucleus-nucleus collisions at the CERN SPS,” *Eur. Phys. J. C* **14** (2000) 443–455.
- [130] **LEBC-EHS** Collaboration, M. Aguilar-Benitez *et al.*, “Charm Hadron Properties in 400-GeV/c p p Interactions,” *Z. Phys. C* **40** (1988) 321.
- [131] **LEBC-EHS** Collaboration, M. Aguilar-Benitez *et al.*, “D meson branching ratios and hadronic charm production cross-sections,” *Phys. Lett. B* **135** (1984) 237–242.
- [132] **E769** Collaboration, G. A. Alves *et al.*, “Forward cross-sections for production of  $D^+$ ,  $D^0$ ,  $D_s$ ,  $D^{*+}$  and  $\Lambda_c$  in 250-GeV  $\pi^\pm$ ,  $K^\pm$ , and p-nucleon interactions,” *Phys. Rev. Lett.* **77** (1996) 2388–2391. [Erratum: *Phys.Rev.Lett.* 81, 1537 (1998)].
- [133] **ACCMOR** Collaboration, S. Barlag *et al.*, “Production of D,  $D^*$  and  $D_s$  Mesons in 200-GeV/c  $\pi^-$ ,  $K^-$  and p-Si Interactions,” *Z. Phys. C* **39** (1988) 451.
- [134] **ACCMOR** Collaboration, S. Barlag *et al.*, “Production properties of  $D^0$ ,  $D^+$ ,  $D^{*+}$  and  $D_s^+$  in 230-GeV/c  $\pi^-$  and  $K^-$ -Cu interactions,” *Z. Phys. C* **49** (1991) 555–562.
- [135] **SVD** Collaboration, N. S. Amaglobeli *et al.*, “Experimental estimation of the charm production cross-section in p p interactions at 70-GeV/c with the aid of the SVD setup,” *Phys. Atom. Nucl.* **64** (2001) 891–901.
- [136] **SVD-2** Collaboration, A. Alev *et al.*, “Charmed particles production in pA -interactions at  $\sqrt{s} = 11.8$  GeV,” *Eur. Phys. J. A* **53** (2017) 45.
- [137] P. M. Nadolsky, H.-L. Lai, Q.-H. Cao, J. Huston, J. Pumplin, D. Stump, W.-K. Tung, and C. P. Yuan, “Implications of CTEQ global analysis for collider observables,” *Phys. Rev. D* **78** (2008) 013004, [arXiv:0802.0007 \[hep-ph\]](#).
- [138] **NNPDF** Collaboration, R. D. Ball *et al.*, “Parton distributions for the LHC Run II,” *JHEP* **04** (2015) 040, [arXiv:1410.8849 \[hep-ph\]](#).
- [139] Y. Yang, A. Geiser, S.-O. Moch, and O. Zenaiev, “A novel phenomenological approach to total charm cross-section measurements at the LHC,” *Eur. Phys. J. C* **86** (2026) 225, [arXiv:2506.22616 \[hep-ph\]](#).
- [140] X. Bai, G. Li, Y. Zhang, Q. Situ, and X. Chen, “Data-driven analysis of the beauty hadron production in pp collisions at the LHC with Bayesian unfolding,” *JHEP* **11** (2024) 018, [arXiv:2405.01444 \[nucl-ex\]](#).
- [141] **ALICE** Collaboration, D. Ali Hassan Abdallah *et al.*, “Measurement of the  $B^0$ -meson production cross section in proton–proton collisions at  $\sqrt{s} = 13.6$  TeV,” [arXiv:2603.18904 \[hep-ex\]](#).
- [142] **ALICE** Collaboration, S. Acharya *et al.*, “Measurement of beauty-quark production in pp collisions at  $\sqrt{s} = 13$  TeV via non-prompt D mesons,” *JHEP* **10** (2024) 110, [arXiv:2402.16417 \[hep-ex\]](#).
- [143] **LHCb** Collaboration, R. Aaij *et al.*, “Measurement of the b-quark production cross-section in 7 and 13 TeV pp collisions,” *Phys. Rev. Lett.* **118** (2017) 052002, [arXiv:1612.05140 \[hep-ex\]](#). [Erratum: *Phys.Rev.Lett.* 119, 169901 (2017)].
- [144] **LHCb** Collaboration, R. Aaij *et al.*, “Measurement of the  $B^+$  production cross-section in pp collisions at  $\sqrt{s} = 7$  and 13 TeV,” *JHEP* **12** (2017) 026, [arXiv:1710.04921 \[hep-ex\]](#).
- [145] **LHCb** Collaboration, R. Aaij *et al.*, “Measurement of forward  $J/\psi$  production cross-sections in pp collisions at  $\sqrt{s} = 13$  TeV,” *JHEP* **10** (2015) 172, [arXiv:1509.00771 \[hep-ex\]](#). [Erratum: *JHEP* 05, 063 (2017)].
- [146] **CMS** Collaboration, V. Khachatryan *et al.*, “Measurement of the total and differential inclusive  $B^+$  hadron cross sections in pp collisions at  $\sqrt{s} = 13$  TeV,” *Phys. Lett. B* **771** (2017) 435–456, [arXiv:1609.00873 \[hep-ex\]](#).
- [147] **LHCb** Collaboration, R. Aaij *et al.*, “Measurement of  $B^+$ ,  $B^0$  and  $\Lambda_b^0$  production in pPb collisions at  $\sqrt{s_{NN}} = 8.16$  TeV,” *Phys. Rev. D* **99** (2019) 052011, [arXiv:1902.05599 \[hep-ex\]](#).
- [148] **ALICE** Collaboration, B. Abelev *et al.*, “Measurement of prompt  $J/\psi$  and beauty hadron production cross sections at mid-rapidity in pp collisions at  $\sqrt{s} = 7$  TeV,” *JHEP* **11** (2012) 065, [arXiv:1205.5880 \[hep-ex\]](#).
- [149] **LHCb** Collaboration, R. Aaij *et al.*, “Measurement of B meson production cross-sections in proton-proton collisions at  $\sqrt{s} = 7$  TeV,” *JHEP* **08** (2013) 117, [arXiv:1306.3663 \[hep-ex\]](#).
- [150] **LHCb** Collaboration, R. Aaij *et al.*, “Measurement of the  $B^\pm$  production cross-section in pp collisions at  $\sqrt{s} = 7$  TeV,” *JHEP* **04** (2012) 093, [arXiv:1202.4812 \[hep-ex\]](#).
- [151] **LHCb** Collaboration, R. Aaij *et al.*, “Measurement of  $\sigma(pp \rightarrow b\bar{b}X)$  at  $\sqrt{s} = 7$  TeV in the forward region,” *Phys. Lett. B* **694** (2010) 209–216, [arXiv:1009.2731 \[hep-ex\]](#).
- [152] **LHCb** Collaboration, R. Aaij *et al.*, “Measurement of  $J/\psi$  production in pp collisions at  $\sqrt{s} = 7$  TeV,” *Eur. Phys. J. C* **71** (2011) 1645, [arXiv:1103.0423 \[hep-ex\]](#).
- [153] **CMS** Collaboration, V. Khachatryan *et al.*, “Measurement of the  $B^+$  production cross section in pp collisions at  $\sqrt{s} = 7$  TeV,” *Phys. Rev. Lett.* **106** (2011) 112001, [arXiv:1101.0131 \[hep-ex\]](#).

- [154] CMS Collaboration, S. Chatrchyan *et al.*, “Measurement of the  $B^0$  production cross section in pp Collisions at  $\sqrt{s} = 7$  TeV,” *Phys. Rev. Lett.* **106** (2011) 252001, [arXiv:1104.2892 \[hep-ex\]](#).
- [155] CMS Collaboration, S. Chatrchyan *et al.*, “Measurement of the strange  $B$  meson production cross section with  $J/\psi\phi$  decays in pp collisions at  $\sqrt{s} = 7$  TeV,” *Phys. Rev. D* **84** (2011) 052008, [arXiv:1106.4048 \[hep-ex\]](#).
- [156] CMS Collaboration, S. Chatrchyan *et al.*, “Measurement of the  $\Lambda_b$  cross section and the  $\bar{\Lambda}_b$  to  $\Lambda_b$  ratio with  $J/\psi\Lambda$  decays in pp collisions at  $\sqrt{s} = 7$  TeV,” *Phys. Lett. B* **714** (2012) 136–157, [arXiv:1205.0594 \[hep-ex\]](#).
- [157] CMS Collaboration, S. Chatrchyan *et al.*, “Measurement of the inclusive cross section  $\sigma(pp \rightarrow b\bar{b}X \rightarrow \mu\mu X)$  at  $\sqrt{s} = 7$  TeV,” *JHEP* **06** (2012) 110, [arXiv:1203.3458 \[hep-ex\]](#).
- [158] CMS Collaboration, V. Khachatryan *et al.*, “Inclusive b-hadron production cross section with muons in pp collisions at  $\sqrt{s} = 7$  TeV,” *JHEP* **03** (2011) 090, [arXiv:1101.3512 \[hep-ex\]](#).
- [159] ATLAS Collaboration, G. Aad *et al.*, “Measurement of the differential cross-section of  $B^+$  meson production in pp collisions at  $\sqrt{s} = 7$  TeV at ATLAS,” *JHEP* **10** (2013) 042, [arXiv:1307.0126 \[hep-ex\]](#).
- [160] LHCb Collaboration, R. Aaij *et al.*, “Measurement of  $J/\psi$  production cross-sections in pp collisions at  $\sqrt{s} = 5$  TeV,” *JHEP* **11** (2021) 181, [arXiv:2109.00220 \[hep-ex\]](#).
- [161] CMS Collaboration, A. M. Sirunyan *et al.*, “Studies of Beauty Suppression via Nonprompt  $D^0$  Mesons in Pb-Pb Collisions at  $Q^2 = 4$  GeV $^2$ ,” *Phys. Rev. Lett.* **123** (2019) 022001, [arXiv:1810.11102 \[hep-ex\]](#).
- [162] CMS Collaboration, A. M. Sirunyan *et al.*, “Measurement of the  $B^\pm$  Meson Nuclear Modification Factor in Pb-Pb Collisions at  $\sqrt{s_{NN}} = 5.02$  TeV,” *Phys. Rev. Lett.* **119** (2017) 152301, [arXiv:1705.04727 \[hep-ex\]](#).
- [163] ALICE Collaboration, B. B. Abelev *et al.*, “Beauty production in pp collisions at  $\sqrt{s} = 2.76$  TeV measured via semi-electronic decays,” *Phys. Lett. B* **738** (2014) 97–108, [arXiv:1405.4144 \[nucl-ex\]](#).
- [164] CDF Collaboration, D. Acosta *et al.*, “Measurement of the  $J/\psi$  meson and  $b$ -hadron production cross sections in p- $\bar{p}$  collisions at  $\sqrt{s} = 1960$  GeV,” *Phys. Rev. D* **71** (2005) 032001, [arXiv:hep-ex/0412071](#).
- [165] UA1 Collaboration, C. Albajar *et al.*, “Beauty production at the CERN p- $\bar{p}$  collider,” *Phys. Lett. B* **256** (1991) 121–128. [Erratum: Phys.Lett.B 262, 497 (1991)].
- [166] UA1 Collaboration, C. Albajar *et al.*, “Measurement of  $b\bar{b}$  correlations at the CERN p- $\bar{p}$  collider,” *Z. Phys. C* **61** (1994) 41–52.
- [167] PHENIX Collaboration, C. Aidala *et al.*, “Measurements of  $B \rightarrow J/\psi$  at forward rapidity in p+p collisions at  $\sqrt{s} = 510$  GeV,” *Phys. Rev. D* **95** (2017) 092002, [arXiv:1701.01342 \[hep-ex\]](#).
- [168] PHENIX Collaboration, A. Adare *et al.*, “Ground and excited charmonium state production in  $p + p$  collisions at  $\sqrt{s} = 200$  GeV,” *Phys. Rev. D* **85** (2012) 092004, [arXiv:1105.1966 \[hep-ex\]](#).
- [169] PHENIX Collaboration, U. Acharya *et al.*, “Production of  $b\bar{b}$  at forward rapidity in p+p collisions at  $\sqrt{s} = 510$  GeV,” *Phys. Rev. D* **102** (2020) 092002, [arXiv:2005.14276 \[hep-ex\]](#).
- [170] PHENIX Collaboration, A. Adare *et al.*, “Measurement of Bottom versus Charm as a Function of Transverse Momentum with Electron-Hadron Correlations in  $p + p$  Collisions at  $\sqrt{s} = 200$  GeV,” *Phys. Rev. Lett.* **103** (2009) 082002, [arXiv:0903.4851 \[hep-ex\]](#).
- [171] PHENIX Collaboration, A. Adare *et al.*, “Cross section for  $b\bar{b}$  production via dielectrons in d+Au collisions at  $\sqrt{s_{NN}} = 200$  GeV,” *Phys. Rev. C* **91** (2015) 014907, [arXiv:1405.4004 \[nucl-ex\]](#).
- [172] PHENIX Collaboration, C. Aidala *et al.*, “ $B$ -meson production at forward and backward rapidity in  $p + p$  and Cu + Au collisions at  $\sqrt{s_{NN}} = 200$  GeV,” *Phys. Rev. C* **96** (2017) 064901, [arXiv:1702.01085 \[nucl-ex\]](#).
- [173] PHENIX Collaboration, C. Aidala *et al.*, “Measurements of  $\mu\mu$  pairs from open heavy flavor and Drell-Yan in  $p + p$  collisions at  $\sqrt{s} = 200$  GeV,” *Phys. Rev. D* **99** (2019) 072003, [arXiv:1805.02448 \[hep-ex\]](#).
- [174] STAR Collaboration, H. Agakishiev *et al.*, “High  $p_T$  non-photonic electron production in  $p + p$  collisions at  $\sqrt{s} = 200$  GeV,” *Phys. Rev. D* **83** (2011) 052006, [arXiv:1102.2611 \[nucl-ex\]](#).
- [175] HERA-B Collaboration, I. Abt *et al.*, “Measurement of the  $b\bar{b}$  production cross-section in 920-GeV fixed target proton nucleus collisions,” *Eur. Phys. J. C* **26** (2003) 345–355, [arXiv:hep-ex/0205106](#).
- [176] HERA-B Collaboration, I. Abt *et al.*, “Improved measurement of the  $b\bar{b}$  production cross section in 920-GeV fixed-target proton-nucleus collisions,” *Phys. Rev. D* **73** (2006) 052005, [arXiv:hep-ex/0512030](#).
- [177] HERA-B Collaboration, I. Abt *et al.*, “Bottom production cross-section from double muonic decays of b-flavoured hadrons in 920-GeV proton-nucleus collision,” *Phys. Lett. B* **650** (2007) 103–110, [arXiv:hep-ex/0612024](#).
- [178] E771 Collaboration, T. Alexopoulos *et al.*, “A Measurement of the  $b\bar{b}$  cross-section in 800-GeV/c proton silicon interactions,” *Phys. Rev. Lett.* **82** (1999) 41–44.
- [179] D. M. Jansen *et al.*, “Measurement of the bottom quark production cross-section in 800-GeV/c proton - gold collisions,” *Phys. Rev. Lett.* **74** (1995) 3118–3121.
- [180] NNPDF Collaboration, R. D. Ball, A. Candido, J. Cruz-Martinez, S. Forte, T. Giani, F. Hekhorn, K. Kudashkin, G. Magni, and J. Rojo, “Evidence for intrinsic charm quarks in the proton,” *Nature* **608** (2022) 483–487, [arXiv:2208.08372 \[hep-ph\]](#).
- [181] M. Czakon and A. Mitov, “NNLO corrections to top-pair production at hadron colliders: the all-fermionic scattering channels,” *JHEP* **12** (2012) 054, [arXiv:1207.0236 \[hep-ph\]](#).
- [182] F. Hekhorn, “MaunaKea.” <https://github.com/felixhekhorn/MaunaKea>.
- [183] I. I. Y. Bigi, M. A. Shifman, N. G. Uraltsev, and A. I. Vainshtein, “The Pole mass of the heavy quark. Perturbation theory and beyond,” *Phys. Rev. D* **50** (1994) 2234–2246, [arXiv:hep-ph/9402360](#).

- [184] M. Beneke and V. M. Braun, “Heavy quark effective theory beyond perturbation theory: Renormalons, the pole mass and the residual mass term,” *Nucl. Phys. B* **426** (1994) 301–343, [arXiv:hep-ph/9402364](#).
- [185] **Particle Data Group** Collaboration, R. L. Workman *et al.*, “Review of Particle Physics,” *PTEP* **2022** (2022) 083C01.
- [186] R. D. Ball, V. Bertone, M. Bonvini, S. Marzani, J. Rojo, and L. Rottoli, “Parton distributions with small- $x$  resummation: evidence for BFKL dynamics in HERA data,” *Eur. Phys. J. C* **78** (2018) 321, [arXiv:1710.05935 \[hep-ph\]](#).
- [187] **xFitter Developers’ Team** Collaboration, H. Abdolmaleki *et al.*, “Impact of low- $x$  resummation on QCD analysis of HERA data,” *Eur. Phys. J. C* **78** (2018) 621, [arXiv:1802.00064 \[hep-ph\]](#).
- [188] M. Bonvini and F. Giuliani, “A new simple PDF parametrization: improved description of the HERA data,” *Eur. Phys. J. Plus* **134** (2019) 531, [arXiv:1902.11125 \[hep-ph\]](#).
- [189] F. Silvetto and M. Bonvini, “Differential heavy quark pair production at small  $x$ ,” *Eur. Phys. J. C* **83** (2023) 267, [arXiv:2211.10142 \[hep-ph\]](#).
- [190] N. Armesto, T. Lappi, H. Mäntysaari, H. Paukkunen, and M. Tevio, “Signatures of gluon saturation from structure-function measurements,” *Phys. Rev. D* **105** (2022) 114017, [arXiv:2203.05846 \[hep-ph\]](#).
- [191] R. D. Ball, J. ter Hoeve, and R. Stegeman, “A Determination of the Top Mass from a Global PDF Analysis,” [arXiv:2603.28865 \[hep-ph\]](#).
- [192] A. Buckley, J. Ferrando, S. Lloyd, K. Nordström, B. Page, M. Rüfenacht, M. Schönherr, and G. Watt, “LHAPDF6: parton density access in the LHC precision era,” *Eur. Phys. J. C* **75** (2015) 132, [arXiv:1412.7420 \[hep-ph\]](#).
- [193] H. D. I. Abarbanel, M. L. Goldberger, and S. B. Treiman, “Asymptotic properties of electroproduction structure functions,” *Phys. Rev. Lett.* **22** (1969) 500–502.
- [194] R. G. Roberts, *The Structure of the proton: Deep inelastic scattering*. Cambridge Monographs on Mathematical Physics. Cambridge University Press, 2, 1994.
- [195] S. Carrazza, J. M. Cruz-Martinez, and R. Stegeman, “A data-based parametrization of parton distribution functions,” *Eur. Phys. J. C* **82** (2022) 163, [arXiv:2111.02954 \[hep-ph\]](#).
- [196] R. Stegeman, S. Carrazza, and J. Cruz-Martinez, “Small  $x$  extrapolation for parton distributions,” *PoS EPS-HEP2021* (2022) 371.
- [197] R. D. Ball and S. Forte, “Double asymptotic scaling at HERA,” *Phys. Lett. B* **335** (1994) 77–86, [arXiv:hep-ph/9405320](#).
- [198] **NNPDF** Collaboration, R. D. Ball *et al.*, “Parton distributions from high-precision collider data,” *Eur. Phys. J. C* **77** (2017) 663, [arXiv:1706.00428 \[hep-ph\]](#).
- [199] **NNPDF** Collaboration, R. D. Ball *et al.*, “Determination of the theory uncertainties from missing higher orders on NNLO parton distributions with percent accuracy,” *Eur. Phys. J. C* **84** (2024) 517, [arXiv:2401.10319 \[hep-ph\]](#).
- [200] S. Forte and Z. Kassabov, “Why  $\alpha_s$  cannot be determined from hadronic processes without simultaneously determining the parton distributions,” *Eur. Phys. J. C* **80** (2020) 182, [arXiv:2001.04986 \[hep-ph\]](#).
- [201] S. Forte, J. Rojo, and R. Stegeman, “Extractions of the strong coupling from collider data without PDF refitting are biased,” in *2025 European Physical Society Conference on High Energy Physics*. 11, 2025. [arXiv:2511.22561 \[hep-ph\]](#).
- [202] T. Kneesch, B. A. Kniehl, G. Kramer, and I. Schienbein, “Charmed-meson fragmentation functions with finite-mass corrections,” *Nucl. Phys. B* **799** (2008) 34–59, [arXiv:0712.0481 \[hep-ph\]](#).
- [203] K. J. Eskola, P. Paakkinen, H. Paukkunen, and C. A. Salgado, “EPPS21: a global QCD analysis of nuclear PDFs,” *Eur. Phys. J. C* **82** (2022) 413, [arXiv:2112.12462 \[hep-ph\]](#).